Mars:

High Resolution VLA Observations at Wavelengths of 2 and 6cm and Derived Properties

Thesis by

Donald J. Rudy

In Partial Fulfillment of the Requirements
for the Degree of
Doctor of Philosophy

California Institute of Technology
Pasadena, California

1987

(submitted March 2, 1987)

© MCMLXXXVII
Donald James Rudy
All Rights Reserved

This is lovingly dedicated to Al and Arlene,
to Mike and Linda, and to Florence

ACKNOWLEDGEMENTS

You don't learn to hold your own in the world by standing on guard, but by attacking and getting well hammered yourself.
G.B. Shaw

First and foremost, I would like to thank my advisor, Herr Doktor Professor Dewey Muhleman. He gave me the right kind and amount of supervision I needed. I felt neither ignored nor intensely scrutinized. Dewey also had an uncanny ability to come and ask me for some results exactly one-half day before I had them ready for him. How he knew **I'll** never know. I'd also like to thank him for letting me eat my lunch in peace, and having the diversity of interests to be able to talk about issues other than science. Dewey, I'd also like to thank you for showing me there's (almost) always time for ice cream even when there's no time for ice cream and for not being able to convince me to give up radio astronomy to sell shoes (although only history will tell if you should have tried harder).

A big thank you to Glenn Berge for all the assistance he provided in teaching this neophyte all about the big bad world of astronomical observing. If it weren't for Glenn I would probably have been pointing the telescopes at passing flocks of migratory birds. Thanks for all the help Glenn, and may your phase always remain stable.

I would like to acknowledge the faculty here for what they have done (and what they've restrained from doing) over the years. I have to admit the faculty here is first rate and really know their science. I don't think I would have found as knowledgeable a group of scientists anywhere else I could have gone as I did here. I would also like to thank all those people who have helped me with this dissertation. All of the helpful (and some of the not so helpful) discussions are greatly appreciated.

In addition, I would like to thank a friend of mine who, during my early years as a student here, was always there to talk to and would listen, without criticism (or

laughter), to all my deep and dark secrets. He was someone to trust and although I ribbed him incessantly, he was always my friend. To Jonathon I. Lunine I owe a heartfelt thanks. Jon I sorely miss ye.

I would like to thank Dave Jewitt for rolling down the hall occasionally. He and Mike Summers were always up to something (filling offices with computer paper, sawing the legs off of desks, changing doorknobs around, the list is almost endless). Their pranks were (almost) always amusing and their infamy for them was a great smoke screen for when I tried my hand at something. I would like to thank Dave for taking me on observing runs when I was all but useless as an astronomer and showing me that even great astronomers can fall asleep while observing. I would like to thank Mike (Michael now) for moral support in my later years as a graduate student and for showing me what its like to really bust loose.

To my all of my office-mates over the years, especially to Carol and Randy, I would like to say that I am grateful for all the help given me and thanks for being out of the office most of the time. I would like to thank Carol for all the things she's done for me. If we had not shared an office, I know my life would not be the same. To the Kirk, the creator, I would like to express my gratitude for allowing me to steal the fonts used in producing this thesis and I would like to remind him that the key is acceptance. To the happy hour crew, Bob, Ken, both Cindy's, Arie, Jimbo, and others, I wish to express my deep gratitude for allowing me to cajole you into joining me for a drink after work. I always enjoyed our conversations even though at times I got a little belligerent (I especially enjoyed them then). I know Thursdays will never be the same again. There has never been, nor is there likely to be, a person who can aggravate me so much and yet who is as close to me as a brother as Arie Grossman. May you never be caught with your finger in the pie, Arie. And to Cindy Piotrowski I owe a debt of gratitude (and a hearty Hi-yo Silver) for helping me in innumerable ways. I will never forget her and all she did for me. To Tim, who fits neatly in no

category, but rather loosely in many of them, I would like to say thanks for being a friend.

I would like to express a heart-felt 'Thank you' to Dr. Bob Sharp, who has, through field trips around California and Hawaii, shown a dyed-in-the-wool skeptic that there is more to geology than just memorization and classification. I would like to say to Kay Campbell, 'Mom', that I appreciate all the help you have given me in finding my way around the Kafka-esque world of Caltech bureaucracy. I would have never have figured out some of the ins and outs of the paperwork required of me without your help.

To the rest of my fellow conspirators Todd, Bruce, Lucien, Randy, Achmed Solar Wingo, Carolyn, Dave, Julie, Kathy, Diane, Mark, Mike, and all the rest of you who have help me become 'well-hammered', so long and thanks for all the fish.

Donald J. Rudy

ABSTRACT

Observations of Mars at wavelengths of 2 and 6cm were made using the VLA in its A configuration. Two seasons were observed; late spring in the northern hemisphere ($L_S \sim 60°$) and early summer in the southern summer ($L_S \sim 300°$). The sub-earth latitudes were 25°N and 25°S, for each of these seasons respectively. So the geometry for viewing the polar region was optimal in each case . Whole-disk brightness temperatures were estimated to be 193.2K±1.0 at 2cm and 191.2K±0.6 at 6cm for the northern data set and 202.2K±1.0 at 2cm and 195.4K±0.6 at 6cm for the southern data set (formal errors only). Since measurements of the polarized flux were taken at the same time, whole-disk effective dielectric constants could be estimated and from these, estimates of sub-surface densities could be made. The results of these calculations at 2cm yielded whole-disk effective dielectric constants of 2.34 ± 0.05 and 2.02 ± 0.03 which imply sub-surface densities of 1.24g cm$^{-3} \pm 0.06$ and 1.02g cm$^{-3} \pm 0.05$ for the north and south, respectively. The same calculations at 6cm yielded effective densities of 1.45g cm$^{-3} \pm 0.10$ and 1.31g cm$^{-3} \pm 0.07$ from effective dielectric constants of 2.70 ± 0.09 and 2.48 ± 0.06 for the north and south data sets, respectively.

From the mapped data these parameters were also estimated as a function of latitude between latitudes of 15°S and 60°N for the north data set; and between latitudes of 30°N and 60°S for the south data set. A region in which the brightness temperature behaves in an anomalous manner was discovered in both data sets. This region lies between about 10°S and 40°S. Here the brightness temperatures at both wavelengths in both data sets appears lower, by 4K to 8K, than a nominal model would predict. In addition to the effective dielectric constant and sub-surface density the radio absorption length of the sub-surface was estimated. The radio absorption length for most of these latitudes was about 15 wavelengths with formal errors on the

order of 5 or 10 wavelengths. This is true for both data sets. The estimation of the effective dielectric constant at most latitudes was between 2 and 3.5 with only slight differences between the two different wavelengths. The two data sets show the same relative trends, but are off by a scaling factor.

These estimates of the dielectric constant lead to estimation of the sub-surface densities as a function of latitude. Most calculations of the sub-surface density yielded results between 1 and 2 g cm^{-3} with errors on the order of 0.5 g cm^{-3}. These results seem to imply that the sub-surface is not much different than the surface as observed by the Viking and Mariner missions. In line with this, an examination of the correlation of the dielectric constant at each wavelength with the thermal inertia, determined by the Viking infrared measurements, shows a relatively strong correlation, at both wavelengths, for the North data set. The South data set, however, shows little to no correlation between the radio parameters and the thermal inertia. Since the South data set is primarily composed of latitudes which contain the anomalous region, it is not suprising that the South data set shows no correlation.

In addition, the thermal-radiative model used to estimate the above parameters was used to estimate the variability of the whole-disk brightness temperature of Mars. This was done in an effort to establish a background for those astronomers wishing to use Mars as a calibration source. The parameters investigated for their effect on the whole-disk brightness temperature of Mars were: the sub-earth longitude, the sub-earth latitude, the sub-earth time of day, the dielectric constant, and the radio absorption length. A nominal model was first created which established the variation of the brightness temperature as a function of season and radio absorption length. A nominal value of 2.2 was used for the dielectric constant, and the sub-earth latitude was set at 0°N and the sub-earth longitude was set at 75°W. The sub-earth time of day was held at noon for this nominal model. This is equivalent to a 0° phase angle. The most important geometric factor was the sub-earth latitude. The error in estimating

the whole-disk brightness temperature of Mars by using the wrong sub-earth latitude can be as large as 5 to 10%. The charts presented will be useful to estimate the whole-disk brightness temperature which the thermal model would predict. It is believed that the error in this estimate is less than or equal to 5K.

TABLE OF CONTENTS

TABLE OF FIGURES

TABLE OF TABLES

CHAPTER 1
INTRODUCTION

Observations of the radio thermal emission of the planet Mars have mostly been measurements of the variation of whole disk brightness temperatures as a function of season and longitude. Earlier work by others, Kuz'min and Losovskii (1984); Epstein *et al.* (1983); Jakosky and Muhleman (1980); Andrew *et al.* (1977); and Cuzzi and Muhleman (1972) to name a few, was done using either single dish antennae or smaller arrays (arrays with a small number of antennae, or short baselines), both of which have coarse spatial resolution. Mars has also been observed using radar. Both the Goldstone radar, Downs *et al.* (1975, 1973) and the Arecibo radar, Harmon and Ostro (1985) and Simpson and Tyler (1978), have observed Mars at different times and with different wavelengths. In addition, the Viking Orbiters telemetry antennae were used to perform a bi-static radar experiment. The resolution of these radar observations was greater than the previously mentioned ground-based observations of the radiometric emission. For some geometries, and certain of the radars, the resolution is even better than what we obtained at the VLA. However, the coverage is very limited in extent and the radar and radiometric results often disagree. There is no general consensus on why this should be the case.

Therefore, we attempt to extend the radiometric science by making estimates of sub-surface properties from observations that have a higher resolution than the whole disk radiometric measurements; and greater coverage than the bi-static radar measurements. We made two sets of observations of the thermal emission of Mars. The first set was taken on November 5 and 7, 1983; at two radio wavelengths, 2 and 6 cm. For this observing run, the viewing geometry was such that a clear view of the north polar region of Mars was obtained. The second set of observations was taken

on February 1 and 2, 1985; at the same wavelengths as the first data set. This second set of data was taken when the viewing geometry for the south polar region was near optimal.

Our observations were made at the Very Large Array (VLA) in New Mexico, which is operated by the National Radio Astronomy Observatory (NRAO). The VLA is a system of twenty-seven radio antennae laid out in the shape of a Y, which has a maximum extent of 35 kilometers. Since each antenna's output can be correlated with the output of every other antenna, it is in essence 351 interferometers, each baseline of which is unique in either its orientation or length. Because of the earth's rotation, the orientation and projected length of each baseline on the sky change during the observation, thereby creating what is known as a synthetic aperture. This synthetic aperture responds in a manner similar to a physical aperture which has a diameter that is the size of the largest spacing, and which has receiving medium only where the antennae of the array are located (c.f. Fomalont and Wright, 1974).

Because the observed microwaves are emitted from a deeper region than the observed infrared radiation, these data are complementary to the observations made by the Viking and Mariner missions, which observed only the surface manifestation of the changing surface and sub-surface temperature. The observed radiometric emission is generated in the Martian sub-surface at depths of up to one meter, the exact depth range observed depending upon the wavelength and radio absorption length. Whole-disk temperatures were calculated using the unmapped, calibrated visibility data and these agree with observations made by several workers, giving us confidence in our calibration (c.f. Jakosky and Muhleman, 1980; Doherty *et al.*, 1979; and Andrew *et al.*, 1977; and Epstein, 1971 for a listing of observations before 1971). There were some problems with the calibration of the second data set. However, these were corrected through a bootstrap procedure which used the polarization data taken at

the same time. This polarization data was used to calculate whole-disk dielectric constants. From these dielectric constants, near surface densities were estimated for each of the two wavelengths on all days for which observations were made.

One of the major reasons for selecting to observe Mars at the times we did, was to ensure maximum visibility of the polar regions. During the first observation run the viewing geometry was optimal for observing the North Pole. Similarly, during the second observation run, the viewing geometry was optimal for observing the South Pole. Polar Cold Regions were observed surrounding each geometric pole and measured. These Regions are not to be confused with the Polar Caps of CO_2 frost that are observed in the visible. Since the thermal emission we measure comes from the sub-surface, the ground may be nearly as cold as the CO_2 frost, but may have no actual covering of CO_2. The size of the North Polar Cold Region was found to be consistent with measurements of the extent of the North Polar Cap made visually during the same season in previous years by other observers (e.g. Iwasaki *et al.*, 1984, 1982, 1979, and James, 1982, 1979). Unfortunately, the second observing run was too far into the southern summer for South Polar Cap to be resolvable according to other observations (James and Lumme, 1982; Fishbacher *et al.*, 1969). A South Polar Cold Region was seen in the radio, but its brightness temperature at 2cm is inconsistent with this entire region being covered with CO_2 frost.

In addition to the whole-disk measurements and the polar region interpretation, we also used the radio maps of the data, made using standard NRAO software, to fit to a thermal-radiative model. This model had as free parameters, two dielectric constants (one for each wavelength), and one radio absorption length (in units of wavelength). Since the data are smeared in longitude due to the rotation of the planet, these free parameters were allowed to vary as a function of latitude only. The resultant fitted values of these parameters have been compared with longitudinally averaged

thermal inertia data from the Viking missions. It appears that, except for very northern regions, the dielectric constants derived from the North data set behave in roughly the same manner as the thermal inertia, while the dielectric constants derived from the South data set do not correlate nearly as well, and the radio absorption length is nearly uncorrelated with the thermal inertia for both sets of observations.

The final chapter of this work concerns itself with using the model developed in previous chapters to ascertain the whole-disk brightness temperature of Mars for the purposes of establishing Mars as a source for radio calibration. To this end, the effect of varying assorted geometric and radio parameters on the whole-disk brightness temperature was investigated. Several tables are given which allow the whole-disk brightness temperature of Mars to be calculated for any observing geometry visible from Earth. In addition, there are also two tables which list the effect of changing the electrical parameters, dielectric constant and radio absorption length, on the whole-disk brightness temperature.

CHAPTER 2
DATA ACQUISITION AND CALIBRATION

Observations of the thermal emission of Mars were made on November 5 and 7, 1983, and on February 1 and 2, 1985, at two radio wavelengths, 2 and 6 cm for all four days. The observations were made by Dr. Duane Muhleman, Dr. Glenn Berge, and myself, at the Very Large Array (VLA) in New Mexico, which is operated by the National Radio Astronomy Observatory (NRAO). Approximately five hours of data at each wavelength were taken during the November observing run and approximately eight hours of data at each wavelength were obtained during the February observing run. Because of the nature of synthesis mapping a great deal of data manipulation was performed to put the data in its final form. The purpose of this chapter is to describe the raw data sets, how and why they were taken, and the procedures that went into producing the resulting, finished data sets.

2.1 The Very Large Array

As stated earlier the VLA is a system of twenty seven radio antennae which has a maximum extent of 35km. The output of the VLA is a set of correlations between each possible pairing of the twenty seven antennae. This output is obtained after every integration period, which was thirty seconds for our observations. Each of these 351 correlations, usually called visibilities, consists of four complex numbers, one for each possible correlation of the two orthogonally polarized receivers. These complex correlations are usually referred to as RR, LL, RL, LR, were L stands for the Left circularly polarized receiver and R stands for the Right circularly polarized receiver. Associated with each visibility is a baseline, projected on the sky, which has

a unique orientation and baseline spacing. This spacing and orientation are usually given in terms of rectangular coordinates, the east-west coordinate being called the U-component and the north-south coordinate being called the V-component of the projected baseline. These visibilities can be thought of as samples of a visibility function which is unknown to the observer, but is well defined over the entire UV-plane.

A simplified explanation of the process of reduction of VLA data is as follows: Since the visibility data will eventually be Fourier transformed using a Fast Fourier Transform (FFT) to obtain an image, the visibilities must be gridded onto a rectangular grid. Since the data do not come in this form a great deal of care is taken to make sure the estimates of the visibility at the grid points are good estimates of the visibility function. It is possible to do a Direct Fourier Transform (DFT) in which case the gridding step is avoided, but the amount of computer time grows prohibitively large with large data bases. For this reason the DFT is not normally used with VLA data. The gridded data are assigned weights at each grid point which are determined by some function chosen by the observer and having to do with the distribution of sampled points in the UV-plane. These weights can be made to be unity so that each visibility is given the same weight as all the others. Another, more common weighting scheme is called uniform weighting. This consists of weighting each visibility that is assigned to a grid point by the inverse of the number of visibilities assigned to that grid point. In effect each grid point has a weight of unity regardless of how many visibilities went into determining the value of the visibility function at that grid point. This has the effect of making the sampling of the UV-plane seem more uniform.

An FFT of these gridded visibilities is then performed, and the data are then convolved with a spheroidal function to help reduce the bad effects of the gridding process. The result is referred to as an image. This image exists in the XY-plane,

X being equivalent to the right ascension and Y being equivalent to the declination of points on the map. This image is the true brightness function of Mars (with added noise) convolved with a beam shape function. This beam shape function is the response of the VLA to a point source and is related, by a Fourier transform, to the map of sampled baselines in the UV-plane multiplied by the weights assigned to these points. In a sense, the beam shape function can be thought of as a Green's function for the image. Because the UV-plane is undersampled, the beam shape function, also known as the synthesized or dirty beam, can often have rather large sidelobes. These sidelobes, often forming interesting Moire-type patterns when imaged, can cause very real looking features in the images. Therefore, the final step in producing images is an attempt to remove the effects that the undersampling of the UV-plane is causing. In a sense, this is an attempt to 'de-convolve' the beam shape function from the image to obtain the true brightness distribution. Currently there are several techniques for doing this de-convolution, among them a maximum entropy method and several methods which use *a priori* knowledge of the brightness distribution.

CLEAN is the technique that was used on the data and therefore a brief exposition on the algorithm is in order. CLEANing is one of several techniques by which the convolution of the true structure with the synthesized beam, commonly called the dirty map, is systematically replaced by a model of the true structure convolved with a simple gaussian of the approximate size of the synthesized beam (c.f. Högbom, 1974). CLEAN attempts to replace the dirty beam with a gaussian called the CLEAN beam, which is oftentimes made to be circularly symmetric. The map resulting from this 'de-convolving' process is often called the CLEANed map. This 'de-convolving' is done by asserting that the true brightness is a collection of discrete point sources, each of which has a given value. Because convolution is a linear process, the sum of the convolutions of each of these discrete points is the convolution of the sum

of the points, i.e. the image. Since the response of the VLA to a point source is the dirty beam, the dirty map can be thought of as a sum of dirty beams all at different locations and multiplied by different scaling factors. CLEAN systematically goes through the dirty map and finds the point with the highest flux density, and subtracts a scaled dirty beam centered on this location from the dirty map. This process is repeated until a user-defined flux density for the search routine is reached. These scaling factors, often called CLEAN components, are then multiplied by the CLEAN beam and added together, in a process that is the reverse of the first part, to form the CLEAN map. The resultant map is a model of what would be seen if the UV-plane were not undersampled, i.e., if the synthesized beam were gaussian in shape.

A second, less intuitive, more interferometric, way to think of the CLEAN algorithm was introduced by Schwarz (1979). In the UV-plane, a single CLEAN component can be represented by a single complex number, which can be thought of as having a cosine real part and a sine imaginary part. Schwarz asserted that, under certain conditions, the CLEAN algorithm is equivalent to least squares fitting of a sum of these sines and cosines to the visibility data in the UV-plane. So, within given restrictions, the CLEAN map is the Fourier transform of a least squares fit of sines and cosines to the visibility data. In this case, the CLEAN components characterize the sine-functions. This is a more interferometric way to think of the CLEAN algorithm because the response of a single interferometer to a point source is a sine function

These 'deconvolved' maps (more correctly called images) are considered the final data. These images are what most researchers interpret and present in the literature; although in the present case visual inspection of the maps is of limited usefulness due to the smearing effect mentioned earlier. A technique that is sometimes used to reduce

the effect of noise in the final product is an application of amplitude and/or phase closure known as self-calibration. This technique of self-calibration requires that there be some *a priori* knowledge of the structure of the source because the source itself is used to re-calibrate the antenna gains. Since a planet is mostly minor structure on top of a bright ellipse, there readily exists this knowledge. In the present case, only the visibility phase was re-calibrated, as a ten degree error in the phase distorts the results as severely as a ten percent error in the amplitude, and the sensitivity of the instrument did not warrant an attempt to do both. The first attempt at de-convolving the true structure from the data (the CLEAN map) can also be used as input to this re-calibration, as long as the CLEAN procedure has not been carried out to the level of suspected error in the calibration. Therefore, this technique is iterative and we processed until the changes to the antenna gains during the self-calibration phase were in the noise (about 2 or 3 iterations). The resulting self-calibrated visibilities were then mapped and CLEANed one final time. These final images were compared with a suite of models; and the radio absorption length and the two dielectric constants were estimated using a linearized least squares procedure.

2.2 The Data Sets

The data were taken during a period of about eight hours each day on November 5 and 7, 1983, and during a period of about eleven hours each day on February 1 and 2, 1985. The observations were broken into 'scans', which consist of about five minutes observing Mars at one wavelength, then five minutes observing Mars at the other wavelength. This was followed by two minutes observing the secondary calibrator (a relatively strong radio source near Mars during the observations) at this same wavelength and then two minutes observing the secondary calibrator at the first

TABLE 2.1

VLA Mapping Parameters				
Date	Nov. 1983		Feb. 1985	
Wavelength	2cm	6cm	2cm	6cm
Frequency	14.940Ghz	4.860Ghz	14.940Ghz	4.860Ghz
Clean Beam FWHM	0.15′′	0.45′′	0.17′′	0.51′′
Pixel Width	0.044′′	0.11′′	0.048′′	0.12′′
Sub-earth Resolution	229km	679km	238km	713km

wavelength. This gave a total integration time, over the two days in November, of about five hours at each wavelength spent observing Mars. For the February data set the total integration time at each wavelength was about eight hours over the two days. Since data were taken at two wavelengths on each of two days, four independent data sets were obtained for each observation run.

During each observation run the VLA was in its largest configuration, the A array, giving us a resolution of about 0.45′′ at 6cm and about 0.15′′ at 2cm for the 1983 data set and about 0.51′′at 6cm and about 0.17′′ at 2cm for the 1985 data set. Since the size of Mars on the sky was larger in 1985 both data sets give roughly the same resolution at each wavelength. At 6cm the resolution at the sub-earth point was about 700km and at 2cm it was about 230km. The relevant ephemerides are given in Table 2.2. The season on Mars during the 1983 observation run was late northern spring ($L_S = 60°$), and therefore the seasonal North Polar Cap was receding. The sub-earth latitude was 25°N, and so the geometry for viewing the north polar region was optimal. For this reason the data taken during the 1983 observation run will be referred to as the Northern data set. During the 1985 observation run, the season on Mars was early southern summer ($L_S = 304°$), and therefore, the seasonal South Polar Cap was nearly gone. The sub-earth latitude during this second run was 26°S, and therefore, complements the first observation run by being optimal for viewing

TABLE 2.2

Ephemerides of Mars				
Date	Nov. 5,1983	Nov. 7,1983	Feb. 1,1985	Feb. 2,1985
L_S	59.6°	61.0°	304.4°	305.0°
Diameter	4.44′/	4.44′/	4.86′/	4.85′/
Heliocentric Distance	1.66294AU	1.66345AU	1.43112AU	1.43217AU
Central Meridian	322.6° → 68.8°	301.1° → 48.2°	44.2° → 190.9°	33.3° → 180.0°
Sub-earth Latitude	24.8°N	24.8°N	26.3°S	26.2°S
Sub-solar Latitude	21.3°N	21.5°N	20.7°S	20.6°S
$A_s - A_e$	−29.5°	−29.9°	31.9°	31.9°

A_s is the planetocentric right ascension of the sun , and A_e is the planetocentric right ascension of the earth

the south polar region. This second data set will be referred to as the Southern data set for this reason.

The difference between the solar and terrestrial planetocentric right ascensions was about -30° for the North data set and about 30° for the South data set. From this difference, known as the phase angle, the Martian time of day for a given point on the disk can be estimated. Because this angle, the difference between the two planetocentric right ascensions, is determined by the Sun-Mars-Earth geometry, it changes very little during one Martian day. This means that the North observations were taken while Mars was showing its afternoon hemisphere (sub-earth local time ~2 pm), and the South observation were taken while Mars was showing its morning hemisphere (sub-earth local time ~10 am).

Because the observation period was a large fraction of the length of a Martian day (8 or 11 hours vs. ~24.6 hours), the data are smeared in longitude. For this reason, plus the fact that the measurements were taken near the brightness sensitivity limit of the instrument, graphical representations of the maps are of limited use. Figure 2.1 is a collection of the CLEANed maps used in all the following discussions. Each

map is a combination of two days observations. The maps of the North data set show the North Polar Cold Region quite well, with the 2cm map showing a more symmetric pole because of its higher resolution. The maps of the South data set do not show as distinct a South Polar Cold Region. The 6cm map does indicate that there is a cold region at the south pole. The 2cm map shows a warm region on the eastern hemisphere that is almost certainly due to diurnal heating. Both the North and South 2cm maps have been convolved with a gaussian to both reduce the noise and make what features exist more easily discernible

Even though results are given as a function of latitude only, the difference between a given model and the data was performed at each point of the disk. This gave several tens of points at some latitude bins and over a hundred in other latitude bins. This varying number of points used to determine the electrical parameters shows up in the changing size of the formal error bars. Larger error bars near the limb are due mostly to the reduced number of points that went into these estimates. From looking at the data, the diurnal thermal wave is barely noticeable in the 2cm data and not at all discernible in the 6cm data. Therefore, averaging over longitude, which is in effect an average over time of day, has little effect on the results; especially as we perform the difference between model and data first, and the models contain the diurnal wave. In Chapter 6 the size of the effect of the diurnal wave upon the whole-disk brightness temperature will be seen to be small at these wavelengths.

2.3 Mapping and Self-Calibration

The Northern data were calibrated using the compact radio source 3C286 as a primary calibrator with an assumed flux density of 7.41 Jansky at 6.14cm and 3.45 Jansky at 2.00cm. We followed the standard VLA prescription to correct for the

MARS: 2CM SOUTH DATA SET

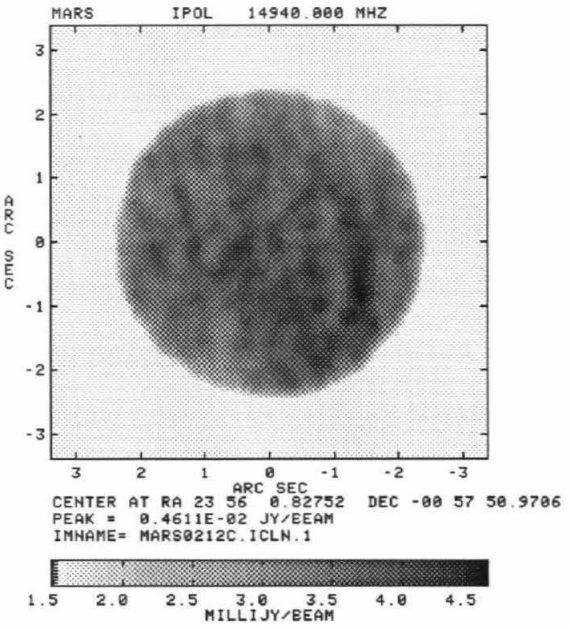

MARS: 6CM SOUTH DATA SET

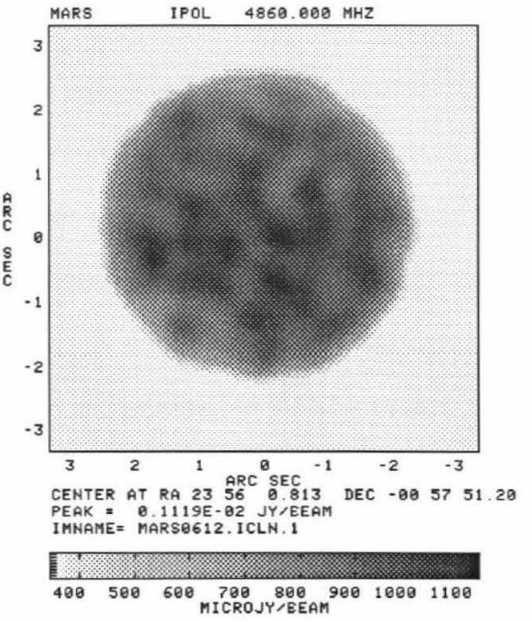

MARS: 2CM NORTH DATA SET

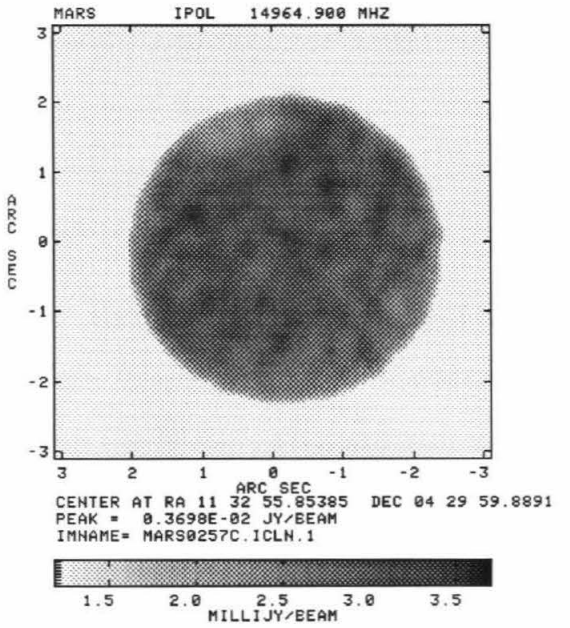

MARS: 6CM NORTH DATA SET

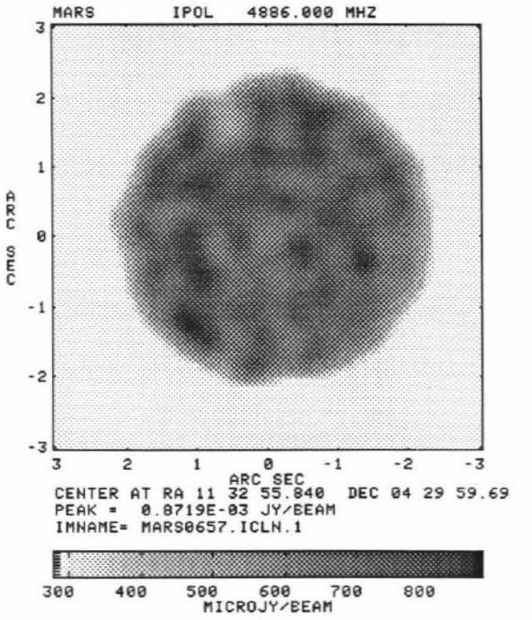

FIGURE 2.1: The four figures are maps of the brightness distribution for each observing run at each wavelength. Both days during each run were added together to obtain these maps.

fact that 3C286 is slightly resolved. The radio source P1148-001 was the secondary calibrator for the North data set. The secondary calibrator is a source which is close, on the plane of the sky, to the object being observed. For the Southern data, 3C286 was not above the horizon during the entire observing run. For this reason another primary calibrator was required. For the purpose of calibration the compact radio source 3C48 was also observed during the Southern observing run. The secondary calibrator for the Southern run was P2344+092. It could be this changing of the primary calibrators during the observing run that is responsible for the problems we experienced with the South data set calibration. These problems and their solution are discussed in Chapter 5. The standard NRAO fluxes were used even though there is some controversy about their accuracy, especially at the shorter wavelengths. It is thought by some (M. Klein, private communication) that the accepted flux density could be off by as much as five percent at 2cm. The effect of applying this correction would be to raise the brightness temperatures at 2cm by five to ten degrees. For the most part, these errors, due to the flux scale, are imbedded in all microwave observations of Mars. This caveat should be kept in mind while going through the results.

Calibration and mapping of the data were performed using standard NRAO software. Mapping consists of gridding the UV data with a user selected grid size. This grid size is commensurate with the requirement that in the XY-plane the dirty beam be 3 to 4 pixels (grid elements) in diameter. This requirement is so that the dirty beam is well-sampled, while at the same time keeping the total number of CLEAN components to a minimum. The size of the dirty beam is directly related to the largest baseline spacing, and, therefore, the resolution. However, since the imaging is done by Fourier transforming the visibility data, there is some freedom in choosing the map grid size. The pixel sizes chosen for the different observing runs and the

different wavelengths are given in Table 2.1 along with the size of the CLEAN beams used in the final mapping. The Full Width Half Maximum (FWHM) of the CLEAN beams are all close to the FWHM of the corresponding dirty beams. CLEANing was performed until the value of the CLEAN components was less than the RMS value of the noise. This insured that all real flux was accounted for.

Self-calibration was performed on all data sets. The basis of the self-calibration procedure is the assignment of the antenna gains as free parameters along with the brightness distribution (CLEAN components). So in addition to the set of CLEAN components, the complex antenna gains are also fit to the data. Since for each scan there are $\frac{N(N-1)}{2}$ visibilities recorded and only N antenna gains, there are $\frac{N(N-1)}{2} - N = \frac{N(N-3)}{2}$ 'good' visibilities per scan. This means a reduction in 'usable' data by a factor of $\frac{(N-3)}{(N-1)}$. For the VLA, where $N = 27$, this factor is about 0.92. Since the number of CLEAN components used is, at most, on the order of 10,000 to 15,000 and the number of visibilities recorded is usually on the order of 60,000 to 80,000, a reduction in the number of 'good' visibilities by a 8% is hardly going to affect the results. In addition, the antenna gains are complex numbers, so only solving for the phase, which is all that was done, reduces this loss to 4%. So the system of data and free parameters is still overdetermined by a factor of 2 or 3. Therefore, we have the utmost confidence that self-calibration can be applied to the data.

Another problem arises, however, in the practical application of self-calibration. In order for the VLA implementation of self-calibration to work properly the signal-to-noise ratio for a given baseline must be greater than one at a specific time. Since it is the antenna gain (and not the correlator gain) for which the equations are being solved, only one baseline with a signal to noise ratio greater than one is needed for each antenna. The algorithm used at the VLA allows the observer to restrict which baselines are used in the fitting process, but the restrictions cannot be too severe or

none of the baselines will be selected. Of course, it can hardly be called least squares fitting if only one baseline is used. So all baselines are used, with those greater than a specified length being given weights chosen by the observer. Obviously, if the procedure is working properly the changes from one iteration of self-calibration and CLEANing to the next will decrease. If they don't, then the noise is too great and the procedure can not be used.

For all data sets this cycle of CLEANing and self-calibration was followed until the changes in the antenna gains were less than five degrees on average. Another caveat that should be mentioned at this point, is that the self-calibration implementation used at the VLA flags (removes from the data base) any visibilities which are very far from the model visibilities used as a basis for the procedure. Noisy data will have many points far from the model. If the points are too far away, as determined by an internal check, the data are flagged. If an excessive amount of data are flagged as bad, the self-calibration procedure fails. This is another way to determine whether or not self-calibration should be used. None of the data sets had much more than five percent of their data flagged as being bad. As models for the self-calibration procedure, data from both days and both IFs were combined into one large data base and this was then mapped and CLEANed. This combination of data bases should have the effect of reducing the noise by a factor of two. In addition, the data were strongly tapered before being mapped to decrease the influence of the longest (and therefore, noisiest) baselines. Tapering is a weighting of the visibilities that decreases with distance from the phase center.

Even with all the procedures used to correct for bad weather and other uncontrollable events, the calibration for the Southern data set was still poor. We believe that the error in the calibration of the 6cm South data was about 6% and the error in the 2cm data to be on the order of 9%. So, to correct for this bad calibration, a

bootstrap method of calibrating was used. Since the whole-disk dielectric constant estimate was made from the polarized intensity, which doesn't depend on good absolute calibration, it could be used as the input parameter to a thermal model and a whole-disk brightness temperature could be calculated. The reason the whole-disk dielectric constant doesn't depend on the flux calibration is that the polarized flux is normalized by the unpolarized flux and then fit to a model. Any errors in gains will cancel out. The radio absorption length was also needed, but since the model isn't as sensitive to this parameter as to the dielectric constant, its value is not as critical and an average value of 15 wavelengths was assumed. This number was chosen because it is the approximate average radio absorption length determined from the North data set. And as we shall see in Chapter 5 it is consistent with the results obtained from the re-calibrated South data set. Given these two electrical parameters, the whole-disk brightness temperature at each wavelength was calculated and the South data set was re-normalized to these values.

Calculation of the brightness temperature using this procedure was performed for both the North and South data sets. Ratios of the measured whole-disk brightness temperature to the estimated whole-disk brightness temperature were also calculated. This was done for both the Northern and Southern data sets. The results are shown in Table 5.1. Since, from other indicators, the North data set appeared to be correctly calibrated, it was used as a test of this re-calibration procedure. For the North data set the whole-disk brightness temperature calculated this way differed from the measured value by two percent at 6cm and three percent at 2cm. These differences can be explained by the fact that the measured whole-disk temperature is actually a fit to a uniformly bright disk. Limb-darkening can easily explain this discrepancy. Changing the re-normalization factor for each wavelength by these amounts was considered, but the estimates of the error in the calibration of the North data set do not

warrant making this minor correction. The whole-disk brightness temperature was then calculated for the South data set. The ratios of the measured to the estimated whole-disk brightness temperature show the South data set to be in error by about six percent at 6cm and nine percent at 2cm.

This procedure implicitly assumes that the loss of emission due to surface roughness from low emission angle regions (i.e., near the sub-earth point) is balanced by the increase in emission of regions near the limb. Monte Carlo simulations of a rough surface have been performed by D. Muhleman (private communication) which indicate that this is true to a high degree for surfaces which are characterized by a gaussian distribution of slopes with a FWHM slope of less than fifteen degrees.

The question of the applicability of synthesis mapping to a source which is variable in time is also an issue. Because performing a Fourier transform on the sampled visibility function to a reconstruct the source function is a linear process; the transform of the sum of visibility functions is equivalent to the sum of the transforms. The problem of sampling different regions of the visibility space at different times is not a serious one as long as the source is 'nice'. That is, the source must not have any transient emissions at specific spatial frequencies that may be seen by a certain sampling function but not by a similar, yet slightly different, sampling function. The technique of self-calibration is applied for time intervals much less than the total integration time (on the order of minutes) so the variability of the source should have minimal effect on this process.

The only really non-linear part of the data processing is the de-convolution (CLEAN) process. Because the sampling function is different for each scan (a part of the total integration time lasting about 5 minutes), the beam shape pattern which is the transform of the sampling function, is also different. The de-convolution of what is called the CLEAN image from the dirty (original) image might change for

each scan. Tests were performed to convince us that de-convolving each scan separately and adding together the results appeared to give the same results as adding together the scans in visibility space and then de-convolving the result to get just one CLEAN image. The former process results in a slightly larger resolution element and a slightly noisier image. The equivalence is not obvious and the proof would probably be difficult, and may be true only for slowly changing sources.

CHAPTER 3
THE MODELS

Several different types of models were used to fit the data, depending upon the parameters which were being investigated. Each type of model had its own specific purpose and degree of complexity, ranging from simple uniform temperature disks to a full blown thermal model which uses the thermal inertia and albedo determined from the Viking missions and includes the deposition and sublimation of CO_2 frost. This latter model was treated like the data even down to projecting it on the sky to simulate the data. And of course, along with its own degree of complexity, each model has its own degree of credibility.

3.1 Whole-Disk Models

The whole-disk models were fit to the visibilities and are the simplest. Because they were fit directly to the visibilities, without going through the mapping, CLEANing, and self-calibrating procedures, they are the least subject to interpretational bias. The more steps that go into modeling the data, the more inaccuracies and subtle observer prejudices that can creep in. The first model is the simplest; it just assumes the planet Mars is an elliptical disk of uniform brightness. The visibility function (the Fourier transform of the brightness distribution) of an ellipse of uniform brightness can be calculated analytically, given the size of the ellipse, its flux density, and its location in space, (c.f., Muhleman *et al.*, 1986) and is given by

$$V(\beta) = e^{\Phi} \frac{J_1(2\pi\beta)}{\pi\beta} F_0(\lambda) \tag{3.0}$$

J_1 is the Bessel function of the first kind of order one and $F_0(\lambda)$ is the total flux density of the disk at wavelength λ. Φ is the complex phase shift due to the displacement

of the center of the disk from the phase tracking center (the position on the sky to which the antennae are pointing) and β is the interferometer spacing normalized to the satellite's radius. β and Φ are given by

$$\Phi = 2\pi i(u\Delta\alpha\cos\delta + v\Delta\delta), \qquad \beta = \frac{\sqrt{a^2\cos\psi + b^2\sin\psi}}{D}\sqrt{u^2+v^2} \tag{3.1}$$

Here u and v are the components of the projected baseline in the east and north directions at a given time, expressed in wavelengths. $\Delta\alpha$ is the difference, in right ascension, between the center of the disk and the phase tracking center, and $\Delta\delta$ is the difference in declination. Both have units of radians. The semi-major axis of Mars is a, while b is the semi-minor axis of Mars, also in radians. ψ is the angle between the semi-major axis and the position angle of the baseline, and D is its distance from the VLA to Mars. The position angle of the baseline is the angle between north and the line of the baseline. Whether the baseline is considered to point from antenna A to B or from antenna B to A is not important because the Fourier transform of the visibilities, the image, is real, implying a symmetry through the origin for the UV-plane. For Mars, a was taken to be equal to b. If a and D are in units of kilometers, then a/D is the angular radius of Mars.

Since the response of the VLA is a discrete sampling of the visibility function, no mapping, CLEANing or other post-calibration processing was needed before comparing the data to this simple model. Before fitting this model to the data, the data were averaged over one scan, the length of a scan being about five minutes. For every visibility point in this averaged data base a model visibility was calculated for a given set of parameters. The data were fit by this analytic function using an iterative, linearized least squares routine, where the radius of Mars was taken as known and only the flux density and offsets were allowed to vary. It is important that the position of the disk be allowed to vary as the ephemerides (Vohden and Smith, 1983, 1985) were accurate, in right ascension, only to within about 15-20 percent of the radius

of Mars. This fitting procedure yielded a whole-disk brightness temperature which is equivalent to what a single dish with a beam larger than the planet would yield.

Figures 3.1 and 3.2 illustrate this fitting. To present the data in a comprehensible configuration, the form presented in these figures is not the form in which the models were fit to the data. Both the real and imaginary parts were fit to, whereas here, only the amplitude is shown. Therefore, what looks to be a distinct bias toward small values of the visibility function at large β is actually gaussian noise when looked at from the point of view of a complex number. To produce the curves shown here the data were first binned and then the magnitude was obtained. In addition, the offsets and the whole-disk brightness temperature, as obtained from the fitting were applied to the data before the binning was performed. β is given by Equation 3.1

This simple model of a disk of uniform brightness is not very realistic. It is obvious from the images that there is limb-darkening, as would be expected. However, calculating the whole-disk brightness temperature with several limb-darkened models instead of the uniform disk model yielded whole-disk brightness temperatures only one or two percent different for the best fit limb-darkened models. This is because the whole-disk brightness temperature is the value of the visibility function at zero spacing, i.e., the intercept with the y-axis. Due to a large percentage of the visibility points lying near the origin in the UV-plane, this is the region that is most heavily weighted in the fitting process. Therefore, the fitting of the limb-darkened models do not yield very different intercepts from the fitting of the non-limb-darkened models.

Similarly, the polarized emission from a dielectric sphere can be calculated semi-analytically in a manner similar to that use to derive equation 3.1 (Berge *et al.*, 1972). If this is considered to be the only source of polarized emission, then the whole-disk

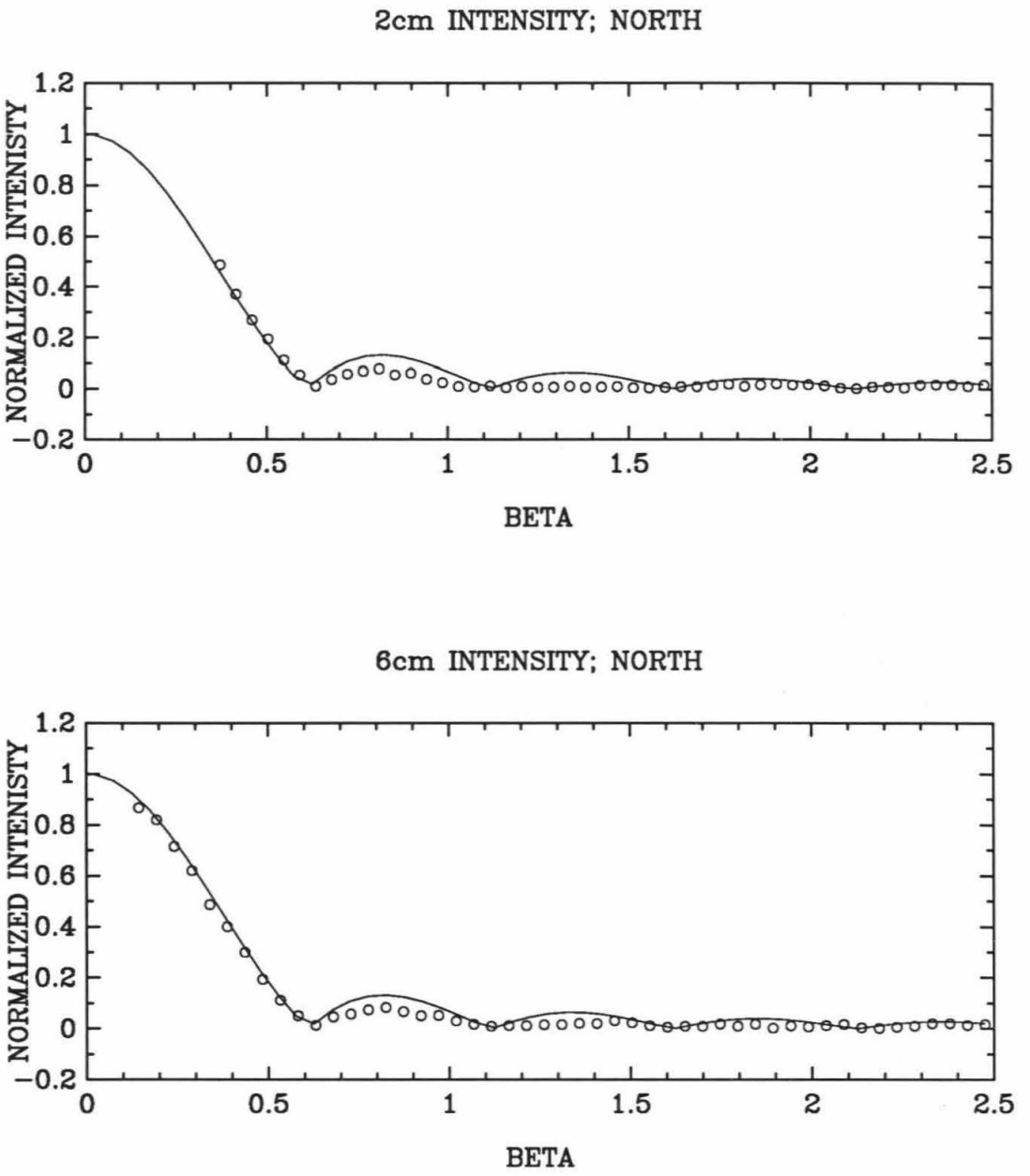

FIGURE 3.1: The top figure is a comparison of the simple whole-disk model to the data at 2cm for the North data set. The bottom figure is the 6cm North data. Both have been normalized by their respective whole-disk brightness temperature.

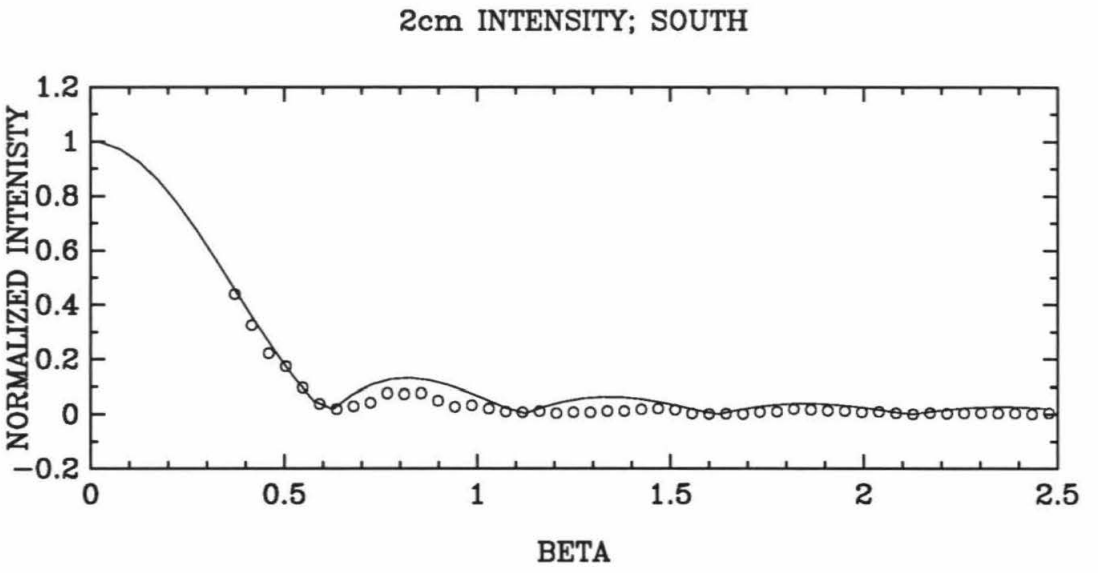

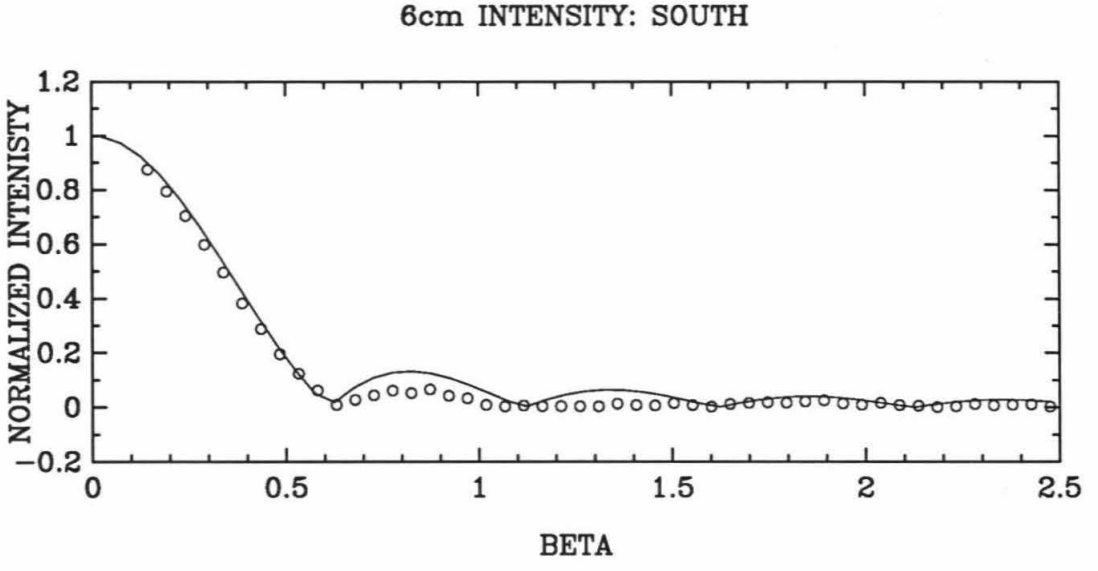

FIGURE 3.2: The top figure is a comparison of the simple whole-disk model to the data at 2cm for the South data set. The bottom figure is the 6cm South data. Both have been normalized by their respective whole-disk brightness temperature.

dielectric constant can be estimated. The polarized intensity is given by:

$$\begin{aligned} I_P^* &= \frac{\mathrm{Re}[e^{\Phi}(V_{RL}+V_{LR})]\cos 2\theta + \mathrm{Im}[e^{\Phi}(V_{RL}-V_{LR})]\sin 2\theta}{I_0(\lambda)} \\ &= \int_0^1 (R_{\|}-R_{\perp})J_2(2\pi\beta\xi)\xi d\xi \end{aligned} \tag{3.2}$$

where I_P^* is the Fourier transform of the polarized intensity. V_{LR} and V_{RL} are the two cross-correlated, cross-polarized components of the visibility data set, and θ is the angle the baseline makes with the east-west direction. These values are all part of the data base. $I_0(\lambda)$ is a constant which can be estimated from the fitting of the whole-disk brightness temperature given above. In addition, J_2 is the Bessel function of the first kind of order two, and $R_{\|}$ and $R_{\perp}$ are the Fresnel reflection coefficients with the electric field vectors in the directions parallel and perpendicular to the plane of incidence, respectively. The Fresnel coefficients are given by:

$$R_{\|} = \left[\frac{\epsilon\cos\phi - \sqrt{(\epsilon-\sin^2\phi)}}{\epsilon\cos\phi + \sqrt{(\epsilon-\sin^2\phi)}}\right]^2, \qquad R_{\perp} = \left[\frac{\cos\phi - \sqrt{(\epsilon-\sin^2\phi)}}{\cos\phi + \sqrt{(\epsilon-\sin^2\phi)}}\right]^2 \tag{3.3}$$

Here ϵ is the dielectric constant of the sub-surface and ϕ is the angle between the radiation being emitted and the normal to the average emitting surface, which can be derived from the observing geometry.

Figures 3.3 and 3.4 illustrate the fitting of the model to the polarization data. Since the percent polarization is already a real number, there is no need to take the magnitude here as was necessary to present the visibility fitting above. Since the polarized intensity is much weaker than the unpolarized intensity, this fitting is not as good as the previous one. However, I hope the figures show that the estimation of the dielectric constant is a relatively accurate one. Again, the offsets, as determined by the fitting of the simple model given in Equation 3.1 to the visibilities, were used to obtain these curves.

The calibration of the data is unimportant for calculating the dielectric constant from the degree of polarization because the polarized intensity has been normalized by

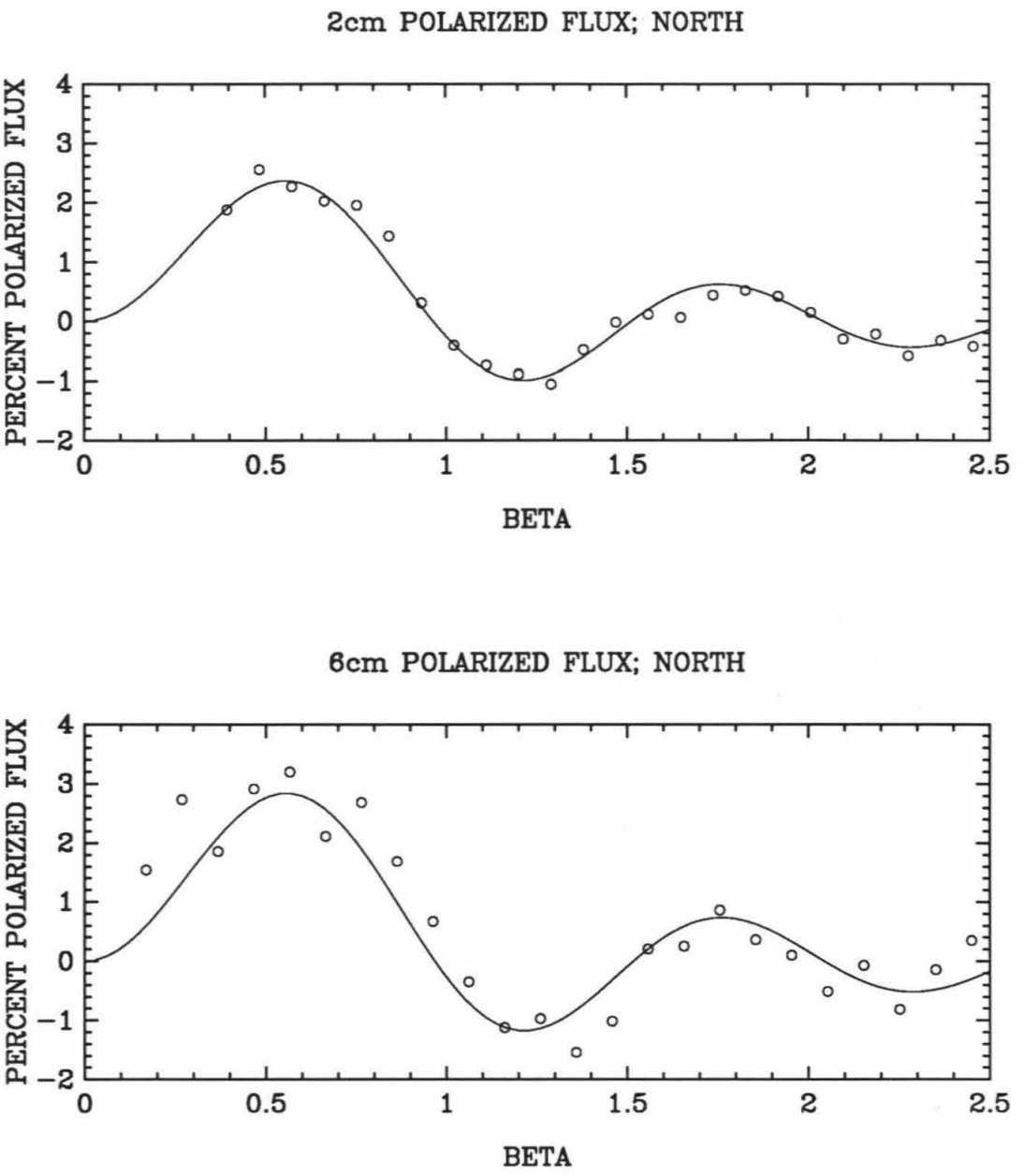

FIGURE 3.3: The top figure is a comparison of the simple whole-disk polarization model to the data at 2cm for the North data set. The bottom figure is the 6cm North data. Both have been normalized by their respective whole-disk brightness temperature to obtain percent polarization.

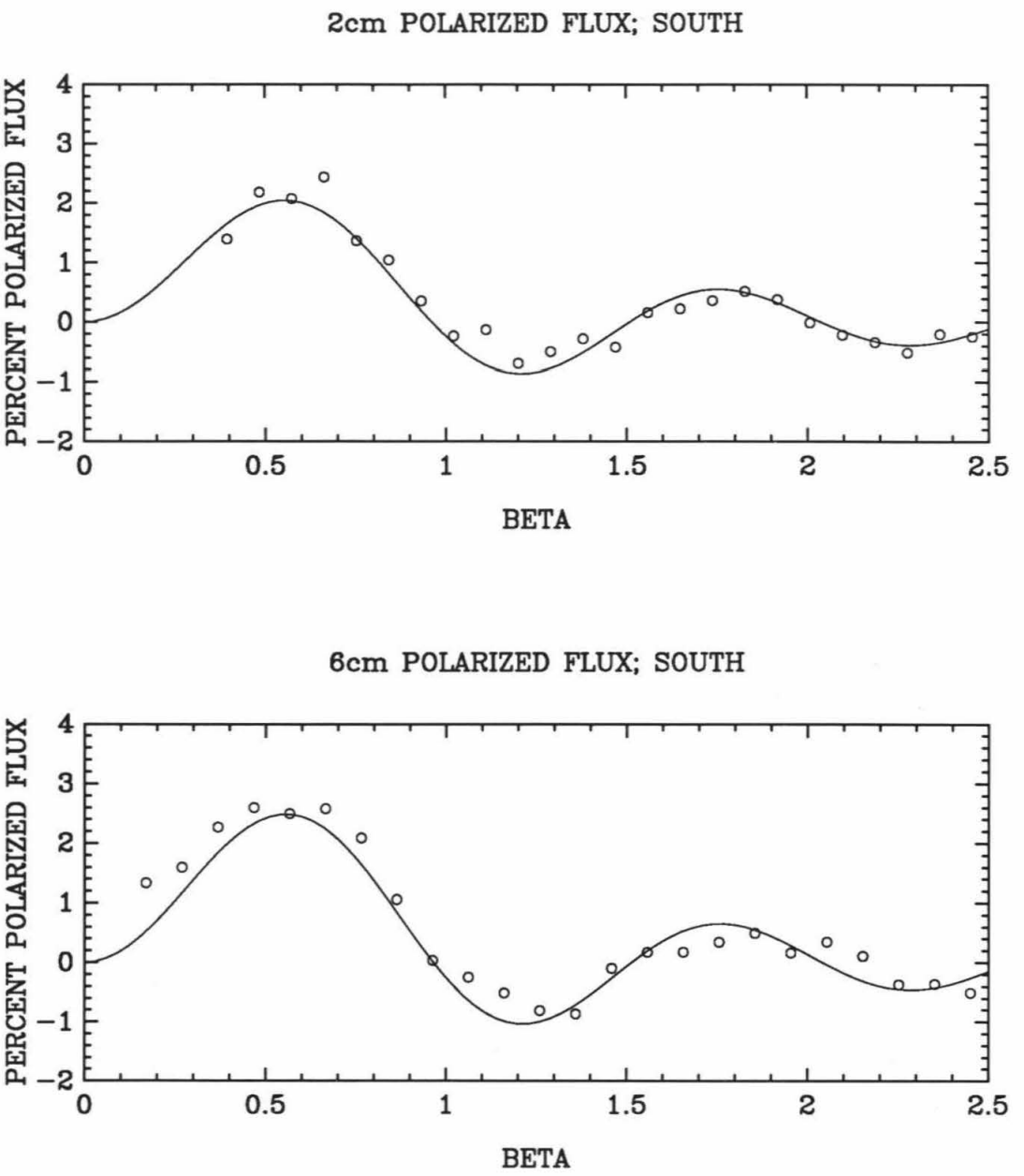

FIGURE 3.4: The top figure is a comparison of the simple whole-disk polarization model to the data at 2cm for the South data set. The bottom figure is the 6cm South data. Both have been normalized by their respective whole-disk brightness temperature to obtain percent polarization.

the unpolarized intensity. This is because the antenna gains that go into estimating V_{LR} and V_{RL} also go into V_{LL} and V_{RR} (which are components of $V(\beta)$) and are, therefore, divided out. So in a sense this parameter is even less dependent upon data manipulation than even the whole-disk brightness temperature. However, it does require the position offsets estimated by the previous model. Fortunately, these offsets are almost completely insensitive to the flux calibration. If these offsets are taken as given, then this semi-analytic model for the polarization has only one free parameter, the disk-averaged dielectric constant. Since the first derivative of equation 3.2 with respect to ϵ is an integral equation, a linearized least-squares fitting could not be performed. Instead, a brute force least-squares routine was used to obtain the whole-disk dielectric constant.

The fitting of the model whole-disk brightness temperature and the model whole-disk dielectric constant was done for each wavelength on each day and then the resulting fits at each wavelength were averaged over the two days in an attempt to reduce the noise. Since the whole-disk brightness temperatures and dielectric constants were calculated directly from the calibrated visibility data without going through the recalibrating, mapping, and CLEANing programs, and since these quantities can also be calculated from mapped data, the whole-disk measurements offer a consistency check on these latter processes.

3.2 Polar Cold Region Models

A second, slightly more sophisticated, model was used to estimate the size and temperature of the Polar Cold Regions. The mapped and CLEANed data were used to fit these parameters. The model was a simple one and consisted of a region of uniform brightness temperature separated at a specified latitude from a second region

of constant, but different brightness temperature. This disk, which was oriented in such a manner as to simulate the data, was then convolved with a gaussian which was the same size and shape as the CLEAN beam and was offset from the center of the map by the amount estimated from the visibilities. The placing of the models so that they lined up with the data is very important because regions that are to overlay each other must do so to within a small error. It is possible that, because of hemispheric differences in the brightness, the center of the disk, estimated from the visibilities in the manner described above, may not be where the center of a best fit circle would be. Since the models start out as circles, this question of lining up the models and the data is especially important because these hemispheric differences obviously exist. Several checks were made to insure that the offsets calculated from the visibilities were accurate and that the models and the data were in line. These checks consisted of visual inspection of both the images and the model images and the results of a circle fitting routine, which proved to be slightly less accurate than visual inspection.

The model images were fit to the data, in a least-squares sense, with the separation latitude and the temperatures of the two regions taken as free parameters. No emissivity effects were taken into account, nor was any limb-darkening, other than the beam effects, applied. Therefore, the results of this fitting are given in terms of the radio brightness temperature. As will be seen later, the radio brightness temperature of the Polar Cold Regions have some interesting, if quantitative, physics associated with them. The relationship of the brightness temperatures of these Polar Cold Regions to possible real, physical temperatures will be discussed in detail in Chapters 4 and 5.

3.3 Thermal and Radiative Models

A third, more complex, set of models was used to fit the electrical parameters to the mapped data. The brightness temperature models were calculated for a suite of values of dielectric constants and radio absorption lengths. Since the only parameters that varied from model to model were the electrical parameters, the same model of the physical temperature as a function of depth, latitude, and longitude was used for all cases. This model of the kinetic temperature of the sub-surface was created by solving the heat equation with constant thermal parameters:

$$\frac{\partial T(x,t)}{\partial t} = \frac{1}{\rho c_p}\frac{\partial}{\partial x}\left(k_t \frac{\partial T(x,t)}{\partial x}\right)$$

where $T(x,t)$ is the physical temperature as a function of the sub-surface depth x and time t, ρc_p is the volume specific heat and k_t is the thermal conductivity. These physical parameters, in the form of the thermal inertia $K = \sqrt{k_t \rho c_p}$, and the albedo were gotten from Palluconi and Keiffer (1981). All thermal inertias presented in this document will be in terms of 10^{-3}cal cm^{-2} sec$^{-1/2}$ K^{-1}. In order to obtain the thermal conductivity, the volume specific heat was assumed to be 1×10^7 erg cm^{-3} K^{-1}. That is, all variability in the thermal inertia is assumed to occur in the thermal conductivity and not in the volume specific heat. This is a relatively good assumption because, for most geologic materials, the variability in thermal conductivity is much larger than the variability in the volume specific heat, which varies, on the average, by factors of two or three. In addition, the square root of this value is taken, cutting down the effect of a change in the volume specific heat even more.

The idea was to solve this equation for an infinite half plane with a lower boundary condition consisting of letting the heat flux go to zero at infinite depth. This is very difficult to do numerically, so the lower boundary condition was approximated by forcing the flux through the bottom boundary to be near zero and, simultaneously

forcing the bottom layer to be deep enough that the temperature did not change by more than one degree during the entire martian year at any latitude. That is, both the derivative with respect to time and with respect to depth of the temperature go to zero at the lower boundary. These restrictions determine the depth of the lower boundary. These limits were chosen because they seemed to be reasonable numbers; not too restrictive, so the algorithm would converge; and not too large, so it would be accurate. Because of the large changes in temperature at the very northern- and southern-most latitudes, the temperature variations with season went deepest in these areas. Thus the depth of the bottom layer was determined by these latitudes. Therefore, at more temperate latitudes the depth of the bottom layer was deeper than needed to nominally satisfy the above criteria. Following the example of others (e.g. Leighton and Murray, 1966; Keiffer *et al.*, 1977; etc.), a modified radiative boundary condition was used at the surface:

$$\frac{S_\odot(1-A^*)cos(\psi)}{R^2(t)} + k_t \frac{\partial T(x,t)}{\partial x}\Big|_{surface} + L\frac{dM_{CO_2}}{dt} + F_a = \varepsilon\sigma T^4(0,t)$$

where the first term on the left hand side is the solar insolation term, $S_\odot$ being the solar constant (whose value was taken to be 1.3533×10^6erg cm^{-2} sec^{-1}, following Thekaekara and Drummond, 1971). A^* is the Bond albedo, R is the heliocentric distance of Mars, and ψ is the angle the incident radiation makes with the surface of a planet at a given latitude, longitude, and time of day. The second term on the left hand side of the equation is the heat flux either going into or coming out of the sub-surface. The third term is the heat lost to the formation or gained from the sublimation of CO_2 frost. The fourth term, F_a, is a radiation backscatter term. Following Keiffer *et al.* (1977) it was given a value of 0.02 of the noontime solar insolation or 0.02 of the value of the surface frost emission, which ever was greater. The only term on the right hand side is the radiative emission term. A value of 1.0 was assumed for ε, the surface infrared emissivity, and σ is the Stephan-Boltzmann

constant.

The exact numerical scheme is discussed in detail in Appendix A and shall only be summarized here. The program is an implicit finite difference scheme based on the Crank-Nicholson algorithm and therefore stable for all values of $\triangle x$ and $\triangle t$. It is second order accurate in both time and space. The program was run with a minor time step of 1/72 of a martian day and depth steps that progressively increase from 1mm to 211cm by increments that begin at 1.2mm and increase by a factor of 1.2 at each depth step. The deepest layer is about 12.7m. After solving for the temperature as a function of depth for one day, the last time step of the current day and the last minor time step of the previous major time step were used to linearly interpolate to the beginning of the next major time step. These three values are all at the same time of day, minimizing the error inherent in this interpolation scheme. The major time steps were placed five martian days apart so that the linear approximation would be accurate, but would give a time savings of a factor of five over solving for each day. Great care was taken to make sure the beginning and endings of each major time step were in synchronization. A sample case was run without this interpolation and it agreed nicely with its counterpart which was run with the interpolation.

This program was run for the equivalent of four martian years even though it appeared to converge after only three years. A caveat here: The program uses the same ephemerides for each of these years, implicitly assuming that the orbit of Mars does not change over a year. So actually the same year is run four times. At the end of this four year period, the temperature as a function of depth and time of day was stored for each day of each observing run. These calculations were done for latitude bins of 5 degrees starting at 87.5°N and extending to 87.5°S. The size of the longitude bins was 5.0 degrees wide and their centers ran from 2.5°W to 357.5°W.

From these temperature profiles the radio brightness temperature at each wave-

length was calculated for each of a set of values of the radio absorption length and effective dielectric constant using standard radiative transfer equations (c.f. Muhleman, 1972).

$$T_B(t) = [1 - R_p(\lambda, \phi)] \int_0^\infty T(x,t) exp\left(\frac{-k_\lambda x}{\cos\theta}\right) \frac{k_\lambda}{\cos\theta} dx \tag{3.4}$$

where T_B is the brightness temperature, θ is the angle at which the radiation from below the ground impinges upon the surface, and is related to the emission angle ϕ by Snell's law of refraction, x is the depth in the sub-surface at which the temperature $T(x)$ occurs, and k_λ is the radio absorption coefficient, which is strongly wavelength dependent and assumed to be inversely proportional to the first power of the wavelength (see Campbell and Ulrichs, 1969; or Muhleman, 1972 for a more detailed analysis of k_λ)

$$k_\lambda = \frac{k_0}{\lambda} \tag{3.5}$$

The radio absorption length is just the inverse of radio absorption coefficient. In addition, the radio emissivity through the surface is given by $(1 - R_p)$, where R_p is the average of the Fresnel reflection coefficients $R_{||}$ and $R_\perp$ for a region about 1 or 2 wavelengths into the surface. For a dielectric constant of 3 and radiation of normal incidence this emissivity is about 0.87.

There were 48 models in all, parametrized with four dielectric constants (1.4, 2.2, 3.0, 3.8) and three radio absorption lengths (5.0, 10.0, 20.0 wavelengths) for each of two days at each of two wavelengths. We used these models to estimate a best fit, in a least squares sense, for each of the model parameters averaged over longitude. Since a brute force least-squares method was used, a linear interpolation between the various models is implied. This fitting was performed after first putting the models in a form similar to the data (i.e., a sphere projected onto the plane of the sky) and convolving them with a point spread function similar to the CLEAN beam.

Because the actual radio absorption length was considered to be proportional to the wavelength, we actually fit this constant of proportionality, which we will call the radio absorption length. This allowed fitting of two dielectric constants and one radio absorption length which is given in units of wavelengths. The dielectric constants referred to in the rest of this work are actually only effective dielectric constants due to the fact that no effort was made to remove the effects of surface roughness. Because the response of a model at one wavelength to a change in dielectric constant is very similar to the response due to a change in radio absorption length, the two wavelengths could not be handled separately to give both a dielectric constant and radio absorption length at each wavelength. The reason for this will be discussed in Chapter 4.

The dielectric constants determined in this manner can be used to estimate the density of the first one or two wavelengths of the sub-surface. This can be done by using the work of Campbell and Ulrich (1969), and others, who have established a relationship between the density of powdered rocks and their dielectric constant. It happens that the dielectric constant of a rock which has been pulverized is more dependent on its density, and therefore its porosity, than upon the dielectric constant of the original rock. There is, of course, some error in the relationship between the density and the dielectric constant, as not all rocks behave in exactly the same manner. This error will propagate itself into the errors of the densities determined in this manner. However, it is a relatively small error and in most cases it is smaller than the formal error obtained in finding the dielectric constant.

CHAPTER 4
NORTH DATA SET: RESULTS AND DISCUSSION

Since several different models were used to fitting several different parameters to several different forms of the data, it is only fitting that the discussion be broken into several different sections. As much cohesion between sections as possible will be maintained, however. The sections will cover the whole-disk results which were determined from directly fitting the visibilities; the North Polar region results, which were fit using a simple two temperature disk model; and finally the latitudinally binned results, from which dielectric constants (and their derived densities), and radio absorption lengths as a function of latitude were derived.

4.1 Whole-Disk Results

The fitted whole-disk brightness temperatures and dielectric constants are listed in Table 4.1. The errors listed in the table are formal errors only (estimated from the least-squares fitting) and do not include any estimate of the systematic errors. An estimate of the calibration error at 6cm is on the order of a few degrees, or about 2%, and is most likely due to inaccuracies in the tabulated flux of the primary calibrator, and atmospheric effects. Because of the inherent difficulties of doing 2cm measurements (phase instabilities due to atmospheric conditions are more prominent by a factor of three than at 6cm) the estimate of the calibration error at 2cm is on the order of 5 to 7 degrees, or about 3 to 4%.

Included in Table 4.1 are some results of observations made by other workers in the field. There is general agreement among all the results in a given category. The whole-disk brightness temperatures are in good agreement with those from other

TABLE 4.1

Northern Data Set Results		
Wavelength	2cm	6cm
Whole Disk Dielectric Constant	$2.34 \pm .05$	$2.70 \pm .09$
Whole Disk Sub-surface Density (g cm^{-3})[a]	$1.24 \pm 0.06 \pm 0.16$	$1.45 \pm 0.10 \pm 0.18$
Whole Disk Brightness Temperature	$193.2\text{K} \pm 1.0$[b]	$191.2\text{K} \pm 0.6$[b]
Normalized Brightness Temperature[c]	$189.0\text{K} \pm 1.0$[b]	$187.1\text{K} \pm 0.6$[b]
1.85cm Bright. Temp., Klein (1971)[c]	$187\text{K} \pm 12$	—
2.7cm Bright. Temp., Mayer *et al.* (1971)[c]	$185\text{K} \pm 12$	—
2.8cm Bright. Temp., Andrew *et al.* (1977)[c]	$194.3\text{K} \pm 3.6$[d]	—
2.8cm Bright. Temp., Doherty *et al.* (1979)[c]	$195.2\text{K} \pm 2.7$[d]	—
6cm Bright. Temp., Kellerman (1971)[c]	—	$196\text{K} \pm 27$
North Polar Cold Region Bright. Temp.	$125.9\text{K} \pm 2.0$[b]	$150.1\text{K} \pm 2.0$[b]
North Polar Cold Region Extent	$69.7° \pm 0.3$	$66.2° \pm 0.6$
North Polar Cap Extent, James (1982)	70.8°	
North Polar Cap Extent, Iwasaki (1984)	67.4°	

[a]The first error is the least squares error and the second error is due to the scatter in dielectric constants for powders of varying origins. (c.f. Campbell and Ulrichs, 1969)

[b]These are formal errors only and estimates of the absolute calibration errors are $\pm 5°$at 6cm and $\pm 7°$at 2cm.

[c]These temperatures have been normalized to a solar distance of 1.524AU using an $R^{0.25}$ power law for comparison purposes.

[d]These measurements were published as functions of longitude and the error shown here is actually the variation over longitude.

workers, giving us confidence that the calibration is good. Much of the discrepancy that is present can be attributed to the fact that different observations were taken at different seasons, different sub-earth time of day, and at different wavelengths. Few other workers have published estimates of the whole-disk dielectric constant. This is because the polarized signal is much harder to measure accurately. Because the VLA has so many baselines, the signal-to-noise inherent in this measurement can be increased. The accuracy with which the model whole-disk brightness temperatures (estimated from the thermal modeling using the fitted whole-disk dielectric constants) agree with the actual whole-disk brightness temperatures will play a crucial role in

the next chapter.

4.2 North Polar Cold Region

The results of the North Polar Cold Region fitting are also listed in Table 4.1, along with some estimates of the extent of the North Polar Cap at this season as measured by other observers. Note the strong agreement between the latitude of the edge of the North Polar Cap and the estimated edge of the North Polar Cold Region. The brightness temperature of the North Polar Cold Region differs between the two wavelengths and is much colder at 2cm than the temperature at which CO_2 sublimates under Martian surface conditions. This is due mostly to the combination of two different effects, one of them physical and one a result of the method of observation.

The first, and most straightforward of these effects, is that the resolution of the 6cm data is one third that of the 2cm data. The estimate of the edge of the North Polar Cold Region from the fit of the lower resolution, 6cm, data will have a larger non-formal error than the estimate from the fit of the 2cm data, which is higher in resolution. If the edge of the North Polar Cold Region is fixed at the 2cm value of 70° N (i.e., the latitude is no longer a free parameter), then the brightness temperature of the North Polar Cold Region at 6cm is only 142K. The second contribution to the difference can be most easily understood by noting that the region which is sampled by the 6cm emission is, roughly, three times deeper than the region sampled by the 2cm emission. Since the radio absorption length of CO_2 frost is very large (it can vary between some tens of wavelengths to over one hundred wavelengths depending on the density of the CO_2 and the soil content, Simpson *et al.*, 1980), it is possible, at certain latitudes, to 'see' through the seasonal frost layer to the ground below, which can be warmer at depth than the sublimation temperature of CO_2. As will be seen

shortly this is exactly the situation that occurs at the season during which the North data set was obtained.

The behavior of the seasonal wave and can be understood through the following, simple argument: At all latitudes, the CO_2 cap is seasonal. This means that sometime during the year the surface gets much warmer than the CO_2 sublimation temperature (Keiffer *et al.*, 1977). Assuming the transport of CO_2 is relatively efficient, the surface temperature remains near the CO_2 sublimation temperature. Therefore, the sub-surface temperature will always be warmer than the sublimation temperature of CO_2, converging at some depth to the seasonal average (assuming minimal heat flow from the deep interior and across latitude ranges). Solutions for the heat equation under these circumstances show that, at a latitude of about 65°N, the temperature at a depth of one seasonal thermal skin depth, about 110cm, will be around 10 to 15 degrees warmer than the CO_2 sublimation temperature during the season in which our measurements were taken.

Figure 4.1 illustrates this warming with depth. The two curves shown in Figure 4.1 are the diurnally averaged kinetic temperature as a function of depth for two seasons. They were computed using the thermal model described in Chapter 3, using a value of 6.5 for the thermal inertia and a value of 0.25 for the albedo. The solid line corresponds to the season during which the North data set was taken. The dotted lines corresponds to late summer in the northern hemisphere. Both were calculated for a latitude of 62.5° N. Note the positive thermal gradient for the line corresponding to the season during which the North data set was taken. In late fall the thermal gradient is just the opposite as the summer heat wave propagates into the sub-surface.

In addition, the CO_2 frost acts as a dielectric 'film' coating the surface so that the angle of emission from the sub-surface to the frost is much nearer the vertical than it would be if the emission were to come directly through the surface-atmosphere

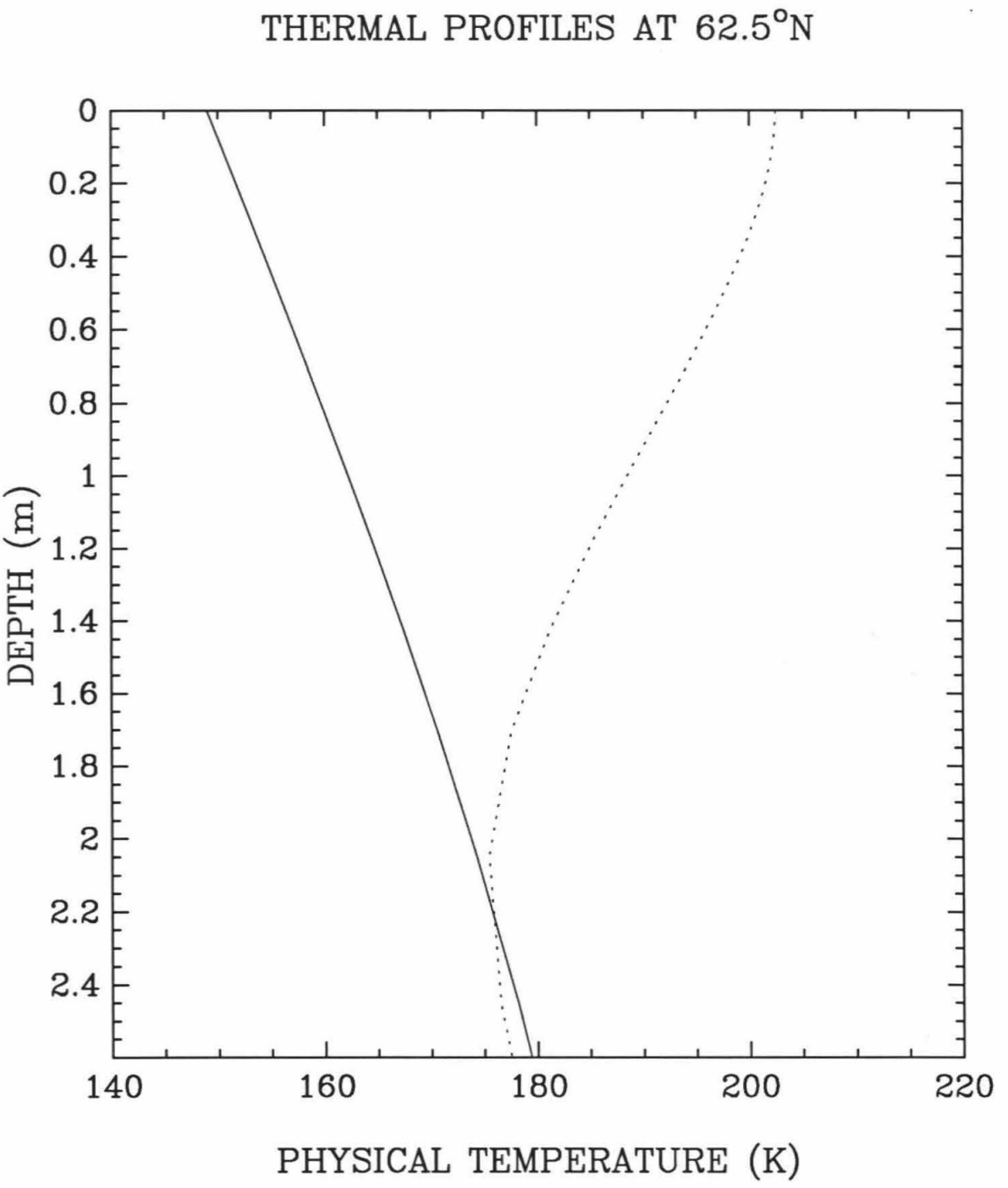

FIGURE 4.1: Physical temperature of the sub-surface for two different seasons at 62.5° N. The solid line is for $L_S = 67°$ (late spring) and the dotted line is for $L_S = 164°$ (late summer).

interface. Because of this, the change in angle at each interface is less dramatic than for a single interface, and the radio emissivity due to the Brewster angle effect, is, therefore, greater. For reasonable values of the surface dielectric constant (e.g. those in the table) and a value of 2 for the dielectric constant of the CO_2 frost, it turns out that the emissivity of the surface, at a latitude of 70°, is about 0.87 as opposed to 0.83 for the non-coated surface.

Thus, it is not surprising that the temperatures of the North Polar Cold Region are warmer than the sublimation temperature of CO_2, and that the 6cm results are warmer than the 2cm results. However, these effects are modified by the actual amount of CO_2 frost present. The CO_2 frost also contributes to brightness temperatures of the North Polar Cold Region. The dirtier the frost, the larger its contribution to the radio brightness temperature. The maximum seasonal accumulation of CO_2 frost in the north has been estimated at about 75 g cm^{-2} (Paige and Ingersoll, 1985), which, if it has the density of packed dry ice, $\rho = 1.56$ g cm^{-3} (Weast *et al.*, 1965), would form a layer about half a meter thick, which is smaller than the radio absorption length, which would be expected to be about 30 or 50 λ, if clean. Because the thickness of the seasonal CO_2 cap would be expected to increase with latitude, you would expect that the CO_2 frost layer would contribute more and more to the brightness temperature as latitude increased.

In addition, at the higher latitudes the seasonal cap is present for more of the year, and the sub-surface temperature gradient is, therefore, smaller. All of these factors taken together imply that the radio brightness temperature at the higher latitudes will be nearly that of the CO_2 frost alone. We assume an isothermal temperature profile through the CO_2. The reasoning behind this is as follows: The surface temperature is moderated by the sublimation and condensation of CO_2 frost, assuming transport of CO_2 gas is efficient, so the surface of the layer stays at the sublimation temperature.

We assume that as the bottom layer of the CO_2 warms up from the heat flowing from the sub-surface, the CO_2 sublimates at this boundary in such a way that the heat flux is transported rapidly to the top of the CO_2 layer, either through diffusion of the gas through the layer or the exchange of heat via sublimation and condensation of different sections of the layer.

As a test of the hypothesis that the radio brightness temperature should approach the brightness temperature of CO_2 frost alone as latitude increases, the latitude of the North Polar Cold Region was varied from its value in Table 4.1to 80° N and just the brightness temperature of the North Polar Cold Region was fitted to the data. The 2cm brightness temperature stayed relatively constant as the edge of the model was moved north, while the 6cm brightness temperature decreased until it agreed with the 2cm temperature, to within the error bars. This can be seen somewhat in Figures 4.2 and 4.3, although the effect is masked by the effect of the convolving gaussian. This agreement occurs when the edge of the model cold region is at about 76° N and both brightness temperatures are about 128K (129K±7 at 6cm and 128K±3 at 2cm).

The sublimation temperature of solid CO_2 is about 148K; the exact temperature depending upon the surface pressure of the CO_2 atmosphere The dielectric constant needed to give a brightness temperature of 128K±3 from a physical temperature of 148K, assuming a smooth emitting surface and an average emission angle of approximately 70° , is about 2.5±0.3. An error of three degrees in brightness temperature translates to an error of 0.3 in dielectric constant. Simpson *et al.* (1980) made measurements of the dielectric constant of solid CO_2 as a function of density. Using their fit and the Rayleigh mixing formula (Campbell and Ulrichs, 1969), a dielectric constant of 2.5 yields a density of CO_2 of 1.7±0.3 g cm^{-3}. The value of the density of solid CO_2 taken from the CRC handbook is 1.56 g cm^{-3} (Weast *et al.*, 1965) which is equivalent to a dielectric constant of 2.25. This can be related to a brightness

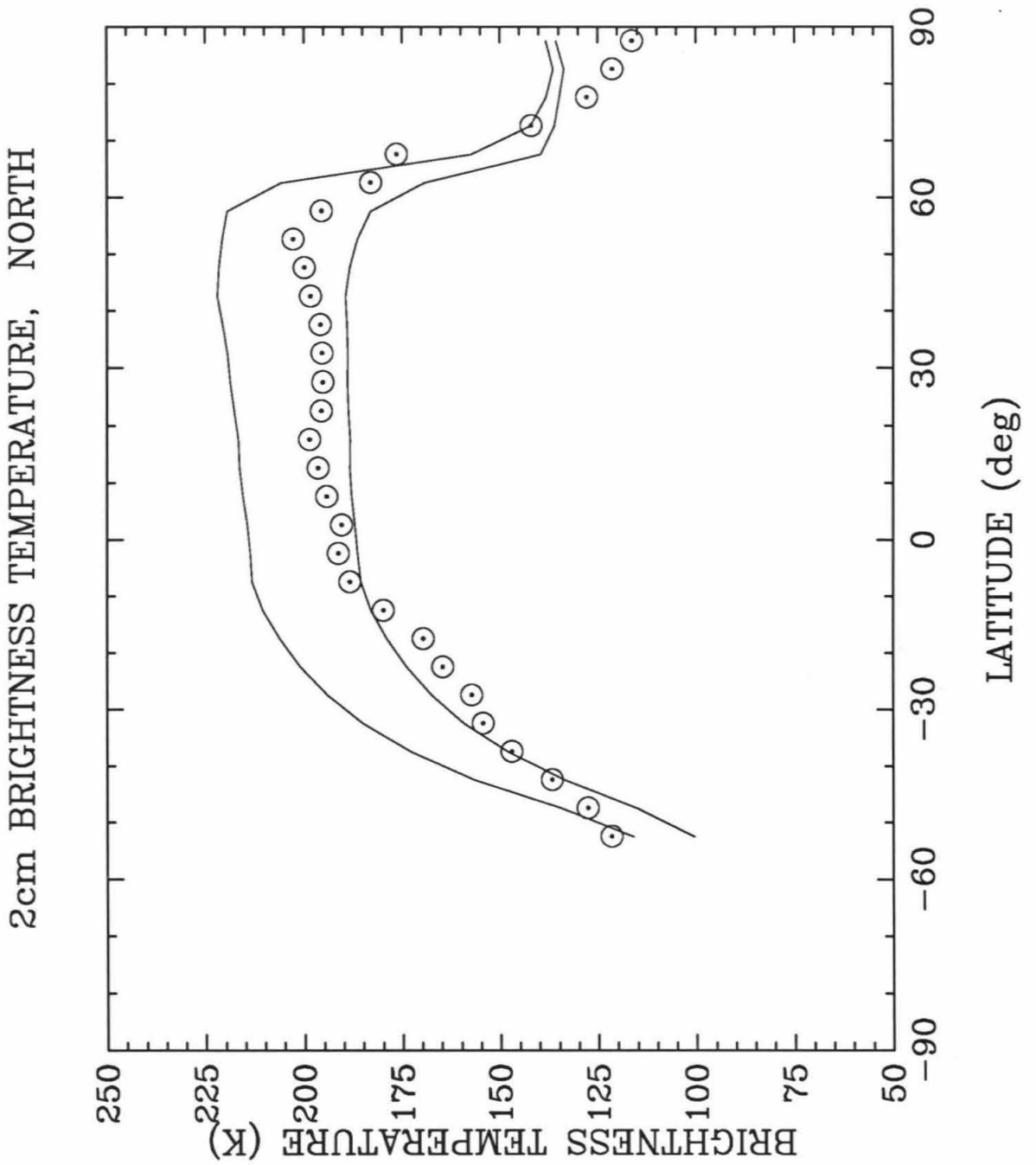

FIGURE 4.2: Longitudinally averaged 2cm brightness temperatures as a function of latitude. The upper line is the model which had a dielectric constant of 1.4 and a radio absorption length of 5.0 wavelengths. The lower line is the model which had a dielectric constant of 3.8 and a radio absorption length of 20.0 wavelengths. The sub-earth latitude was 24.8°N.

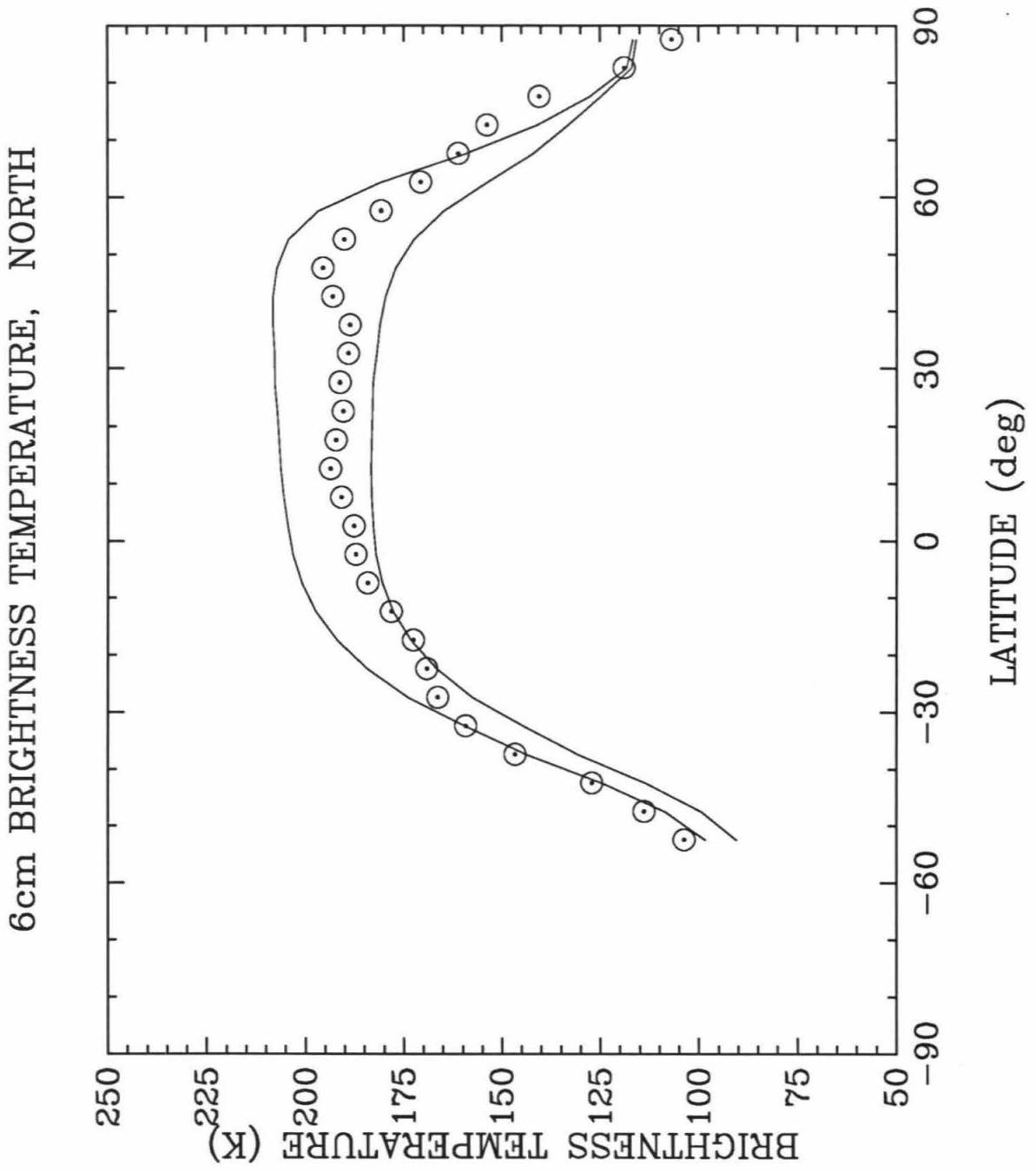

FIGURE 4.3: Longitudinally averaged 6cm brightness temperatures as a function of latitude. The upper line is the model which had a dielectric constant of 1.4 and a radio absorption length of 5.0 wavelengths. The lower line is the model which had a dielectric constant of 3.8 and a radio absorption length of 20.0 wavelengths. The sub-earth latitude was 24.8°N.

temperature for the North Polar Cold Region of 129.5K. Unfortunately, because of the large error bars on the determination of the dielectric constant, there is not a strong limit on the density of the CO_2 frost determined in this manner.

However, since reasonable changes in density, and therefore dielectric constant, cause rather minor changes in the radio brightness temperature, the North Polar Cold Region brightness temperature does give us faith that our calibration is off by less than 5K at either wavelength, which translates into an error of less than 3% at both wavelengths. The higher temperature at 6cm at latitudes between the edge of the North Polar Cold Region and 76° N indicates that up to that latitude the emission we are receiving is coming from a region below the CO_2 frost layer. This is not surprising because the CO_2 North Polar Cap ultimately recedes to a very high latitude and may disappear altogether (c.f. Paige and Ingersoll, 1985).

As stated above, the annual frost deposition probably does not exceed one meter, (unless the frost is very fluffy) consequently, we are probably just seeing into the sub-surface to a depth where the temperature is warmer than the surface temperature. At higher latitudes the brightness temperature during the season we observed would be expected to be close to that of CO_2 frost. This is because even though the radio absorption length of CO_2 frost is large, at very northern latitudes the CO_2 layer is thicker and the sub-surface temperature gradient is smaller and so would contribute little to change the brightness temperature from the isothermal case. Of course, if the CO_2 frost has a high soil content, then its radio absorption length will decrease, and it will contribute more to the radio brightness temperature. Unfortunately, because of the large parameter space for many of the critical variables (CO_2 density and radio absorption length, sub-surface thermal inertia, albedo of the rock surface, etc.) and their degeneracy, it is not possible from our data to make an estimate of either the soil content or the thickness of the CO_2 frost.

4.3 Latitudinally Binned Results

The dielectric constant has been measured by both ground-based radar and the Viking bi-static radar experiment. Radar estimations of the dielectric constant are slightly higher than those calculated from the thermal emission. This is many times the case, and explanations for this discrepancy are usually not very rigorous and mostly unsatisfactory. One explanation for the difference is that, the radar estimation, like the dielectric constant estimated radiometrically, can be masked by the effects of surface roughness. However, due to the radar backscatter law, the radar results are more susceptible to sub-surface discontinuities such as rocks than are the radio thermal emission results. With this in mind a brief review of the results of other workers in the field is in order.

Pettengill *et al.* (1973) measured the radar cross-section per unit area and inferred the dielectric constants of the surface of Mars from ground based radar at a wavelength of 3.8cm. They performed these measurements for areas in the region between latitudes 14° S and 22° S and between longitudes 70° W and 110° W. They found that the dielectric constants so determined varied over this region from around 1.7 to about 5. Unfortunately this region is nearly complementary to the region measured during this observation run so a direct comparison is not possible. Downs *et al.* (1975, 1973) also did a radar measurement. Their measurements were made at a wavelength of 12.6cm and in a band circling the globe between the latitudes 14° S and 22° S. They measured an average reflectivity of 0.07 with large variations (on the same order as the average). These variations partially correlate with variations in the thermal inertia. For normal incidence this reflectivity translates into a dielectric constant of slightly less than 3.0.

Harmon and Ostro (1981) performed a radar experiment which separated the

diffuse and specular components. The specular component is much more useful in determining the reflectivity than the diffuse component. They made several measurements of which only two are in the region covered during the North observing run. For the region centered on 39.8°W, 24°N, they found a reflectivity of 0.13 and for the region centered on 330.2°W, 24°N, they found a reflectivity of 0.061. These translate into dielectric constants of 4.6 and 2.8, respectively. Simpson and Tyler (1981), using the Viking orbiter, performed a bi-static radar experiment at wavelengths of 13cm and 3.6cm and found that the dielectric constant in the very northern latitudes ($\phi > 60°$) was relatively low, between 2 and 3, and seemed to decrease with latitude. At lower latitudes ($\phi < 20°$) they estimate a dielectric constant between 3.0 and 3.2 at longitudes near 250° W. Historically, there has often been a discrepancy between electrical properties as measured by radar and those measured by radio thermal emission, see Golden (1979); Muhleman (1972); Hagfors and Moriello (1965) and others.

Although the radio absorption length is on the order of 15 wavelengths, the dielectric constant estimated from our measurements is the value in the region one or two wavelengths below the surface. This is because it is the emissivity that determines the dielectric constant. And the emissivity, which is due to the interface of two different dielectric constants, is affected only by the first one or two wavelengths. Radiometric emissivity and polarization measurements are sensitive to the near surface as are the radar experiments. Although both are sensitive to nearly the same region (at the same wavelength), the radar measurements are more sensitive to surface and sub-surface roughness (see Muhleman, 1972). The low-incidence, bistatic radar is sensitive to the surface roughness in a slightly different way, as well as having to contend with the shadowing problem. As a consequence, all of our estimates of dielectric constant, which are at or below 3, are not out of line with these other workers. A comparison of radar and thermal characteristics can be found in Jakosky

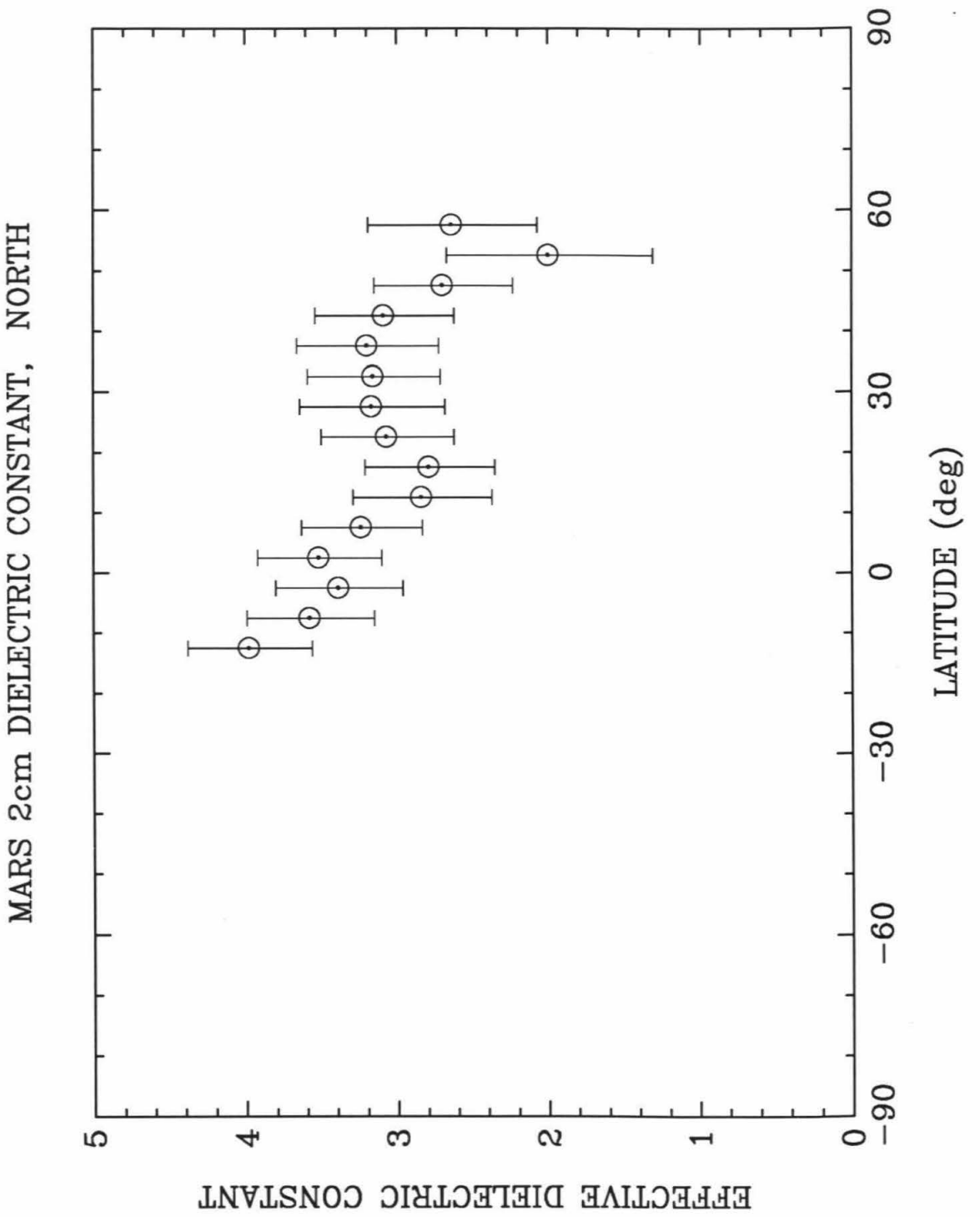

FIGURE 4.4: The data points are the longitudinally averaged 2cm effective dielectric constants as a function of latitude. The error bars shown are formal errors only and do not take into account systematic errors such as calibration errors.

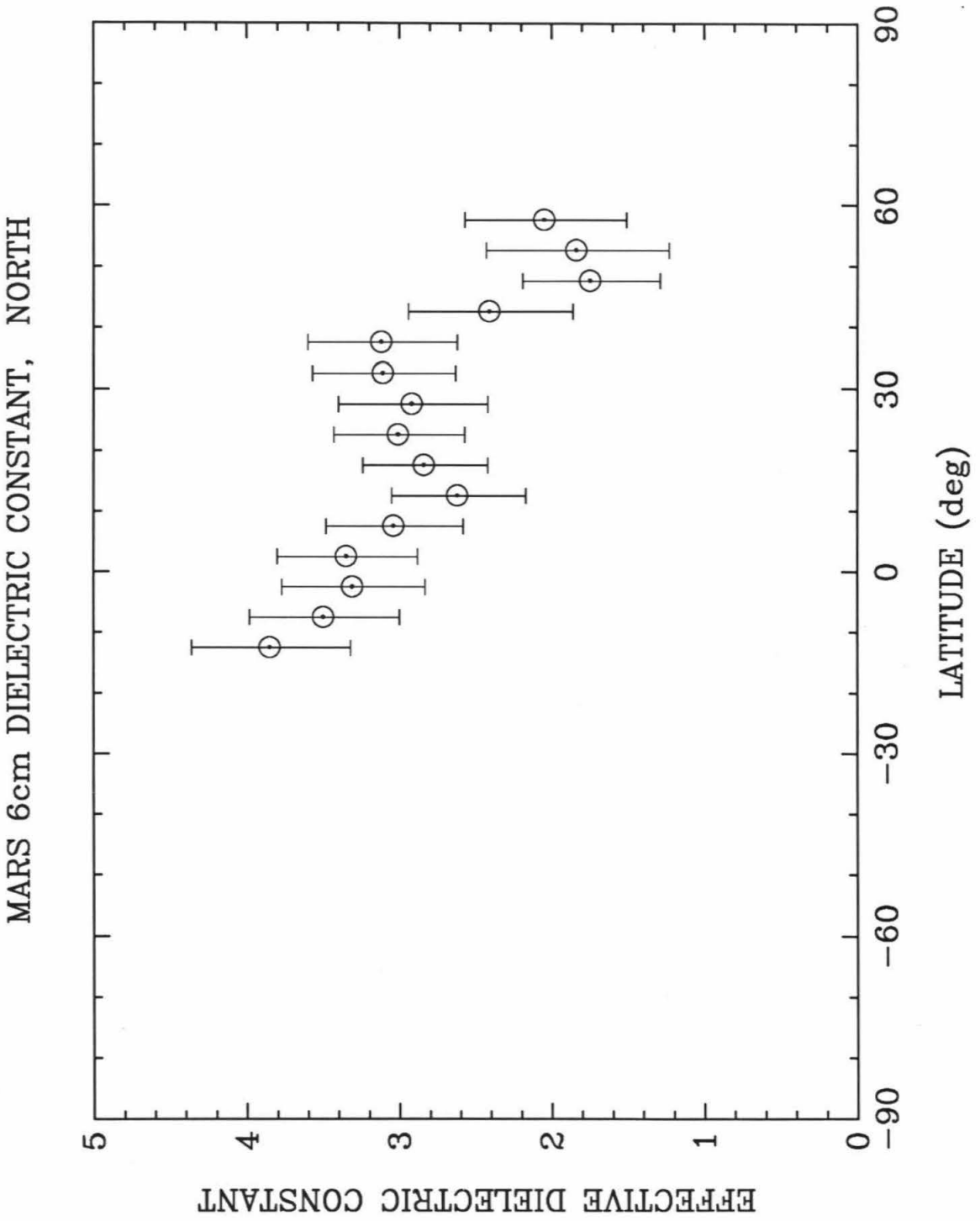

FIGURE 4.5: The data points are the longitudinally averaged 6cm effective dielectric constants as a function of latitude. The error bars shown are formal errors only and do not take into account systematic errors such as calibration errors.

and Muhleman (1981) and Jakosky and Christensen (1986). Both show a correlation between thermal inertia and the radar reflectivity, similar in nature to the correlation between thermal inertia and dielectric constant discussed here.

The brightness temperatures averaged over longitude for each wavelength are shown in Figure 4.2 and 4.3. The two extremes of the suite of models which were fitted to the data are also shown. The brightness temperatures were averaged into 5° latitude bins starting at 87.5° N. Note the strong correlation between the two wavelengths. Both wavelengths show a dip in brightness temperature at about 35° N, and both wavelengths exhibit behavior not well predicted by the suite of models at latitudes between 15° S and 35° S. The strong curvature at southern latitudes is due to the effects of the beam shape function and the radio emissivity. The drop at the northern end is due to these effects and, more noticeably, the North Polar Cold Region. The gentleness of the edge of the North Polar Cold Region in both the data and the model at 2cm is mostly due to the beam shape function and at 6cm partly due to the beam shape function and partly due to actual temperature variations.

In the models the edge of the North Polar Cold Region is very sharp, but since these have been convolved with a gaussian of the same size as the CLEAN beam, this edge has been smoothed. The slope of the smoothed edge of the model is pretty well consistent with the data in the 2cm case. This implies that, as seen at 2cm, the edge of the North Polar Cold Region is a sharp boundary. However, in the 6cm case, the slope of this smoothed edge is steeper than the data. This implies that, as seen at 6cm, there is no sharp edge to the North Polar Cold Region. This may be due to a poor estimate of the thermal parameters above 60°N.

It should also be stated that no attempt was made to adjust the models so that the edge of the Polar Cap in the models coincided with the edge of North Polar Cold Region in the data. This means there is a slight offset between the edge of the North

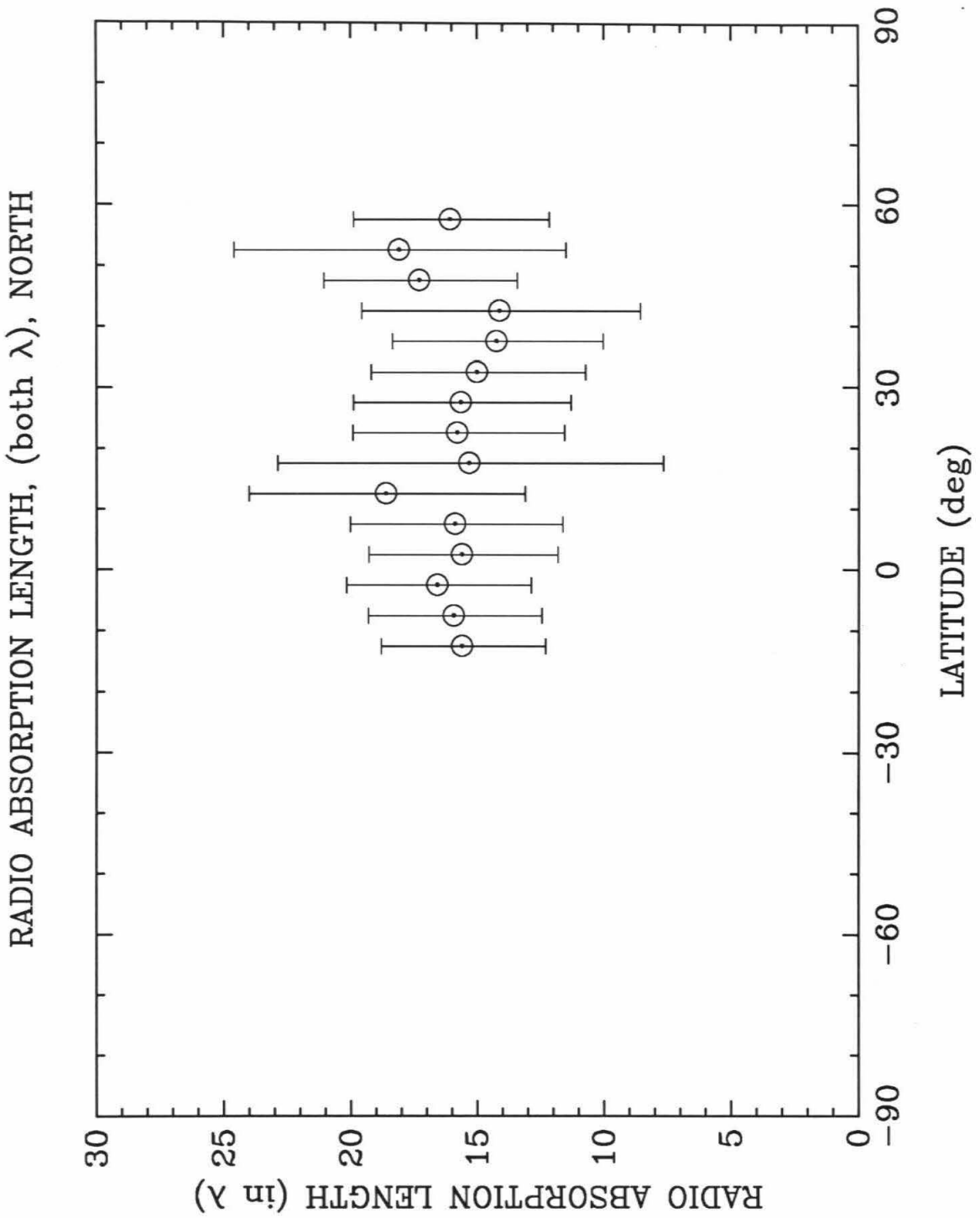

FIGURE 4.6: The data points are the longitudinally averaged radio absorption lengths (both wavelengths) as a function of latitude. The error bars shown are formal errors and do not take into account systematic errors such as calibration errors.

Polar Cold Region in the maps and the North Polar Cap in the models. This has little effect on the results of estimating the electrical properties as no fitting of these properties was done above 60° N because no good values of the thermal inertia and albedo were available for the thermal model. It may be possible, with measurements at several more wavelengths, to estimate average values for both the electrical and thermal parameters from the radio data. The estimated edge of the North Polar Cold Region and the edge of the North Polar Cap in the models were both above 60° N. No fitting of electrical parameters was done below 35° S because below this latitude surface roughness begins to play an important role. This is because these latitudes are near grazing incidence. Unfortunately, the dip in brightness temperatures which begins at about 15° S casts doubt upon the validity of any estimates south of even this latitude. As will be seen in the next chapter, this is a difficult area to fit even when the incidence angle is near normal.

Effective dielectric constants as a function of latitude for each wavelength are shown in Figures 4.4 and 4.5. These values were estimated by fitting Equation 3.4 to the latitudinally binned data, i.e. $R_p(\lambda, \phi)$ was estimated. The error bars are formal errors only, absolute errors being estimated at an additional two to four percent. The latitude dependence of the dielectric constant at one wavelength is strongly correlated to that of the dielectric constant at the other wavelength, reflecting the correlation seen in the plots of brightness temperature. The longitudinally averaged radio absorption length as a function of latitude is shown in Figure 4.6. Except for two or three points, it is relatively constant as a function of latitude, suggesting a high degree of sub-surface homogeneity. The results here are similar to the radio absorption length inferred for the sub-surface of the Moon. This is surprising, since the geologic maps of Mars would suggest latitude averages of block-mass density, and scattering due to sub-surface inhomogeneities would vary at these wavelengths. In

addition, as will be shown later, the average of about 15 wavelengths will also be about right for the average radio absorption length determined by the South data set.

Figures 4.7 and 4.8 show the correlation of thermal inertia (Palluconi and Keiffer, 1981) with the estimated effective dielectric constant at each wavelength. Unfortunately, because of the way our estimates must be made, it is not possible to do this correlation point by point and then average into latitude bins. Instead, the thermal inertia maps were averaged in such a way as to make them similar in form to the data. The 6cm dielectric constant is relatively well correlated with thermal inertia, while the 2cm dielectric constant is slightly better correlated. If the four northern most points were excluded (the solid circles), the correlations at both wavelengths would be even stronger; we note that these northern-most points lie above a strong discontinuity in thermal properties. Both thermal inertia and dielectric constant depend on the density of the sub-surface. Although the infrared radiation comes from a very small emitting region, the thermal inertia determined from it is probably a good estimate of the thermal inertia for one diurnal skin depth (which is on the order of several centimeters). The 2cm emission, coming from a region closer to the surface than the 6cm emission, would tend to be more strongly correlated with surface properties. This would show up in a stronger correlation of thermal inertia with the 2cm dielectric constant than with the 6cm dielectric constant.

One problem with trying to interpret the radio data is that if only one or two observations are made of the same region at the same season, some of the electrical parameters are nearly degenerate in their effect on the radio brightness temperature. This is the reason that, even though we try to keep the assumptions to a minimum in interpreting the data, the assumption that the radio absorption length was proportional to the wavelength was used. How this helps to resolve the degeneracy will

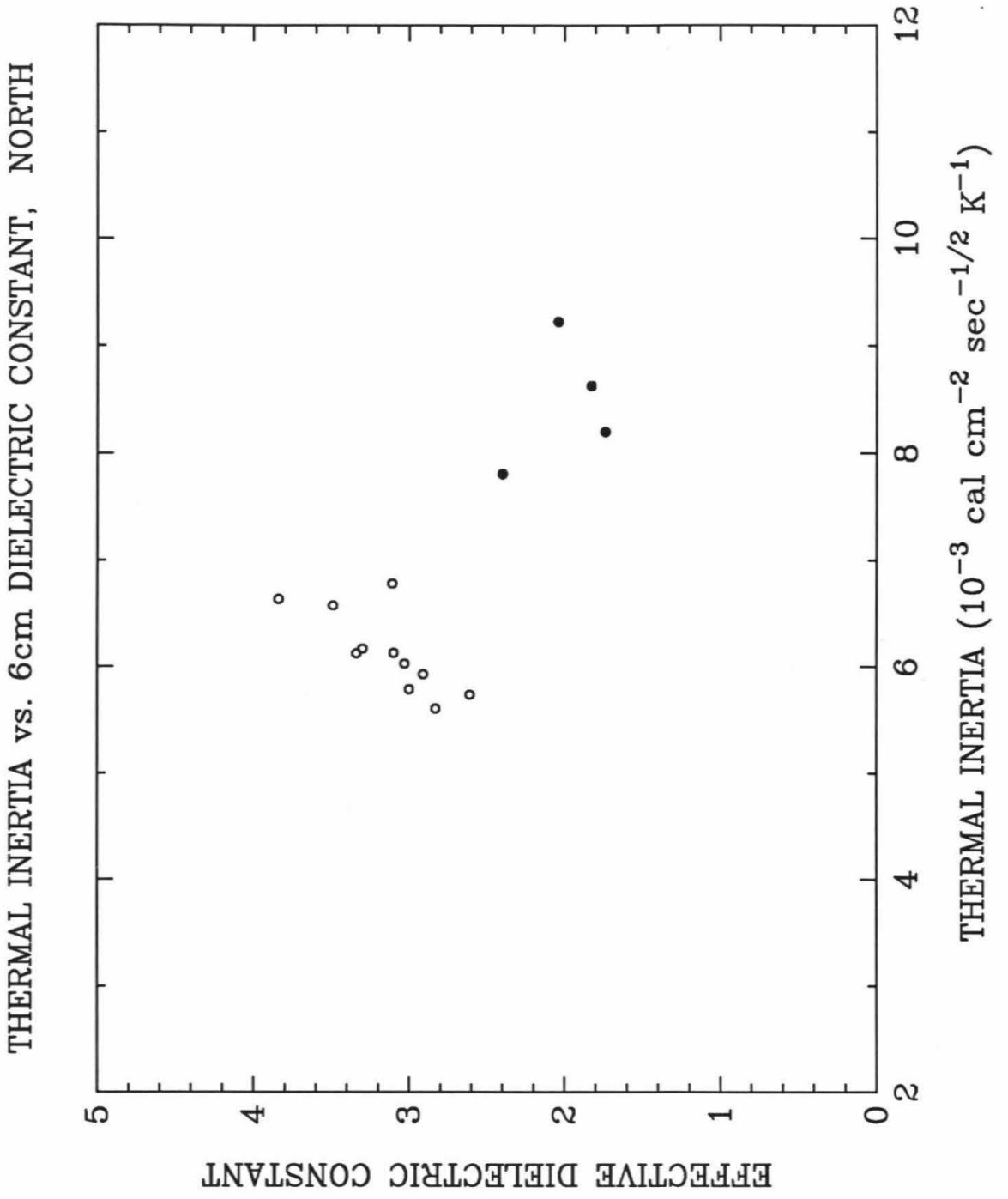

FIGURE 4.7: The correlation of the longitudinally averaged 2cm effective dielectric constant with the thermal inertia, averaged in the same manner as the data, is shown. The filled circles are those whose latitude is above the northern temperature discontinuity.

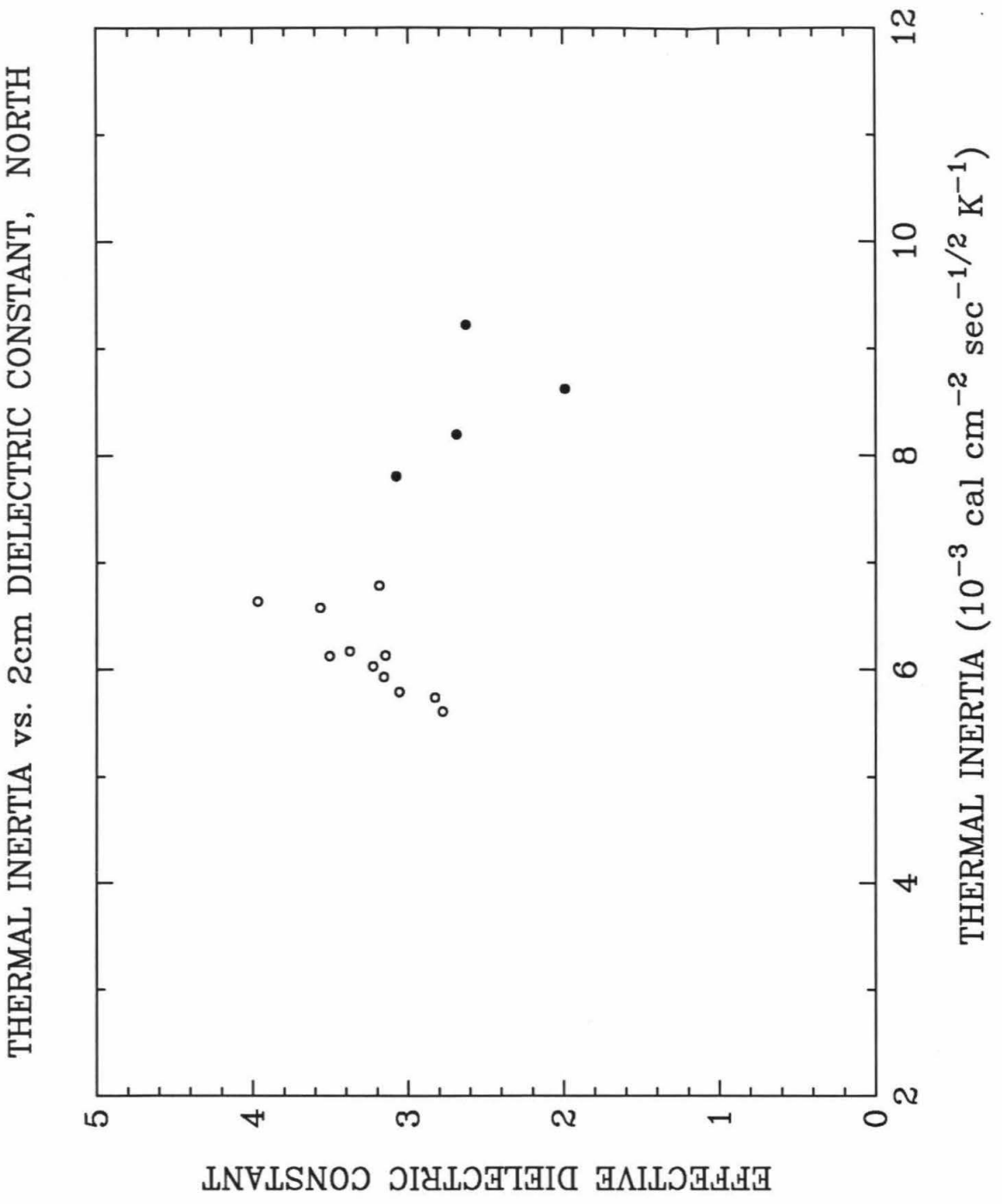

FIGURE 4.8: The correlation of the longitudinally averaged 6cm effective dielectric constant with the thermal inertia, averaged in the same manner as the data, is shown. The filled circles are those whose latitude is above the northern temperature discontinuity.

require a little foray into the effect of each of the parameters on the radio brightness temperature. At most latitudes south of the North Polar Cold Region, the radio absorption length is about 15 wavelengths with large error bars. This translates to a region of sampling down to about 30cm for a wavelength of 2cm and about 90cm for a wavelength of 6cm. Using the average thermal properties of Keiffer *et al.* (1977) a diurnal thermal skin depth of about 4cm and a seasonal skin depth of about 108cm are found. From this it can be seen that at 6cm the region affected by the diurnal thermal wave is a small fraction of the total region sampled. At 2cm the region from which the radiation is emitted is not as deep as at 6cm and therefore the diurnal thermal wave region plays a more important role, but not an overwhelming one. Therefore, the diurnal wave is of relatively little use in determining the electrical parameters.

The effect of changing the dielectric constant in the models is to change the overall brightness temperature but the effect upon the limb darkening curve is minimal, except near the limb. Lowering the dielectric constant in the model raises the flux density coming from all parts of the disk, not uniformly, but the variation is small away from the limb. The effect of changing the radio absorption length in the model is to sample a different region of the sub-surface. However, since the region in which the diurnal wave is important is a very small part of the region contributing to the 6 cm emission and a small, but not insignificant, part of the region contributing to the 2 cm emission, what is mostly sampled is the seasonal wave. This means that for any point on the disk at a given latitude, the sampled temperature profile is very nearly the same and only the weights for different depths vary from one point on the disk to another. This would not be true if the diurnal wave were important; the sampled thermal profile would then vary greatly across the face of the disk.

It is also true that, since the dielectric constant of the sub-surface is not unity, the emission coming from the sub-surface comes from a direction not far from the normal

to the surface for most locations on the disk (recall that the sub-surface incident angle is related to the emission angle by Snell's law). Again, the exception is near the limb, where emission angles approach 90°. This means that even the weights are very nearly the same for all points on the disk, except near the limb. This, in turn implies that changing the radio absorption length will mostly change the overall brightness temperature, with minor variations as a function of longitude. Therefore, the difference between changes in the model brightness temperature due to a change in dielectric constant and changes in the brightness temperature due to a change in radio absorption length, at a given wavelength, are very subtle. Add the usual noise to the data and the separation of these two parameters becomes nearly impossible. This is why data from one wavelength were not used to estimate both dielectric constant and radio absorption length.

However, the 6cm emission samples a different region of the temperature profile than the 2cm emission and using both wavelengths, and the assumption that the radio absorption length is proportional to wavelength, the separation of the two effects becomes possible. The large error bars on the radio absorption length versus latitude plot are witness to the difficulty of this separation. It should be noted that a nominal change in dielectric constant changes the brightness temperature much more than a similar nominal change in radio absorption length. A change of radio absorption length from 10λ to 20λ carries with it a change of about 4K, whereas a change of dielectric constant from 3 to 4 carries with it a change in the model's longitudinally averaged brightness temperature of about 10K. Our results for the absorption length are remarkably similar to those measured on the Moon (Muhleman, 1972).

From the work of Campbell and Ulrichs, (1969) and others, it is known that the dielectric constant of a powdered substance is much more dependent upon its density than upon its original composition. So, the density of the near sub-surface

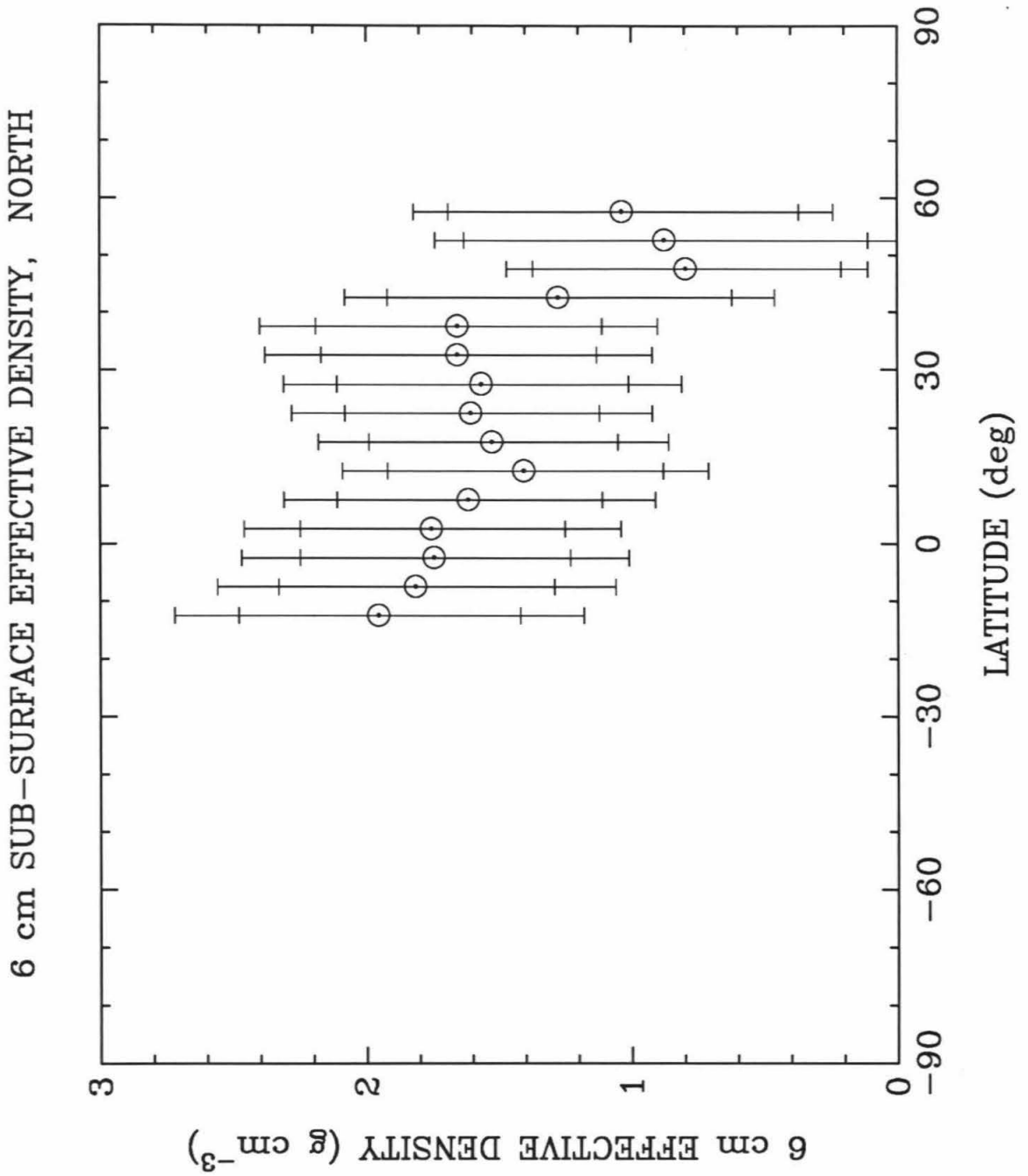

FIGURE 4.9: Estimates of the effective 2cm sub-surface density calculated from the effective dielectric constants. The inner error bars are directly derived from the error in estimating the effective dielectric constant. The additional error that goes into making the outer error bars is due to the spread in dielectric constants among the powders used to derive the empirical relation.

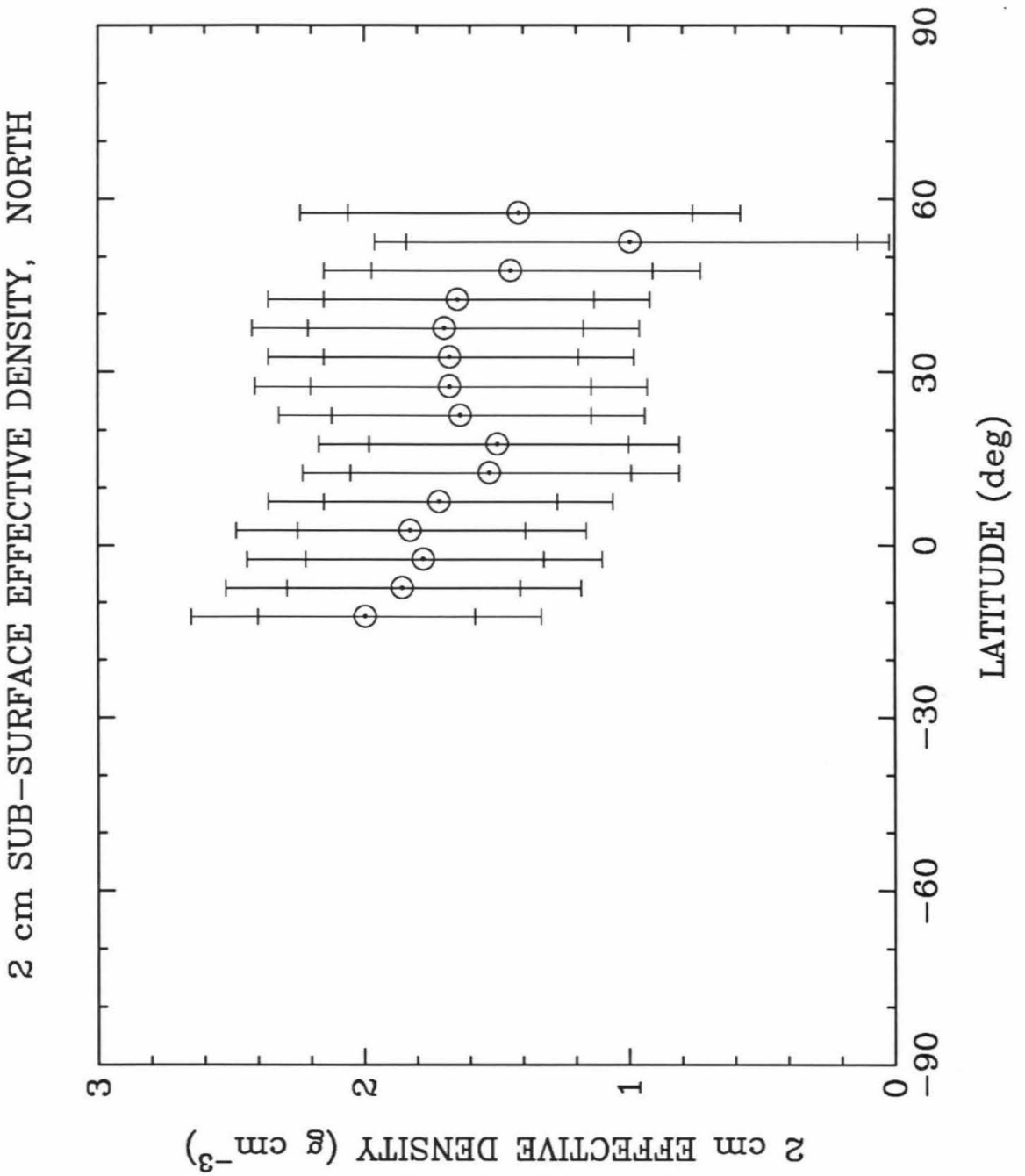

FIGURE 4.10: Estimates of the effective 6cm sub-surface density calculated from the effective dielectric constants. The inner error bars are directly derived from the error in estimating the effective dielectric constant. The additional error that goes into making the outer error bars is due to the spread in dielectric constants among the powders used to derive the empirical relation.

material can be estimated from just the dielectric constant. Using the Rayleigh mixing expression and a dielectric constant of 2.0±0.1 for a powder of density 1 g cm^{-3} (see Campbell and Ulrichs, 1969), the effective density was estimated for each wavelength at each of the latitudes for which a dielectric constant was calculated. The results are shown in Figure 4.9 and 4.10. The inner error bars are calculated from the errors in the dielectric constant. The outer error bars are an additional, combined error due to the scatter in the dielectric constant of the powders of rocks of different types. The additional error was estimated from the data of Campbell and Ulrichs and was determined to be 0.1 gm cm^{-3}.

The effective densities determined for the different wavelengths agree quite well in the equatorial and northern mid-latitudes and begin to diverge in the further north. In addition no estimates are made for latitudes south of 15°S. This is because the results of the fitting routine became unreliable south of this latitude. This is probably a manifestation of some difference between the model's thermal parameters and the actual sub-surface in the southern hemisphere. This is also apparent in the brightness temperature versus latitude plots. It can be seen in Figure 4.2 that south of this latitude the 2cm data become colder than any of the models and it may also be true for the 6cm data. Below 35° S, surface roughness takes on a more important role and the data and the models do not agree as well as at smaller emission angles. This region is also seen to be anomalous in the South data set. This region will be discussed in more detail in Chapter 5.

Because of this anomalous change in brightness temperature, the last couple of estimates of dielectric constant and density are in question. Although they are included with the rest of the estimates in the plots for reference purposes, we do not believe the last estimate of the dielectric constant is a true reflection of the effective dielectric constant of the sub-surface. Rather we believe the explanation for the unusual

behavior of the brightness temperature in this region lies in the thermal behavior of the sub-surface.

The longitudinally averaged dielectric constants can also be used to calculate a whole-disk dielectric constant. For the 6cm data this number is 2.8±0.5, and for the 2cm data this number is 3.1±0.5. At 6cm the whole-disk dielectric constant calculated from the two different methods are in relatively good agreement (2.7 vs. 2.8). However, at 2cm, the dielectric constant measured from the degree of polarization fitting to the visibilities is smaller than that deduced from the thermal equilibrium models (2.3 vs 3.1). It is possible that the estimate of the map fitted whole-disk dielectric constant is too high due to calibration error, since, as stated earlier, a 3K difference between the model and the data is equivalent to a 0.3 change in the effective dielectric constant. Therefore, it wouldn't take much difference in the temperature to cause this discrepancy. However, the agreement between the two methods, one not dependent upon the calibration, plus the North Polar Cold Region results, reassure us that our calibration is good to within several percent. It is more likely that this discrepancy is due to the fact that the dielectric constant estimated from the whole-disk polarization measurement is more sensitive to surface depolarization, particularly at the shorter wavelength. This is because a rough surface depolarizes emission more than it changes the amount of emission. This would then appear as a lower effective dielectric constant than the longitudinally averaged dielectric constants. If the surface of the planet were partly covered with rocks on the order of the wavelength, the whole-disk, polarization-derived dielectric constant would be lower than the average map fitted dielectric constants. The surface depolarization could also affect the 6cm whole-disk measurement. However, it would be affected to a lesser degree, depending on the scale of the roughness, than the shorter wavelength (c.f., Muhleman *et al.*, 1976).

CHAPTER 5
SOUTH DATA SET: RESULTS AND DISCUSSION

As with the North data set, the results for the South data set will be divided into three sections. The first will concern itself with the whole-disk results. That is, those results obtained by directly fitting the visibilities to a simple uniformly bright disk model. The second section will discuss the South Polar Cold Region brightness temperatures and sizes. Finally, the third section will present the results of the thermal model fitting of the mapped data.

5.1 Whole-Disk Results

The South data set whole-disk dielectric constants and brightness temperatures are listed in Table 5.1. This table differs from the table showing the North data because of the problem with calibration mentioned in Chapter 2. So included in Table 5.1 are the corrected whole-disk brightness temperatures obtained by following the procedure outlined in Chapter 2. All results in this chapter are presented with the following caveat: There is an uncertainty in the base brightness temperatures of about 6% at 6cm and 9% at 2cm. Now it may be possible that the brightness temperatures are what we measured, but it is extremely unlikely. Unfortunately, the observations were taken far enough into the southern summer that the South Polar Cap had receded beyond our ability to get an accurate brightness temperature. This precludes using the relatively well known kinetic temperature of CO_2 frost to re-calibrate the brightness temperatures. Instead, re-calibration was performed using the whole-disk dielectric constants and the thermal model described in Chapter 3. This procedure was described in Chapter 2. These 're-calibrated' results can be compared

TABLE 5.1

Southern Data Set Results		
Wavelength	2cm	6cm
Whole Disk Dielectric Constant	2.02 ± 0.03	2.47 ± 0.06
Whole Disk Sub-surface Density (g cm^{-3})[a]	$1.02 \pm .06 \pm .16$	$1.31 \pm .10 \pm .16$
Whole Disk Brightness Temperature[b]	$220.9\text{K} \pm 1.0$	$183.9\text{K} \pm 0.6$
Re-calibrated Brightness Temperature[b]	$202.2\text{K} \pm 1.0$	$195.4\text{K} \pm 0.6$
Re-calibration Ratio, South	1.093	0.941
Re-calibration Ratio, North[c]	1.015	1.031
Normalized Brightness Temperature[d]	$198.0\text{K} \pm 1.0$	$192.1\text{K} \pm 0.6$
2.8cm Bright. Temp., Doherty *et al.* (1979)[d]	$195.2\text{K} \pm 2.7$[e]	—
6cm Bright. Temp., Epstein (1971)[d]	—	$196\text{K} \pm 27$
South Polar Cold Region Bright. Temp.	$182.9\text{K} \pm 2.0$	$148.1\text{K} \pm 2.0$
South Polar Cold Region Extent	$52.7° \pm 0.4$	$62.2° \pm 0.7$
South Polar Cap Extent, James *et al.* (1982)	$\sim 86°$	
South Polar Cap Extent, Fischbacher *et al.* (1969)	$> 80°$	

[a]The first error is the formal least squares error, and the second error is due to the scatter in dielectric constants for powders of varying origins. (c.f. Campbell and Ulrichs, 1969)

[b]See text for explanation of the re-calibration procedure.

[c]The re-calibration ratio for the North data set is given for comparison purposes only. The North data set was not re-calibrated.

[d]These temperatures have been normalized to a uniform solar distance of 1.524AU using an $R^{0.25}$ power law for comparison purposes.

[e]These measurements were published as functions of longitude and the error shown here is actually the variation over longitude.

with the brightness temperature as measured by other observers and listed in Table 5.1. Figures 5.1 and 5.2 show the both the original data and the re-normalized data. Both were averaged in the same way to obtain these plots.

Recall that, although the whole-disk brightness temperatures were obtained from the re-calibrated data, the whole-disk dielectric constants were not. This is because the polarized flux is divided by the unpolarized flux to obtain the whole-disk dielectric constant. This normalization means that the results of this fitting are independent of the calibration. Therefore, we have good reason to believe the accuracy of these results. Of course, these are only effective dielectric constants because no surface

roughness has been taken into account. This fact is not worrisome in the re-calibration of the whole-disk brightness temperatures because the thermal-radiative model also does not take into account the surface roughness and uses only effective dielectric constants. In addition, the decrease in surface radio emissivity at near normal incidence caused by surface roughness is nearly balanced out by the increased emissivity near the limb for whole-disk measurements (Muhleman, personal communication).

Comparing the whole-disk effective dielectric constants from the South data set to those derived from the North data set shows that the dielectric constant at each wavelength is about 0.3 less than its counterpart in the North. The lower effective whole-disk dielectric constants deduced from the South data set is consistent with the north-south asymmetry seen in the thermal inertia and albedo maps of Palluconi and Keiffer (1981). This asymmetry can also be seen in the geologic maps of Scott and Carr (1976). The lower dielectric constant at 2cm seems to indicate a surface layer of dust or possibly, and more likely, a large degree of roughness on the order of 2cm. The 6cm dielectric constant also being lower indicates that it is probably surface roughness which is lowering the dielectric constants. This roughness or lack of a layer of dust could also be the reason the northern hemisphere has, on average, a higher albedo than the southern hemisphere.

5.2 South Polar Cold Region

The results of the South Polar Cold Region fitting are listed along with the whole-disk results in Table 5.1. Note the discrepancy between the latitude of the edge of the South Polar Cold Region and the South Polar Cap as observed by others. From inspection of photographs taken by the Viking orbiter (c.f., James *et al.*, 1979), and from ground-based observations, (c.f., James and Lumme, 1982), it is clear that by

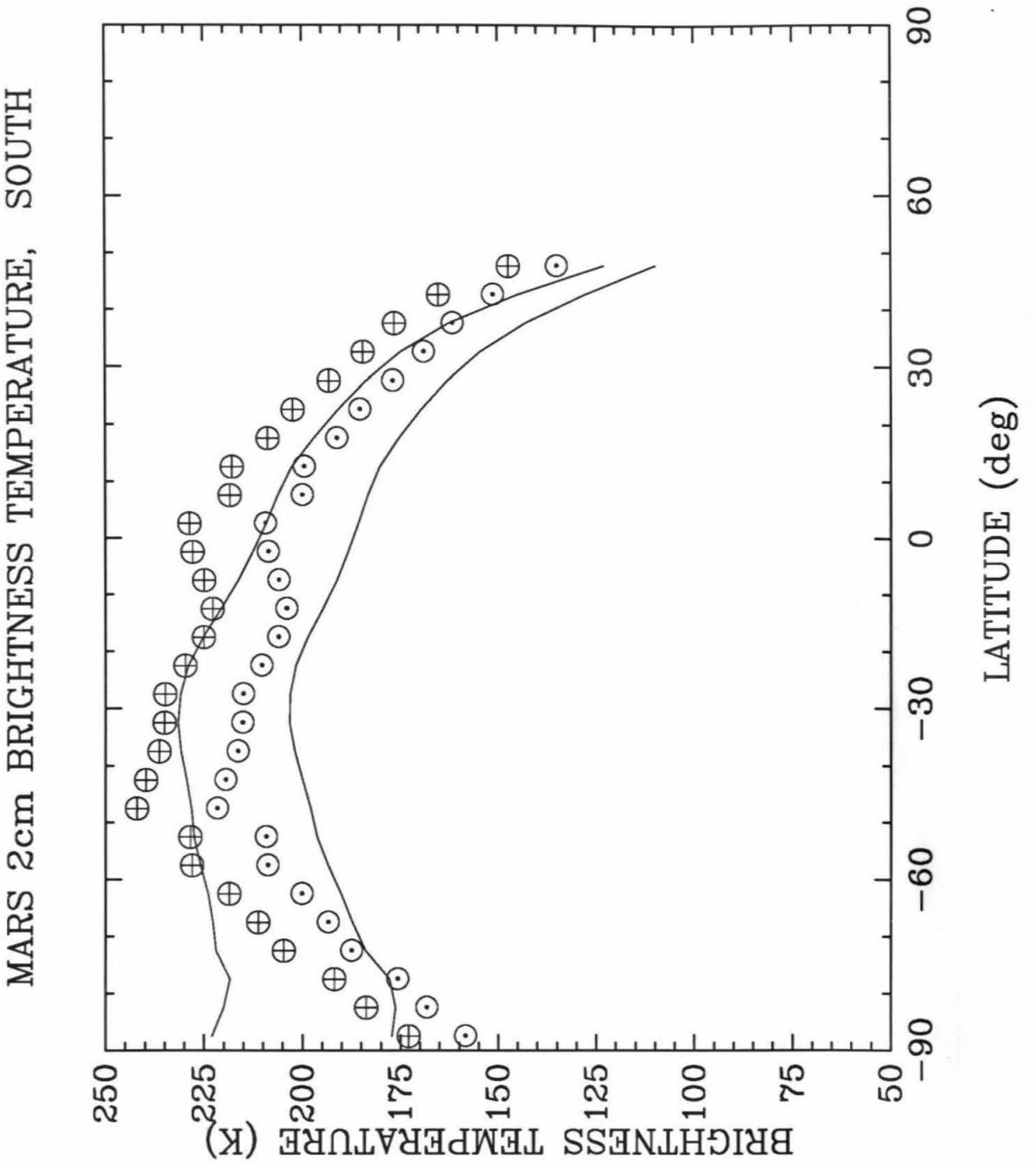

FIGURE 5.1: Shown are the longitudinally averaged 2cm brightness temperatures (circled crosses) and the re-normalized brightness temperatures (circle dots). The upper and lower curves have dielectric constants of 1.4 and 3.8, respectively. The radio absorption lengths of the upper and lower curves are 5.0 and 20.0 wavelengths, respectively. The sub-earth latitude was 26.2°S

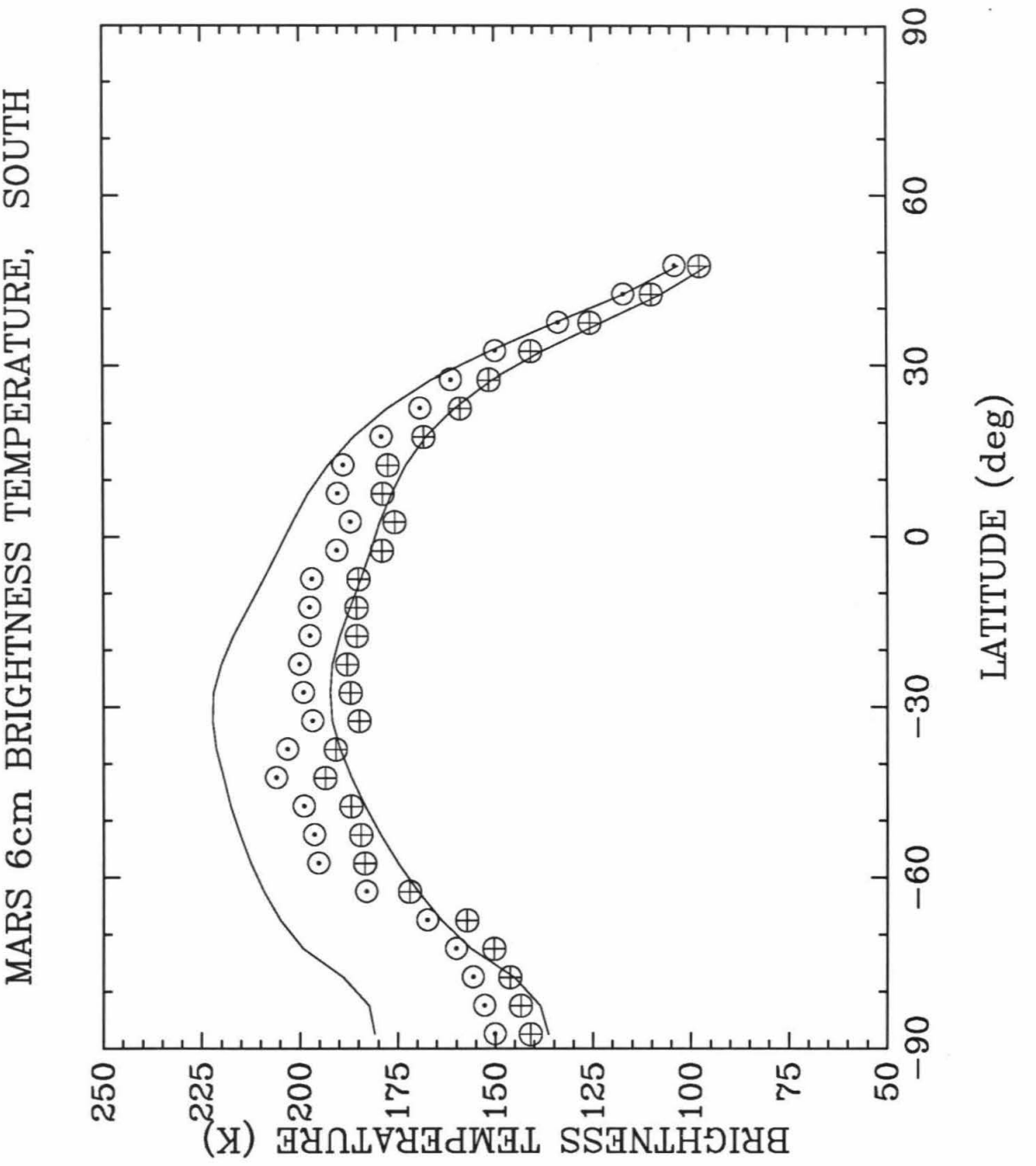

FIGURE 5.2: Shown are the longitudinally averaged 6cm brightness temperatures (circled crosses) and the re-normalized brightness temperatures (circle dots). The upper and lower curves have dielectric constants of 1.4 and 3.8, respectively. The radio absorption lengths of the upper and lower curves are 5.0 and 20.0 wavelengths, respectively. The sub-earth latitude was 26.2°S

the season during which we observed, $L_S = 300°$, the South Polar Cap is reduced to nearly its residual configuration. If, during the season we observed, the South Polar Cap is indeed as small and as offset from the geometric pole as the photographs indicate it became during the same season in previous years, then the corresponding South Polar Cold Region would not be resolvable in the 6cm data and barely so in the 2cm data. This is because the cap would be the same size as the bins. In addition, if it is offset, it would tend to get lost in the smearing of the data due to rotation of the planet.

There is, however, a definite region which does appear colder than the latitudes more to the north of it. The signature of this region is the sudden drop in brightness temperature, for both wavelengths, at a latitude of about 60°S. This region, which can be seen in Figures 5.1 and 5.2, is the area that was fit by the South Polar Cold Region fitting program. Recall the very simple model used to fit the South Polar Cold Region brightness temperature and extent. It is just a disk with two regions of different fluxes convolved with a gaussian similar in size and shape to the clean beam. This region of lower brightness temperature is the reason that the fitted South Polar Cold Region is much larger than the visual extent of the South Polar Cap, as determined by other observers.

Possible explanations for the existence of this region include a smaller than expected thermal inertia, possible sub-surface volatiles, including water, or scattered 'islands' of CO_2 frost. Since the thermal inertias of Palluconi and Keiffer (1981) only extend as far south as 60°, the physics of this region is not constrained well enough to speculate about which of these, if any, is correct. Although the 6cm brightness temperature of this cold region is relatively consistent with there being a covering of frost over large tracts of this area, the 2cm brightness temperature is such that this zone cannot be uniformly covered by CO_2 frost. It can, at best, have only a

very limited covering. It is possible that, because of the very roughness that causes the dielectric constants to be low, there are 'islands' of CO_2 that remain longer than would be expected. This could be due to shadowing by the roughness or even possibly sub-surface pockets of CO_2. Because of the rotational smearing of the data, this would probably look very similar to the data. However, the photographs of this region at this season do not indicate that such pockets of frost exist, at least not on a scale large enough to be easily discernible. This leaves the brightness temperature of the province south of 60° a mystery, at least for now.

Since the thermal model predicts that the seasonal CO_2 cap will all but have disappeared by this season, there is some discrepancy between this present discourse and the work of others. The article by Paige and Ingersoll (1985), for example, indicates that their South Polar Study Region is covered by CO_2 frost all year long. However, this region is very small and is offset from the geometric pole. It is not possible with the current radio data set to resolve such a region. It would be lost in both the binning and the rotational smearing. The discrepancy between the thermal models described in this work and those used by Paige and Ingersoll is in the conduction of heat from the sub-surface to the surface. Our current thermal model starts with no frost and goes for 4 model years letting the frost accumulate and sublimate. Paige and Ingersoll assume the residual cap to be CO_2 frost, because from the observations it appears to be. Therefore, heat conduction from the sub-surface would be minimal. It is obvious that if the frost ever does disappear completely, the surface temperature would rise steeply and the sub-surface would begin to accumulate heat making condensation begin at a later date and so less CO_2 frost would be present throughout the winter.

Therefore, the discrepancy between this present work and the work of Paige and Ingersoll is actually minimal for the heat balance, but is quite great on the question of

the permanence of CO_2 frost at the South Polar Cap. In addition, the thermal model used for both this chapter and the previous chapter does not include topography. The South Polar Cap is at a different distance from the geoid than implicitly assumed in the thermal model. This would influence the sublimation temperature of the CO_2 frost. Since the current thermal model does not include H_2O ice accumulation nor sublimation, this is possibly another source of difference between the thermal model and the visual data. It may be possible that the same physical causes can explain both the observed extent of the South Polar Cold Region and the fact that there exists a residual CO_2 frost cap. This would be a very interesting avenue of research to pursue.

5.3 Latitudinally Binned Results

As can be seen from Table 2.2, the region of longitudes passing through the sub-earth point during the South observing run have very little overlap with the longitudes that passed through the sub-earth point during the North observing run. This means that the North results for a given latitude bin cannot be used as a check on the re-calibration procedure. However, the regions observed during the South run are more compatible with the regions observed by radar, because most of these observations are made with the sub-earth point in the southern hemisphere. The observations made by Pettengill *et al.* (1973) covered a region between 70°W and 110°W and latitudes between 14°S and 22°S. This region passed through the sub-earth point during the beginning of the South observing run. For a wavelength of 3.8cm they measured a dielectric constant that varied from 1.7 to 5. The best fit results from the South data set yield dielectric constants of about 2.7 at 2cm and 2.5 at 6cm.

The work of Harmon and Ostro (1981) also contains calculations of the reflectivity

in one region that overlaps the region we observed. Both their region at 55.7°W, 25°N and their region at 143.1°W, 25°N were measured to have a reflectivity of 0.11, which translates to a dielectric constant of about 3.75. This is a higher dielectric constant than we measured for a similar region on the planet. The values at these same latitudes were estimated to be 2.1 at 2cm and 2.45 at 6cm. This latitude is also where surface roughness effects start to play an important role and therefore, is at the limit at which dielectric constants were estimated.

Figures 5.1 and 5.2 show the longitudinally average brightness temperatures for 2cm and 6cm, respectively. As with Figures 4.2 and 4.3, Figures 5.1 and 5.2 also show the extremes of the models used in fitting the dielectric constant and radio absorption length. In addition, Figures 5.1 and 5.2 also show the longitudinal average of the data before the re-normalization. The brightness temperatures were averaged in the same manner as for the North data set. The inability of the models to fit the data north of about 30°N, which is an emission angle of about 70°, is due mostly to roughness effects. As with the North data set, there is a region in the south temperate latitudes in which the brightness temperatures appear to be cooler than a model which would be considered a best fit at all latitudes. The difference between the South and North data sets is that the onset of this 'cool' region begins at about 15°S for the North data set, whereas for the South data set the region appears to begin nearer the equator. Since the data are smeared in longitude by the rotation of the planet, the region that is included in the anomalous area is rather large. Since it is seen in both data sets it nearly circumscribes the globe. The surface geology has been mapped by Scott and Carr (1978). The major geologic units in the anomalous region are: (using the nomenclature of Scott and Carr) Nplc, Cratered Plateau Material, and Nhc, Hilly and Cratered Material. Both are highly cratered rough terrain, with the major difference between the two units being that the intercrater regions in the Nplc unit are smooth

on a length scale larger than about 30m and the intercrater regions in the Nhc unit are rough on this scale. From the albedo maps of Palluconi and Keiffer (1981) it can also be seen that this is a region of relatively low albedo.

Since the North data set was analyzed first, and it was late fall in the southern hemisphere for that data set, the anomalous brightness temperatures indicated that the warm summer seasonal wave had penetrated the sub-surface farther or with less attenuation than the models predicted. This could happen if the sub-surface thermal inertia were larger than accepted. The idea that a duricrust, postulated elsewhere, (c.f. Jakosky and Christensen, 1986) may be thicker in this region than in the more northerly regions observed was discussed in a recently published paper, Rudy *et al.* (1987). This thicker, or more tightly bound, duricrust would have a larger thermal inertia than just the unbound regolith of which it is made.

This idea was explored by running the thermal model for a specific latitude, 22°S, using variations of the thermal inertia. In order to affect the surface temperature to as small a degree as possible, the thermal inertia was varied only below the diurnal skin depth. Two thermal inertia cases were tested. Both were two layer models with the upper layer being held at a thermal inertia of 6.5 and only the lower layer was varied. The first case consisted of a 4cm region with a thermal inertia of 6.5 (the planetary average used by Keiffer *et al.*, 1977) overlying a region with a thermal inertia of 4.0. This second region extended all the way down to the bottom layer. The second case consisted of the same near-surface region, but the lower layer had a thermal inertia of 10.0. Recalling that the Martian season was $L_S = 60°$, it can be seen from Figure 5.3 and 5.4 that increasing the sub-surface thermal inertia causes the brightness temperature at both wavelengths to be cooler. Therefore, this change in thermal inertia can explain the cooler temperatures in the anomalous region for the North data set. In addition, changing the sub-surface thermal inertia has very

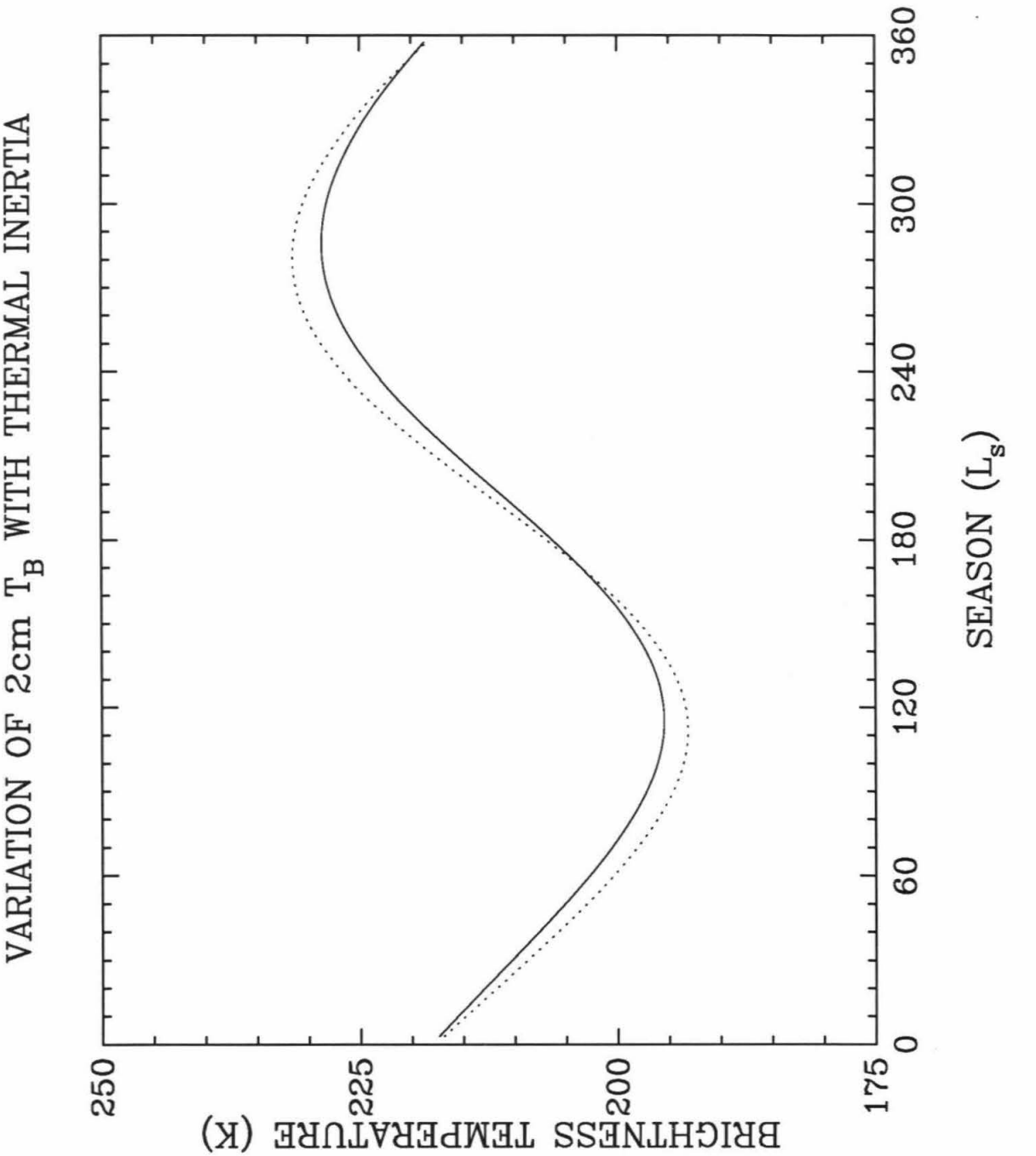

FIGURE 5.3: The solid line is the seasonal variation of the average diurnal 2cm brightness temperature at 22°S for a sub-surface consisting of a layer with a thermal inertia of 4.0 underlying a 4cm region with a thermal inertia of 6.5. The dotted line is the same calculation, but with a thermal inertia of 10.0 underlying the 4cm of the sub-surface with a thermal inertia of 6.5.

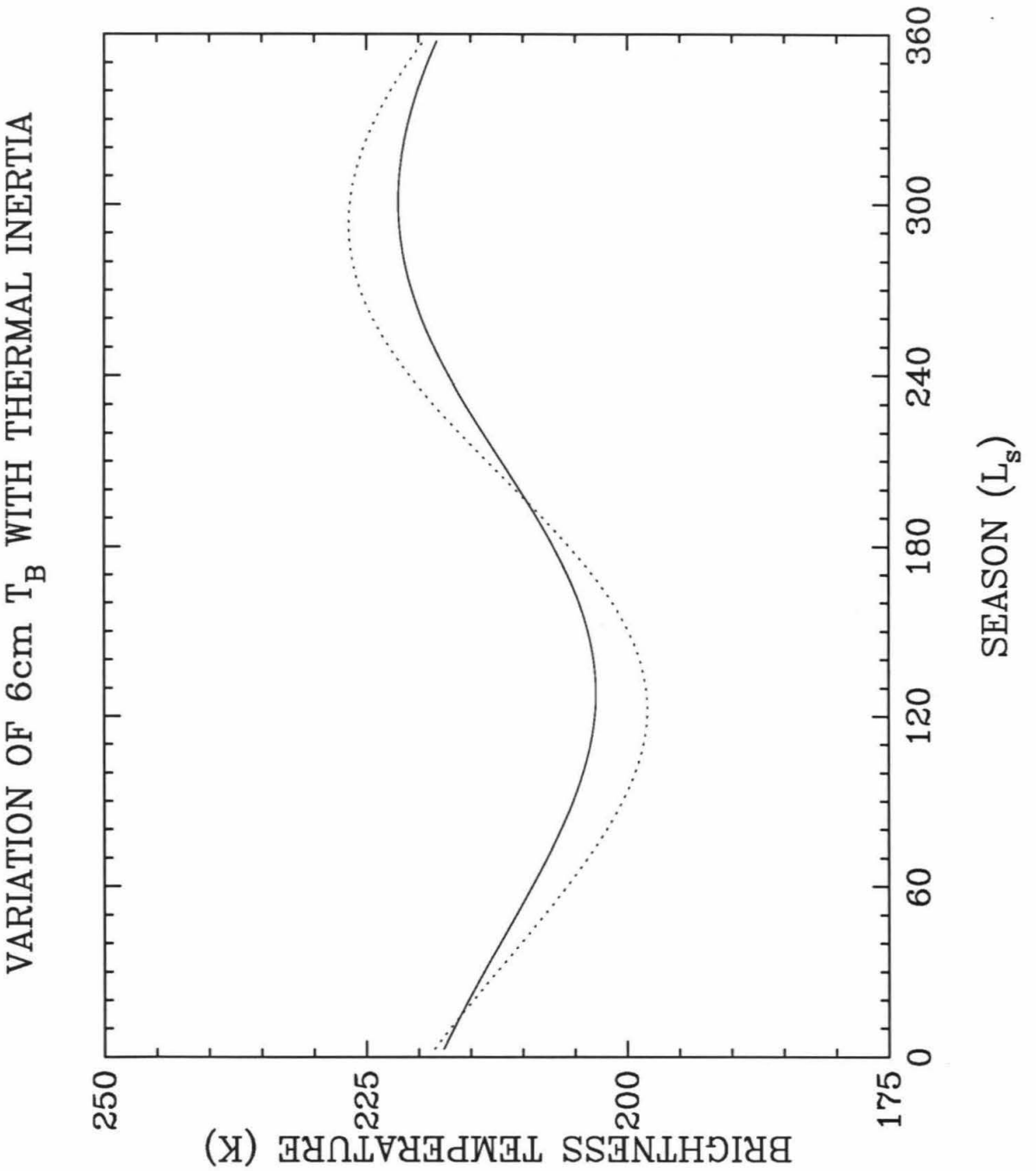

FIGURE 5.4: The solid line is the seasonal variation of the average diurnal 6cm brightness temperature at 22°S for a sub-surface consisting of a layer with a thermal inertia of 4.0 underlying a 4cm region with a thermal inertia of 6.5. The dotted line is the same calculation, but with a thermal inertia of 10.0 underlying the 4cm of the sub-surface with a thermal inertia of 6.5.

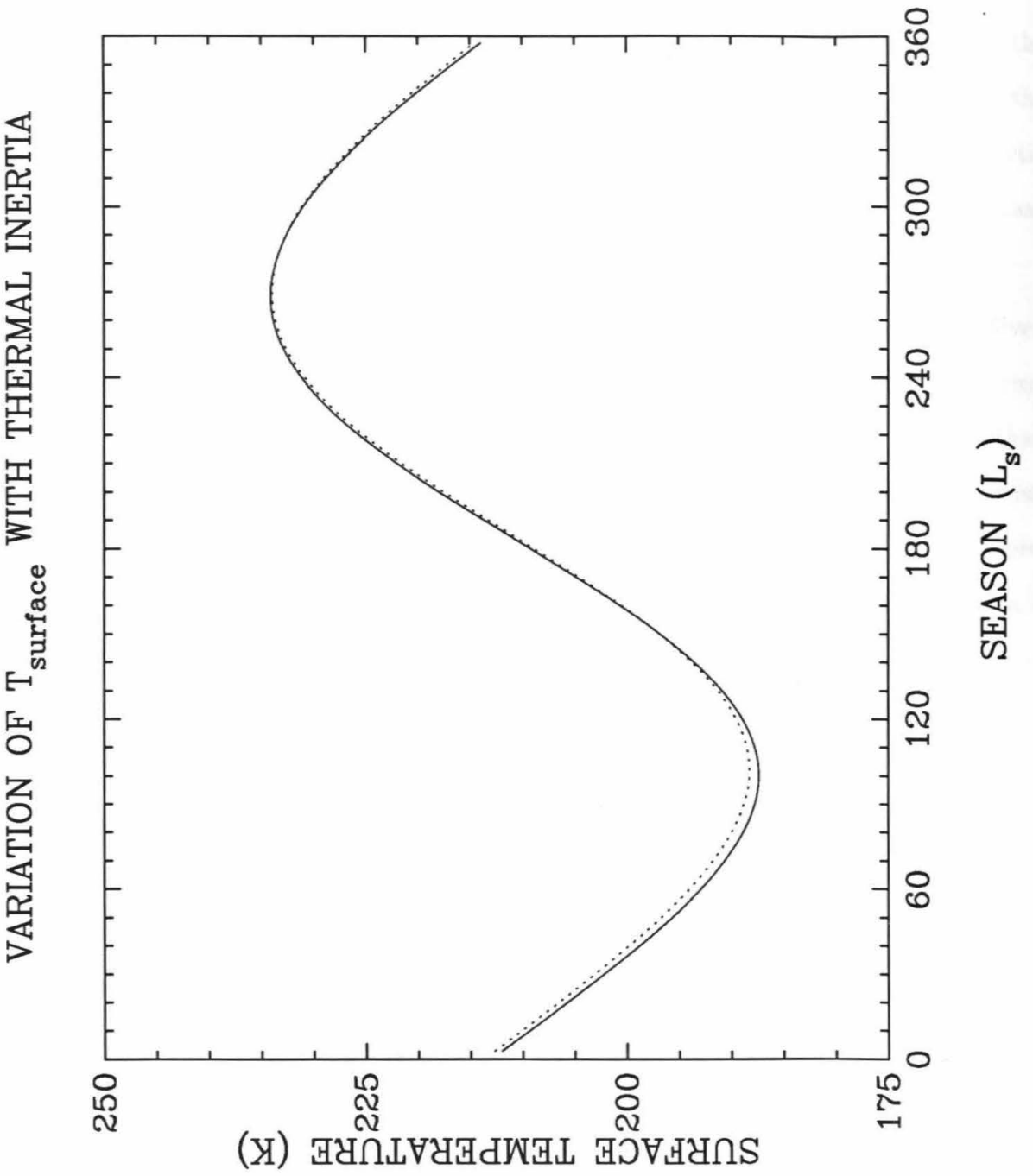

FIGURE 5.5: The solid line is the seasonal variation of the average diurnal surface temperature at 22°S for a sub-surface consisting of a layer with a thermal inertia of 4.0 underlying a 4cm region with a thermal inertia of 6.5. The dotted line is the same calculation, but with a thermal inertia of 10.0 underlying the 4cm of the sub-surface with a thermal inertia of 6.5.

little effect on the surface temperatures. This can be seen in Figure 5.5. If the variation in thermal inertia occurred at an even greater depth, the effect on the surface temperature would be even less. Of course, if the variation in thermal inertia occurred at a greater depth it would also decrease the difference between the case with a second layer and the case which is homogeneous.

Unfortunately, the South data set is also anomalously cool in this region. Given that the Martian season was $L_S = 305°$ during the time of the South observing run, Figures 5.3 and 5.4 predict a warmer brightness temperature at both wavelengths than if the surface had a homogeneous thermal inertia. Therefore, a variation in thermal inertia with depth alone will not explain both regions. The South data set, therefore, eliminates the possibility that the discrepancy between the models and the data is due solely to a change in the thermal conductivity with depth. The work by Pollack *et al.* (1979) shows that the average surface temperature during dust storms probably is not much different tha the average surface temperature before the dust storm. So invoking dust storms as a method of explaining the temperature anomaly is not feasible. What is needed is a mechanism that can cool the sub-surface temperature all year, or equivalently, cool the surface temperature for a good fraction of the year.

Since the band of low brightness temperature shows up in the Palluconi and Keiffer albedo maps as a region of low albedo, the question arises: What if this region's albedo is not that low? It may be possible that a global dust storm deposited a layer of dust over this band and increased its albedo for the year during which our observations were taken. Christensen (1986) did a study of the albedo variations in several regions on the Martian surface and how long these variations lasted. As a test of this hypothesis, the thermal model was run with a homogeneous thermal inertia, but with two different albedos. The two cases had albedos of 0.15 and 0.35. These were chosen because the first one is a reasonable estimate of the albedo near 22°S

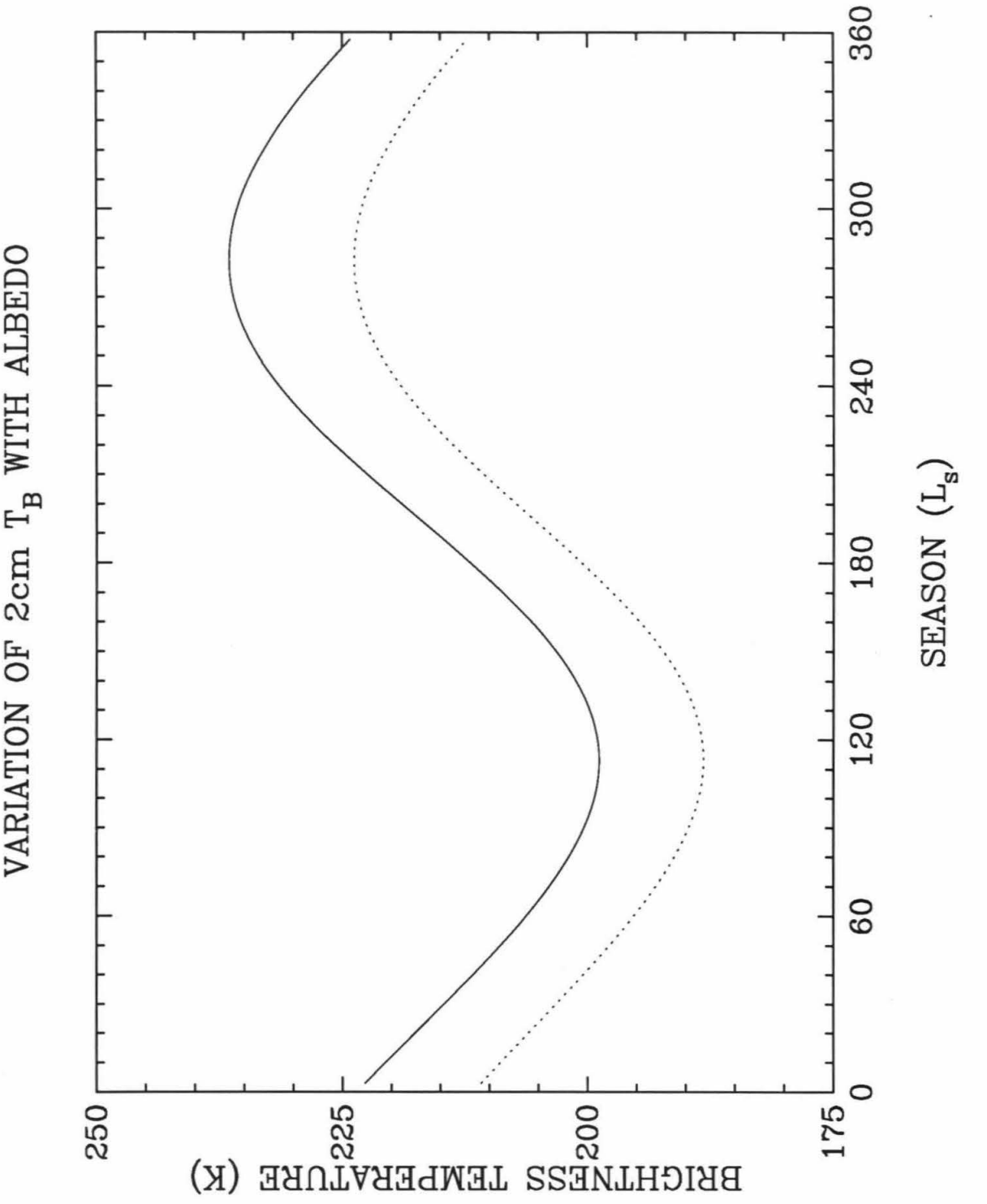

FIGURE 5.6: The solid line is the seasonal variation of the average diurnal 2cm brightness temperature at 22°S for a sub-surface with a surface albedo of 0.15. The dotted line is the same calculation, but with a an albedo 0.35.

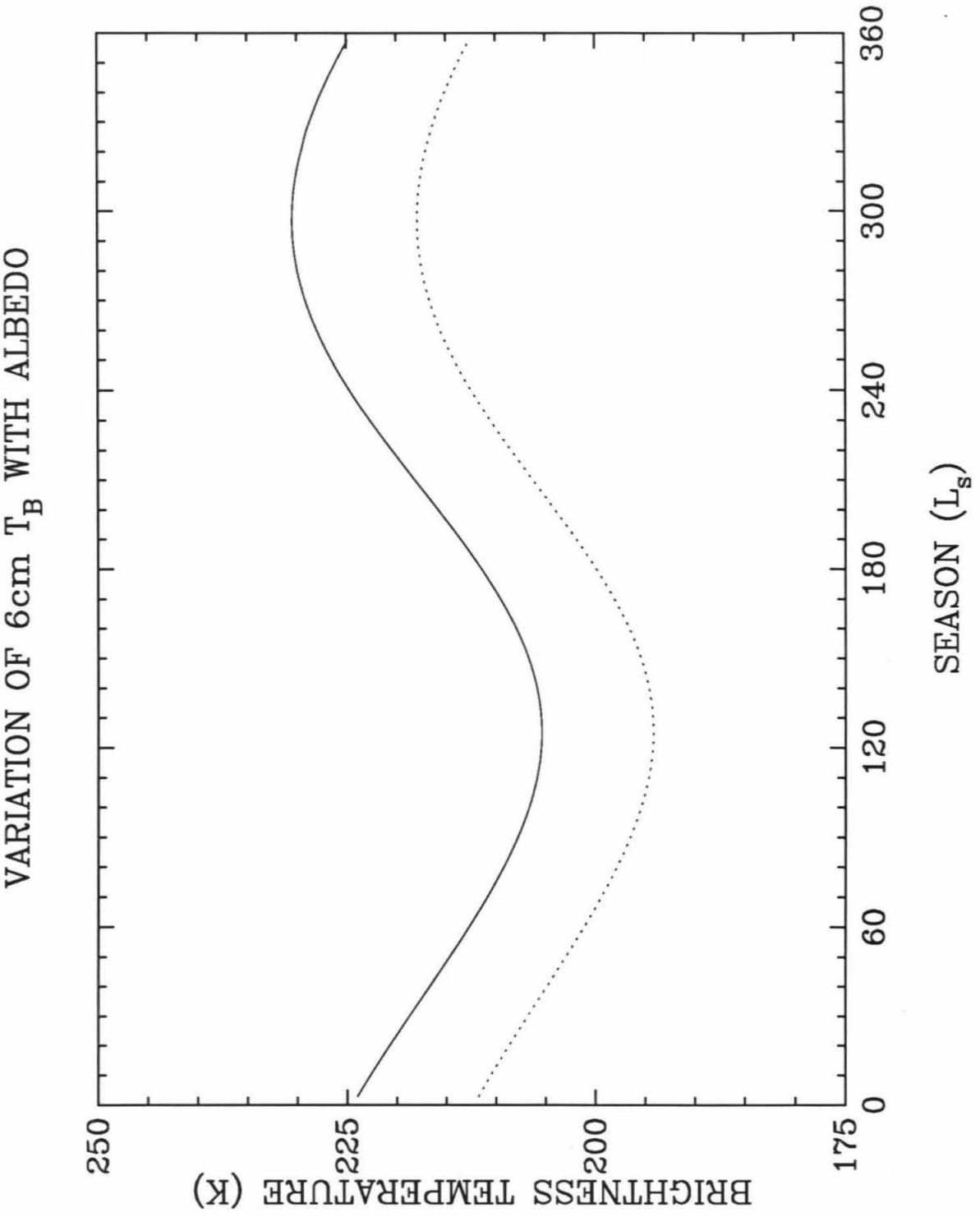

FIGURE 5.7: The solid line is the seasonal variation of the average diurnal 6cm brightness temperature at 22°S for a sub-surface with a surface albedo of 0.15. The dotted line is the same calculation, but with a an albedo 0.35.

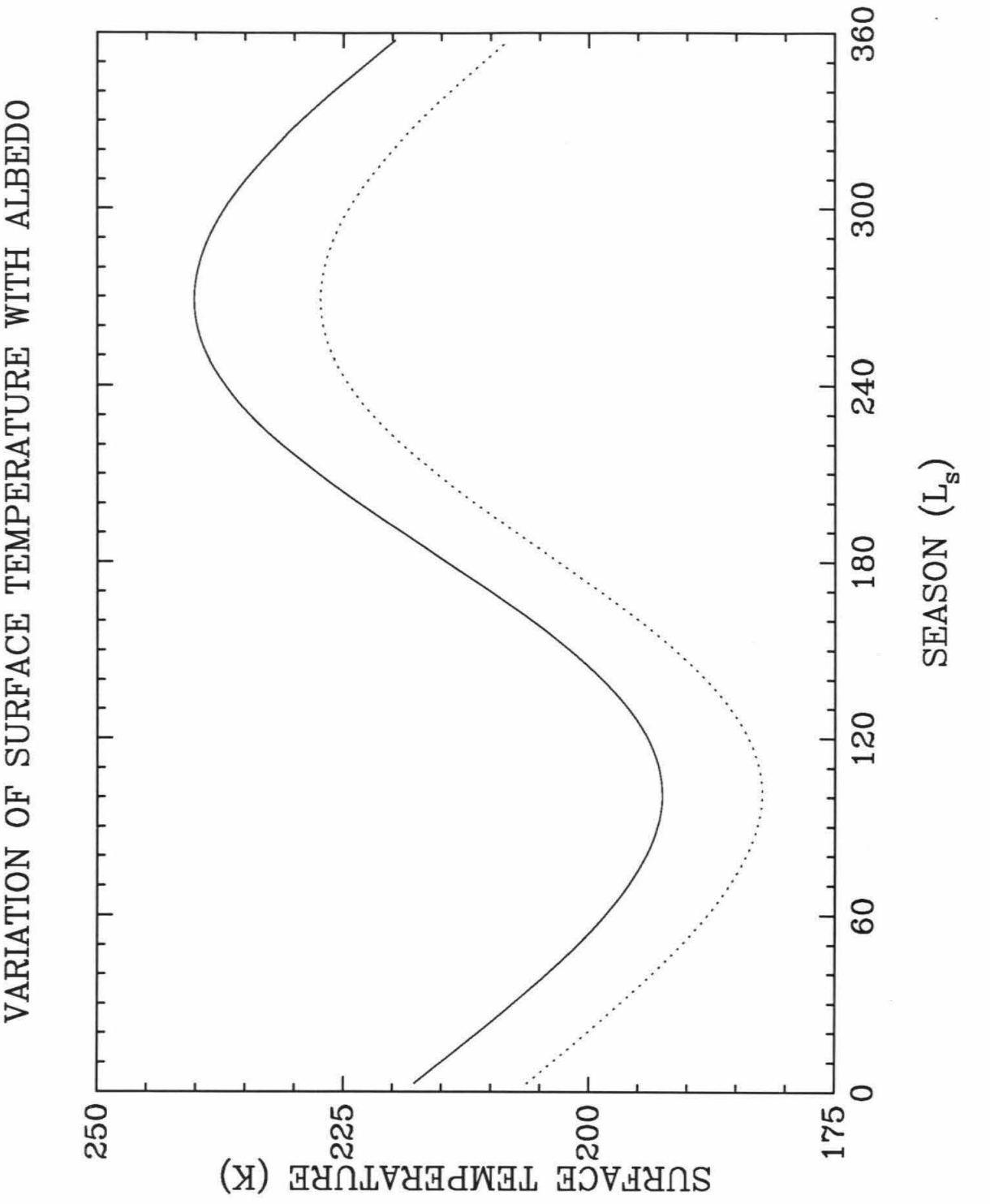

FIGURE 5.8: The solid line is the seasonal variation of the average diurnal surface temperature at 22°S for a sub-surface with a surface albedo of 0.15. The dotted line is the same calculation, but with a an albedo 0.35.

where the model calculations were performed. The second was chosen because its a reasonable value for an increase in this region due to a covering of dust. For the sake of illustration, the albedo was not varied during the thermal model calculations, rather, the albedo was set at a certain value and held there through four Martian seasons. Because of this, the brightness temperatures for the case with an albedo of 0.35 are actually lower than they would be if the surface were brighter only part of the year.

As can be seen in Figures 5.6 and 5.7, the brightness temperatures at both wavelengths are very strongly affected by a change in surface albedo. And the change is in the proper direction to explain the anomalous temperatures for both seasons. Since only about 8K of variation is needed to cause the region to behave in the manner seen in the data, and since the changes in Figures 5.6,7,8 are all on the order of 12K or since, this magnitude of variation is probably all that is required to explain the discrepancy. Of course, the model should be run with a time-variable albedo to see what percentage of a year must be spent in each albedo state to achieve the requisite temperature change. Also, the albedo, if it changes, almost certainly does not change from a high albedo condition to a low albedo condition discretely (although it most probably does change from low to high in a discrete manner). Both these questions need to be examined.

Since a change in albedo also changes the surface temperature, as can be seen in Figure 5.8, this explanation requires that the albedo, as mapped by Viking, be a function of time. If this is true for one region, it may also be true for other regions. It may be that certain, rough, surface features hold onto the dust deposited during a storm much longer than other regions and therefore, are more susceptible to cooler sub-surface temperatures than their less rough counterparts. Christensen (1986) studied several regions and found that certain regions of the surface had albedos which

did not return rapidly to their pre-dust storm values, but rather did so only slowly. These regions remained brighter for several months after the dust storms and only slowly returned to their pre-dust storm albedo values. A laboratory study by Wells *et al.* (1984) showed that minute amounts of dust can radically alter the surface photometric and spectral characteristics. For example, they found that the average reflectance at 0.56 microns of their average dark area increased by 70% after deposition of just 1.5×10^{-4} gm cm^{-2} of dust.

Figures 5.9 and 5.10 show the effective dielectric constant as a function of latitude for each wavelength for the Southern data set. As with the Northern data set, the error bars are formal errors only. Because of the re-calibration procedure the absolute errors are about 6% at 6cm and approximately 9% at 2cm. The latitude dependence of the dielectric constant at one wavelength is not correlated to that of the dielectric constant at the other wavelength. This lack of correlation is not like the case of the North data set, where a minor amount of correlation was noticed. This is most likely due the problems the fitting routine had for the anomalous region. The longitudinally averaged radio absorption length as a function of latitude is shown in Figure 5.11. Unlike Figure 4.4, Figure 5.11 shows large variations in the radio absorption length. An average over longitude of the radio absorption length would yield an average of about 15, the same as for the North data set. This translates to a region of sampling down to about 30cm for a wavelength of 2cm and about 90cm for a wavelength of 6cm. However the scatter among the South data is much larger than for the North data. As can be seen in Figure 5.11, the radio absorption length for that part of the anomalous region between 10°S and 25°S is higher than this average and the region south of the anomalous region is slightly lower than 15λ. North of the equator the estimated radio absorption lengths all congregated right around 15λ which is approximately what was determined for the North data set.

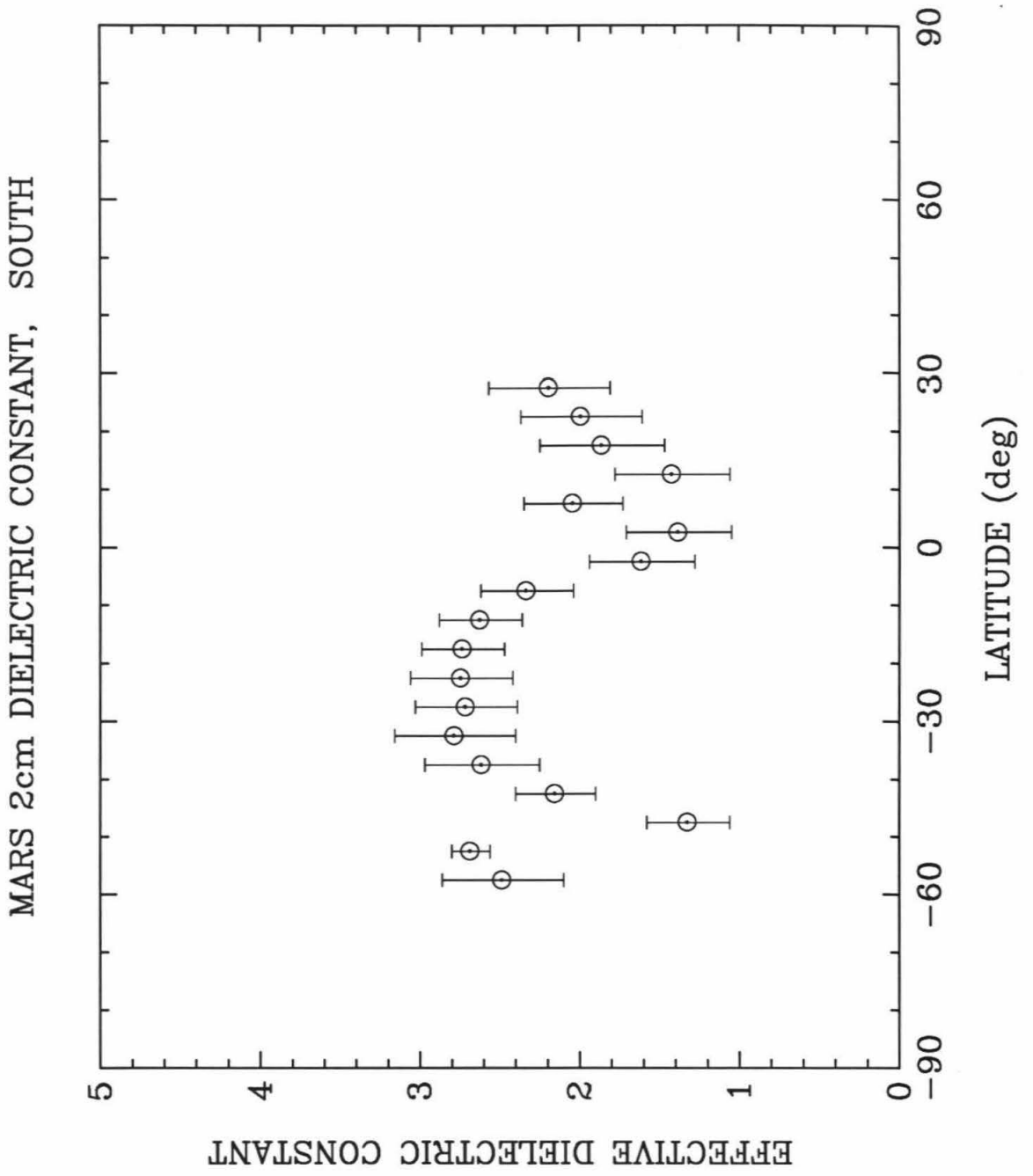

FIGURE 5.9: The data points are the longitudinally averaged 2cm effective dielectric constants as a function of latitude. The error bars shown are formal errors only and do not take into account systematic errors such as calibration errors.

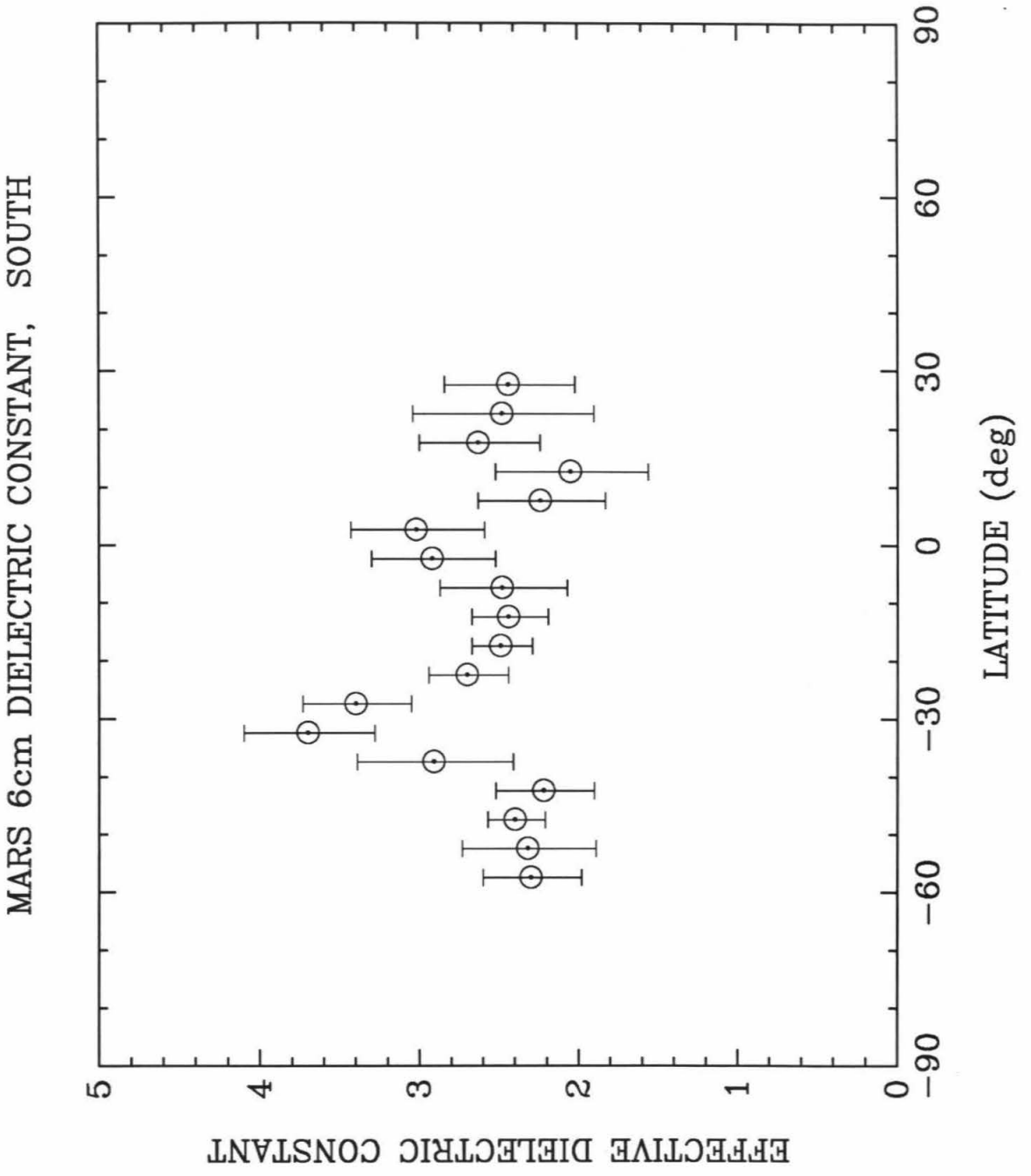

FIGURE 5.10: The data points are the longitudinally averaged 6cm effective dielectric constants as a function of latitude. The error bars shown are formal errors only and do not take into account systematic errors such as calibration errors.

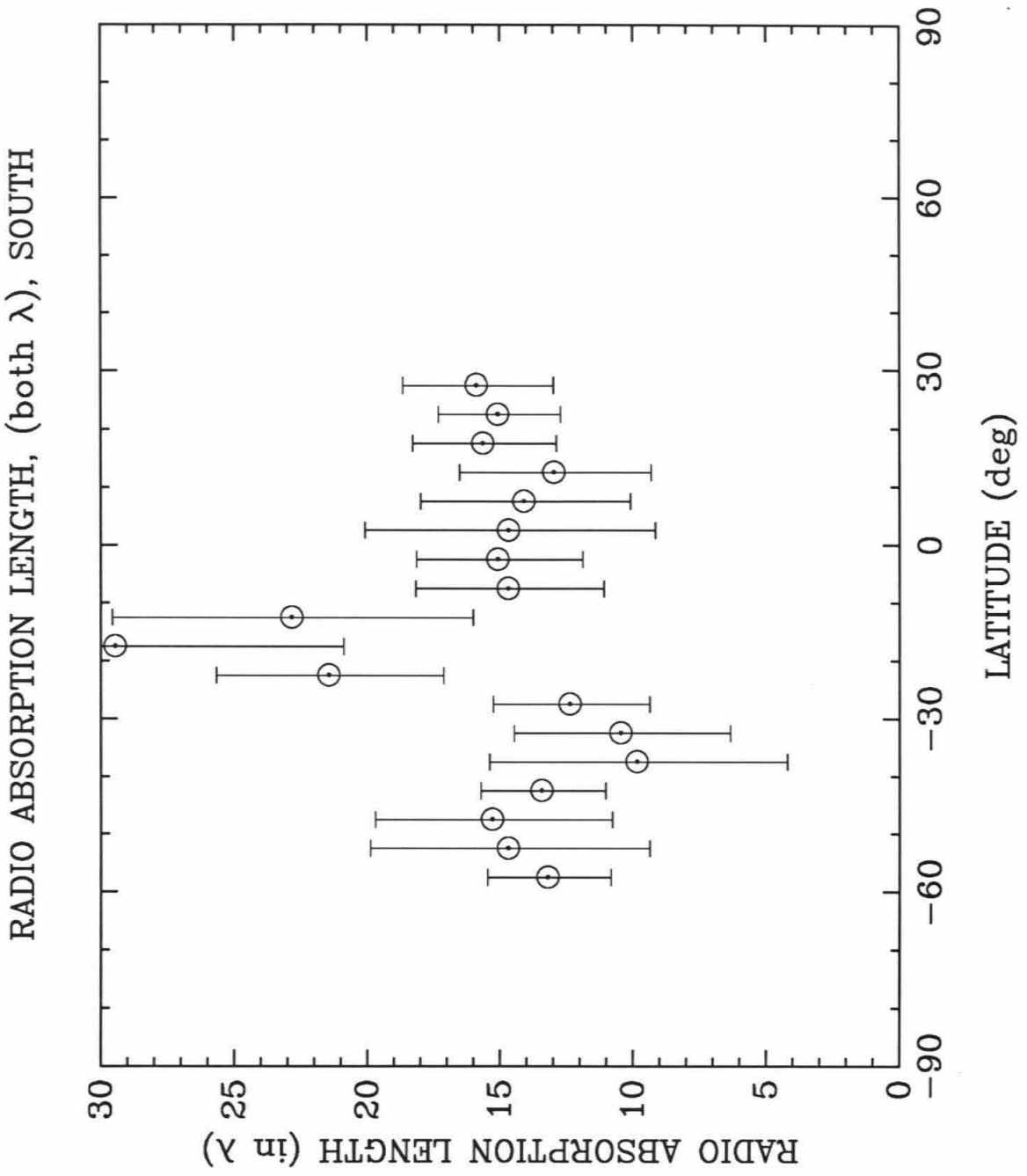

FIGURE 5.11: This figure shows the radio absorption length as a function of latitude. The error bars shown are formal errors only and do not take into account systematic errors such as calibration errors.

Since the sub-earth longitudes observed during the North observing run are not the same as those for the South observing run, a direct comparison of these two data bases is not strictly possible. Since one does not expect there to be a great difference between the east and west hemispheres, a small diversion to compare and contrast the latitudes that overlap the two data bases will be illuminating in spite of this fact. The comparison of the dielectric constants in the region between 30°N and 20°S shows that, at both wavelengths, the North data set derived dielectric constants are larger than the corresponding dielectric constants derived from the South data set. However, both have the same general trend, with a dip at about 15°N. The gap between the 2cm dielectric constants for the two data sets is larger than it is for the 6cm dielectric constants. This discrepancy could be explained by the fact that the two data bases have completely different sub-earth longitudes. Since the error bars for both data sets at both wavelengths are on the order of 0.6, this difference would not be exceptional. As a matter of fact, considering the size of the error bars, the 6cm dielectric constants agree quite well.

The large difference at 2cm could also be caused by a calibration error in the North data set; as was stated in Chapter 2, 2cm data are more sensitive to calibration errors than 6cm data. A third possible explanation is a difference in surface roughness between the east and west hemispheres. Recall that the dielectric constant is determined by the first one or two wavelengths into the surface. Since the difference doesn't show up in the 6cm data, the roughness would need to be on the order of 2cm.

Finally a North-South comparison of the radio absorption length in this region shows that, within the error bars, the radio absorption lengths are about the same. But of course the error bars are large. Since the depth of the region sampled is determined by the estimated radio absorption length, it is a better estimator of the

similarity of the sub-surface in the two regions than the dielectric constants. Since the radio absorption lengths are the same for both data sets, this indicates the sub-surface has a degree of homogeneity, in the overlap region.

Shown in Figures 5.12 and 5.13 is the correlation of thermal inertia with the estimated effective dielectric constant at each wavelength. Unlike the Northern data set, the correlation of thermal inertia with the effective dielectric constant is not strong at either wavelength. The 6cm dielectric constant is poorly correlated with thermal inertia, as is the 2cm dielectric constant. Unlike the Northern data set, where both sets of effective dielectric constants were correlated with the thermal inertia, the Southern data sets are uncorrelated. This lack of correlation at both wavelengths implies that even at shallow sub-surface depths (greater than 4cm but less than 30cm), the sub-surface is not as similar to the surface as it was in the northern hemisphere, as indicated by the North data set. This casts some shadow of doubt on the veracity of using the infrared determined thermal inertias for depths greater than the diurnal thermal skin depth. Or it indicates that the fitting routine was so confused by this atypical region, that the resultant scatter from fitting is larger. However, since no other thermal inertias are available, the following results will be discussed under the assumption that the thermal inertias determined by Palluconi and Keiffer (1981) are good for the entire depth over which the thermal calculations were performed.

As with the North data set, the dielectric constants can be used to obtain an estimate of the effective sub-surface density. Using the same law derived from the work of Campbell and Ulrichs (1969), and others, as was used in Chapter 4, sub-surface densities were derived for both wavelengths. That is, a dielectric constant of 2.0 ± 0.1 was used for a powder of density 1 g cm^{-3}. The effective density was calculated for each wavelength at each of the latitudes for which a dielectric constant was calculated. The results are shown in Figure 5.14 and 5.15. The inner set of error

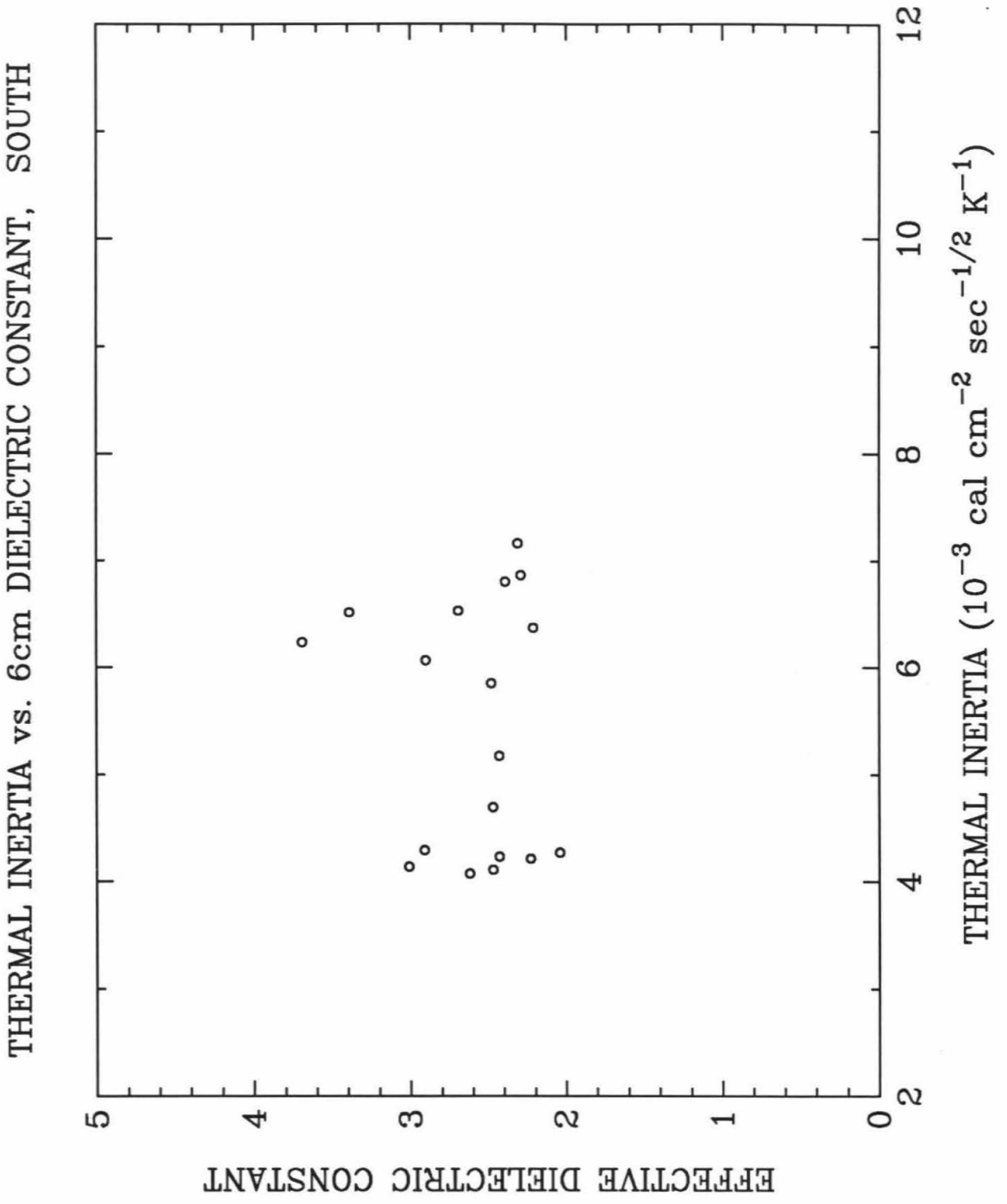

FIGURE 5.12: The correlation of the longitudinally averaged 2cm effective dielectric constant with the thermal inertia averaged in the same manner as the data are shown. The filled circles are those whose latitude is above the northern temperature discontinuity.

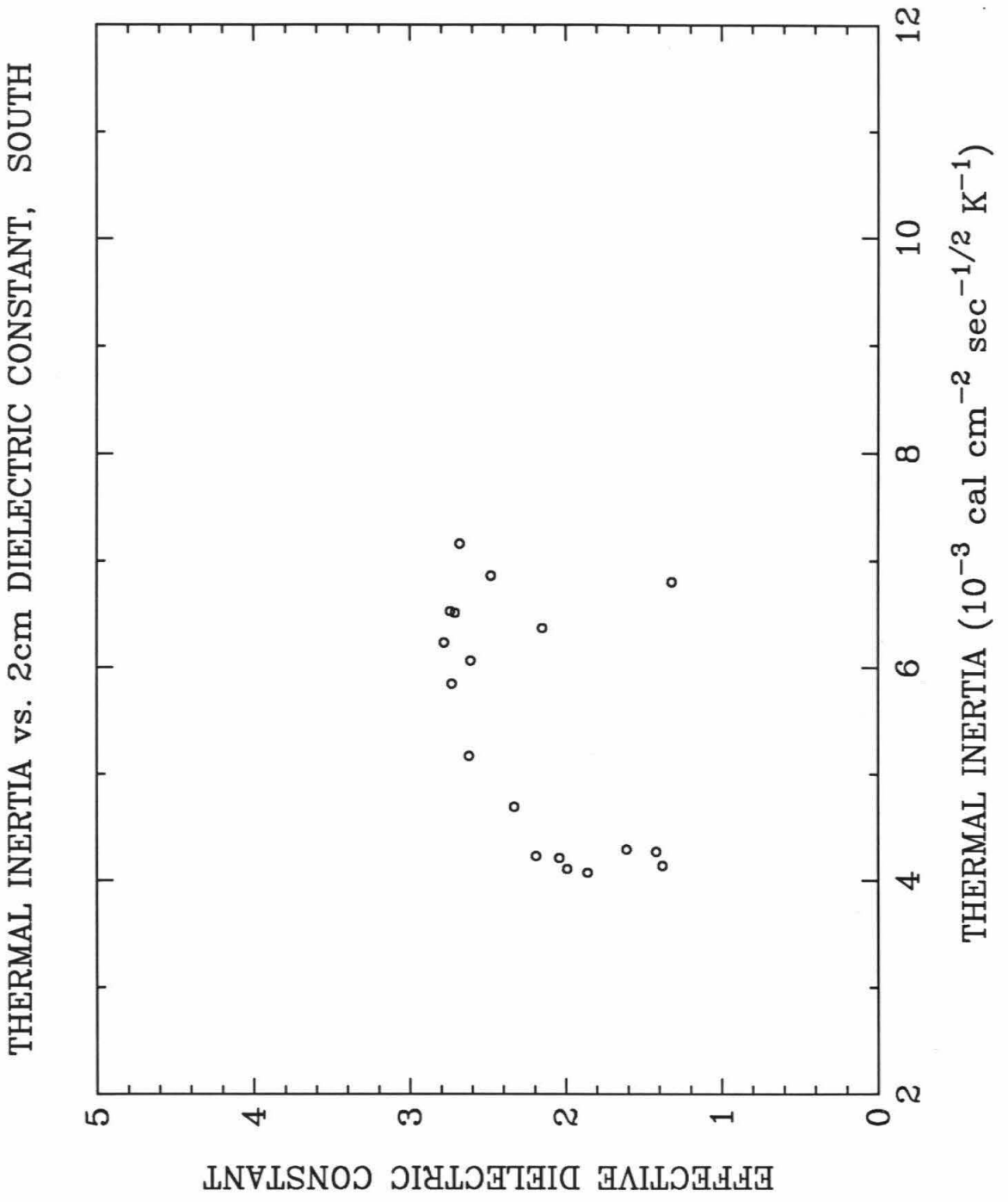

FIGURE 5.13: The correlation of the longitudinally averaged 6cm effective dielectric constant with the thermal inertia averaged in the same manner as the data are shown. The filled circles are those whose latitude is above the northern temperature discontinuity.

bars are calculated from the errors in the dielectric constant, just as was the case for the North data set. The outer set of error bars are an additional, combined error due to the scatter in the dielectric constant of the powders of rocks of different types, which was estimated from the data of Campbell and Ulrichs.

The densities derived from the 6cm data sets agree quite well, considering the error bars, in the region north of the anomalous region, that is, above 10°S. The 2cm effective densities, however, are much smaller for the South data set than they are for the North data set. In the region between 10°S and 25°S there is little agreement between the estimated densities at either wavelength. This divergence in the anomalous region is probably a manifestation of some difference in this region between the model's thermal parameters and the actual sub-surface. This is also apparent in the brightness temperature versus latitude plots. Because of this, the estimates of the effective density in this anomalous region are in doubt. Without a way to constrain the sub-surface physical properties of this region an accurate determination of the sub-surface density is not possible. Therefore, even though the densities are displayed herein, I don't believe their accuracy and merely present them for the sake of comparison. Rather I believe the explanation for the unusual behavior of the brightness temperature in this region lies in the thermal behavior of the sub-surface. The Viking infrared data should be examined for different seasons and see if any indication of this anomalous behavior is present. This would not be an easy task, because as seen before, a change in the thermal inertia below the diurnal thermal skin depth has a very small surface temperature manifestation.

Again, longitudinally averaged dielectric constants can be used to calculate a whole-disk dielectric constant. The result of this calculation for the 6cm data is 2.5 ± 0.3, and for the 2cm data, 2.2 ± 0.3. At both wavelengths the whole-disk dielectric constant calculated from the two different methods are in relatively good agreement

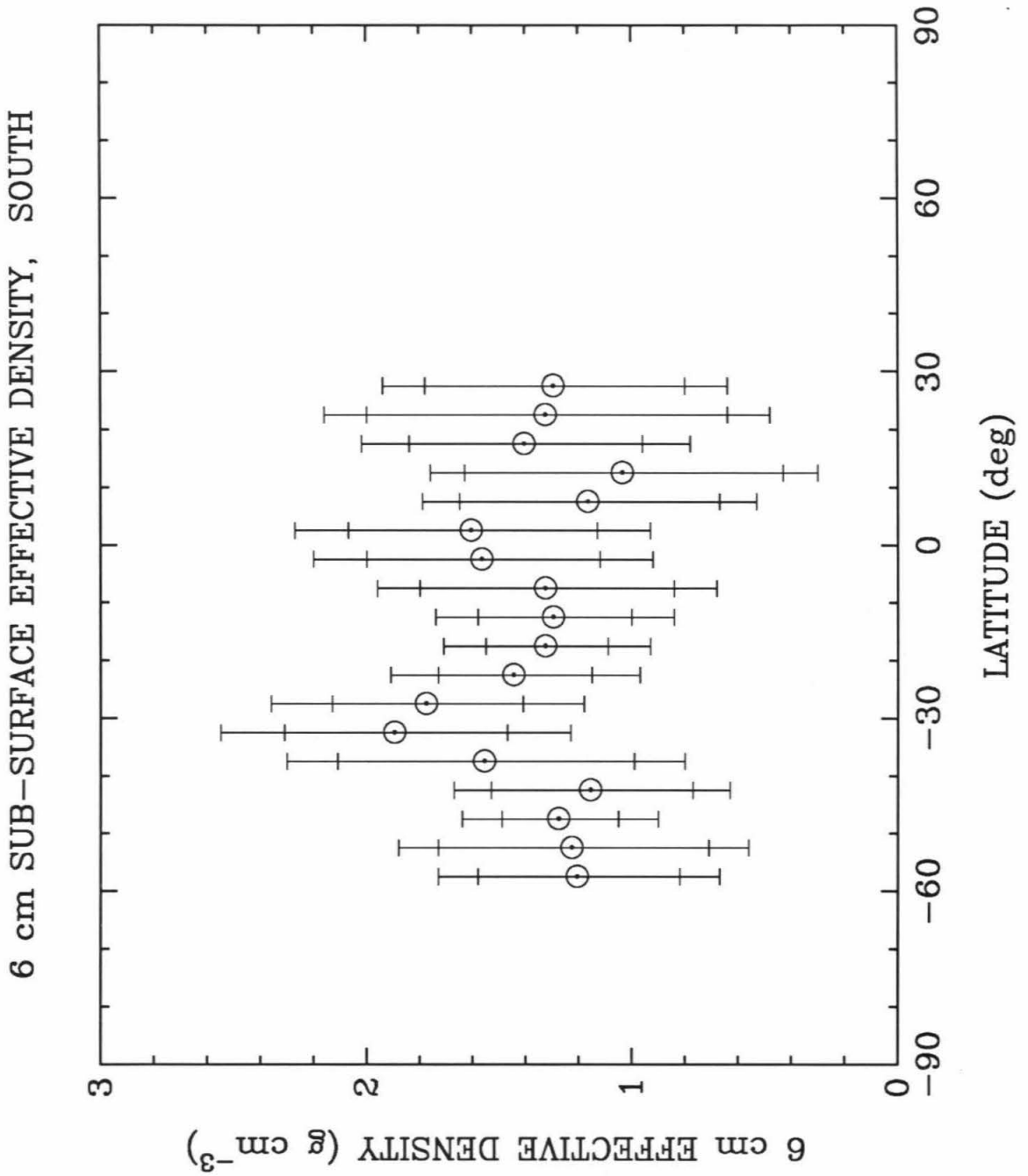

FIGURE 5.14: Estimates of the effective 2cm sub-surface density calculated from the effective dielectric constants. The inner error bars are directly derived from the error in estimating the effective dielectric constant. The additional error that goes into making the outer error bars is due to the spread in dielectric constants among the powders used to derive the empirical relation.

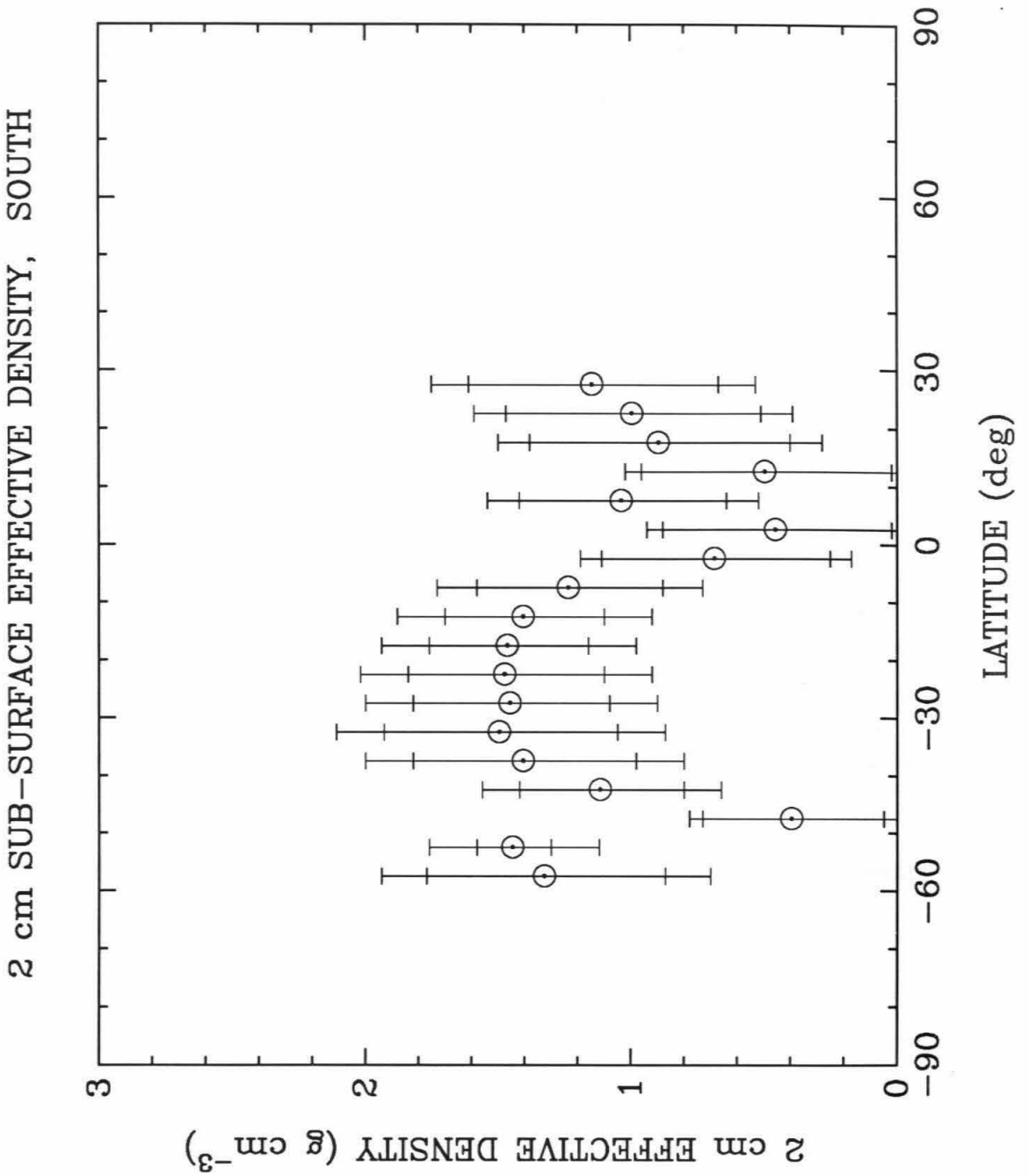

FIGURE 5.15: Estimates of the effective 6cm sub-surface density calculated from the effective dielectric constants. The inner error bars are directly derived from the error in estimating the effective dielectric constant. The additional error that goes into making the outer error bars is due to the spread in dielectric constants among the powders used to derive the empirical relation.

(2.7 vs. 2.5 at 6cm and 2.0 vs. 2.2 at 2cm). It is possible that the estimate of the map fitted whole-disk dielectric constant is too high due to calibration error, since, as stated earlier, a 3K difference between the model and the data is equivalent to a 0.3 change in the effective dielectric constant. Therefore, it wouldn't take much difference in the temperature to cause this discrepancy. It is more likely that this discrepancy is due to the fact that the dielectric constant estimated from the whole-disk polarization measurement is more sensitive to surface depolarization, particularly at the shorter wavelength. Unlike the North data set where the difference between the two methods is much larger at 2cm than at 6cm, the relative agreement here could be due to the re-normalization procedure. However, the fact that the two methods do not produce identical results indicates that the physical processes that go into determining each are quite distinct. Since the dielectric constant estimated from the whole-disk polarization measurement is more sensitive to surface roughness (via surface depolarization) the difference between the two methods could be explained by invoking surface roughness. This is because a rough surface depolarizes emission more than it changes the amount of emission (Muhleman, 1972). This would then appear as a lower effective dielectric constant than the longitudinally averaged dielectric constants.

CHAPTER 6
WHOLE-DISK BRIGHTNESS STUDIES

Because Mars is often used as a calibration source, its whole-disk brightness temperature is of paramount concern. This is especially true since some workers in the field believe that the flux standards used at observatories, like the VLA, are in error. This is especially true at the shorter wavelengths. This is because the observational studies used to establish these flux standards are old and use the measured flux at the longer wavelengths to estimate the flux at the shorter wavelengths. M. Klein (private communication) believes that the flux for the standard source 3C286 (Baars *et al.*, 1977) may be too small by 3 to 4% at 2cm. Thus it would be important if the flux from Mars could be accurately predicted from theoretical considerations. To help further this cause, I have calculated the whole-disk brightness of Mars for a variety of different observing geometries and various electrical parameters using the model described in Chapter 3. The purpose of this study is to see which parameters are important, which can be replaced by scaling factors. It is also a theoretical study of how large the variation in brightness temperature is. It is hoped that other observers will use the following charts and plots to estimate the whole-disk brightness temperature of Mars for calibration purposes. Even though not all possible cases have been tested against these tables, I would expect that estimating a whole-disk brightness temperature from the tables would be within five degrees of what the model would calculate for the same electrical and geometric parameters.

For example, in order to compare whole-disk brightness temperatures, many workers use an $R^{0.25}$ rule, R being the heliocentric distance, to account for the seasonal variation in the brightness of Mars. This is the rule I used in Chapters 4 and 5 to compare our whole-disk brightness temperatures to others. However, as it will become

obvious later, this rule is only approximately good and only for certain wavelengths. The tables and graphs in this chapter will, hopefully, allow better comparison between workers whose observations take place at different seasons and wavelengths. In addition, I hope it will provide a backdrop for those people who perform flux calibration measurements.

The procedure followed was to use the thermal model described in Chapter 2 and do the radiative transfer calculation for four dielectric constants, and ten radio absorption lengths. In addition, the space of all observing geometries was also sampled. Although some of the actual geometries are impossible to obtain from earth, they were included so that a better feel for the way the whole-disk brightness temperature varies throughout the parameter space may be developed. It will be shown that simple relationships exist between some of these discrete samplings and for others, the changes from one point in the parameter space to another will just be illustrated with graphs and tables. First a nominal model will be tabulated. This nominal model has a dielectric constant of 2.2, a sub-earth latitude of 0°N, a central meridian longitude of 75°W (the reason for this choice will become clear later), and a sub-earth time of day of noon, that is 0° phase angle. Following the presentation of this nominal model will be several sections which will discuss the anomalies in whole-disk brightness temperature that are caused by variations in the following parameters: dielectric constant, sub-earth longitude, sub-earth latitude, and phase angle (sub-earth time of day). Both computer time and the confusion inherent in trying to investigate the entire parameter space limited the detail of this investigation.

6.1 Nominal Model

In this section is offered the nominal model. That is, the whole-disk brightness

temperature as a function of the season on Mars is presented. As mentioned above, this representative model has a dielectric constant of 2.2, a sub-earth longitude of 75°W, a sub-earth latitude of 0°N, and a sub-earth time of day of noon. The whole disk brightness temperature was calculated at twenty-four equally spaced seasons for ten different radio absorption lengths. Equally spaced here means with respect to time and not with respect to L_S. The ten radio absorption lengths used were 5, 10, 15, 20, 30, 60, 100, 140, 200, and 300, all in units of cm. Most estimates of the whole-disk electrical parameters for centimeter observations fall somewhere in these regions.

Since the radio absorption lengths are given in units of centimeters, varying wavelengths and the radio absorption length constant, in units of the wavelength, can be combined to get the same radio absorption length in units of cm. For example, a wavelength of 3cm with a radio absorption length constant of 10λ yields a radio absorption length of 30cm. So does a wavelength of 2cm with a radio absorption length constant of 15λ. As will be seen below, it would be difficult, and inaccurate, to parametrize the variation of whole-disk brightness temperature due to changes in the radio absorption length in any simple manner. Because of this, all ten of the brightness temperature curves are presented in Figures 6.1 and 6.2. Table 6.1 is just a listing of the points that are presented in graphical form in Figures 6.1 and 6.2.

Figure 6.1 is the first five radio absorption lengths, the ones which are more strongly affected by the sub-earth time of day. That the sub-earth time of day is important can be seen from the fact that the averages, over season, of the curves are not coincident. This is because the part of the diurnal curve sampled in Figure 6.1 is at noon. Obviously, what part of the diurnal curve is sampled is irrelevant if the diurnal wave is unimportant, and the only variation between the curves will be a change in amplitude due to the seasonal wave. This is seen in Figure 6.2 in which

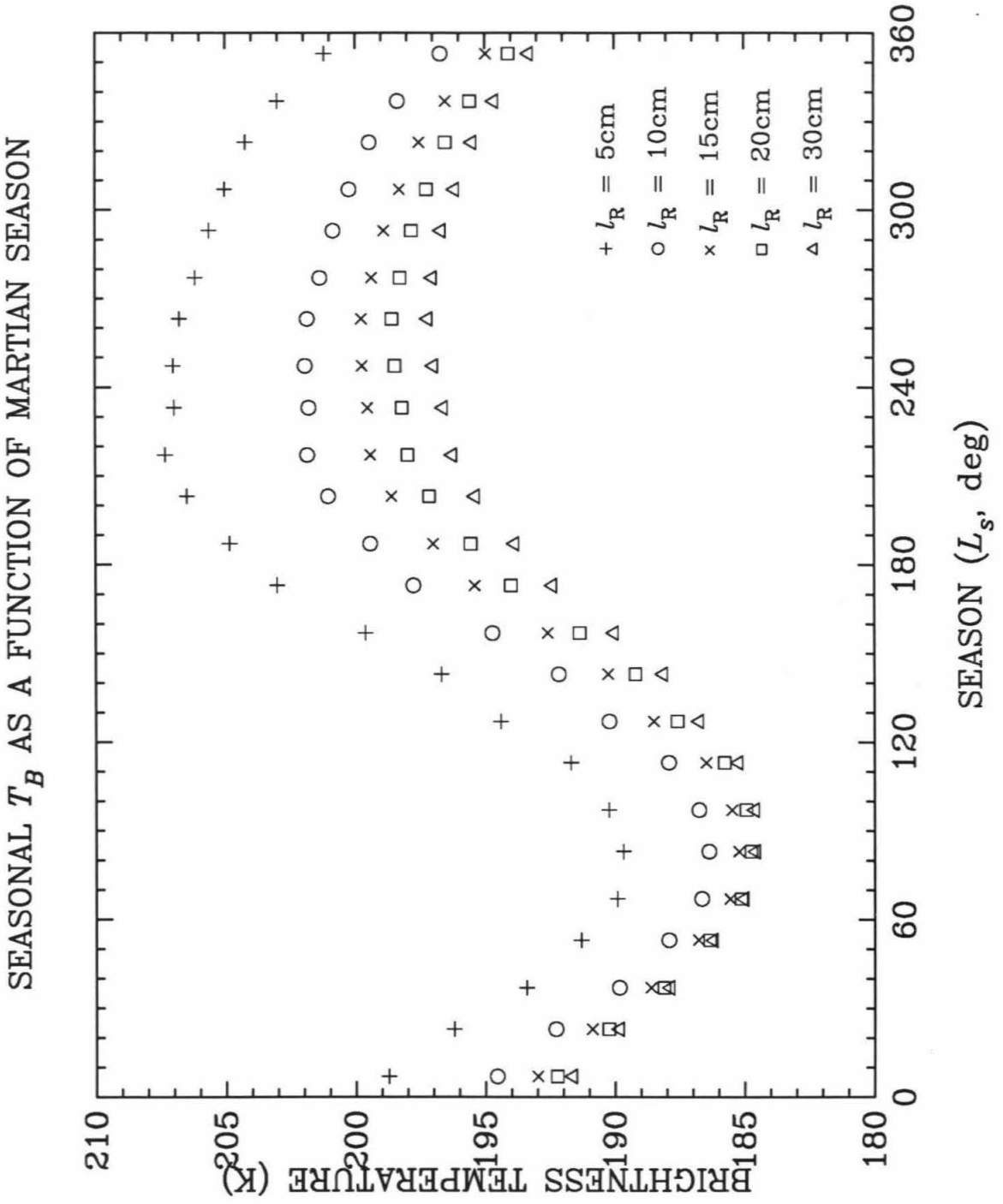

FIGURE 6.1: The variation of brightness temperature as a function of the Martian season is illustrated for the first five radio absorption lengths used. The sub-earth longitude for all the curves was 75°W, the sub-earth latitude was 0°N, the phase angle was 0°, and the dielectric constant was 2.2.

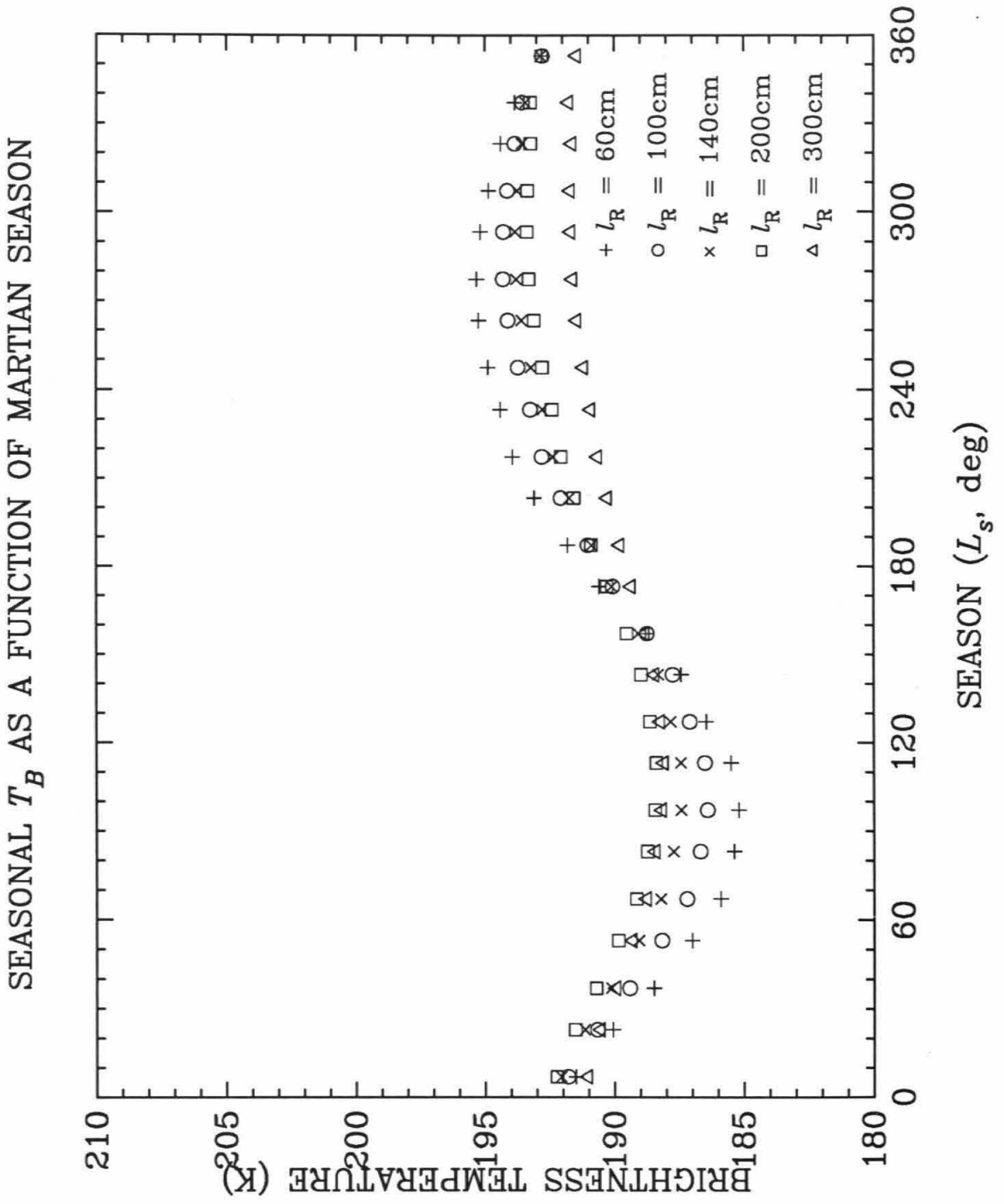

FIGURE 6.2: The variation of brightness temperature as a function of the Martian season is illustrated for last five radio absorption lengths used. The sub-earth longitude for all the curves was 75°W, the sub-earth latitude was 0°N, the phase angle was 0°, and the dielectric constant was 2.2.

TABLE 6.1

Nominal Model								
	L_S=8°	L_S =23°	L_S=37°	L_S=53°	L_S=69°	L_S=82°	L_S=98°	L_S=112°
l_R	R=1.58	R=1.61	R=1.64	R=1.66	R=1.67	R=1.66	R=1.65	R=1.63
5cm	198.7K	196.2K	193.4K	191.3K	189.9K	189.7K	190.2K	191.7K
10cm	194.6K	192.3K	189.8K	187.9K	186.7K	186.4K	186.8K	187.9K
15cm	193.0K	190.9K	188.6K	186.8K	185.6K	185.2K	185.5K	186.5K
20cm	192.2K	190.3K	188.1K	186.4K	185.1K	184.8K	184.9K	185.8K
30cm	191.6K	189.8K	187.9K	186.2K	185.0K	184.6K	184.6K	185.2K
60cm	191.5K	190.1K	188.5K	187.0K	185.9K	185.4K	185.2K	185.5K
100cm	191.8K	190.7K	189.4K	188.2K	187.2K	186.7K	186.4K	186.5K
140cm	192.1K	191.1K	190.1K	189.1K	188.2K	187.7K	187.4K	187.4K
200cm	192.2K	191.5K	190.7K	189.9K	189.1K	188.7K	188.4K	188.4K
300cm	191.0K	190.5K	189.9K	189.3K	188.8K	188.4K	188.2K	188.1K
	L_S=129°	L_S=141°	L_S=157°	L_S=174°	L_S=188°	L_S=203°	L_S=219°	L_S=232°
l_R	R=1.59	R=1.56	R=1.52	R=1.48	R=1.45	R=1.42	R=1.40	R=1.39
5cm	194.4K	196.7K	199.6K	203.0K	204.9K	206.5K	207.3K	207.0K
10cm	190.2K	192.2K	194.7K	197.8K	199.4K	201.1K	201.9K	201.8K
15cm	188.5K	190.3K	192.6K	195.4K	197.0K	198.6K	199.4K	199.5K
20cm	187.6K	189.2K	191.4K	194.0K	195.6K	197.1K	198.0K	198.2K
30cm	186.8K	188.1K	190.0K	192.4K	193.9K	195.4K	196.2K	196.6K
60cm	186.4K	187.4K	188.8K	190.6K	191.8K	193.1K	193.9K	194.4K
100cm	187.1K	187.7K	188.7K	190.1K	191.0K	192.1K	192.8K	193.2K
140cm	187.8K	188.3K	189.1K	190.1K	190.9K	191.7K	192.4K	192.8K
200cm	188.6K	189.0K	189.5K	190.3K	190.9K	191.6K	192.1K	192.4K
300cm	188.2K	188.4K	188.8K	189.3K	189.8K	190.3K	190.6K	190.9K
	L_S=248°	L_S=264°	L_S=280°	L_S=293°	L_S=308°	L_S=323°	L_S=337°	L_S=353°
l_R	R=1.38	R=1.38	R=1.40	R=1.41	R=1.44	R=1.47	R=1.50	R=1.54
5cm	207.0K	206.8K	206.1K	205.6K	205.0K	204.2K	203.0K	201.2K
10cm	201.9K	201.9K	201.4K	200.9K	200.2K	199.4K	198.4K	196.7K
15cm	199.7K	199.8K	199.4K	198.9K	198.3K	197.5K	196.5K	195.0K
20cm	198.5K	198.6K	198.3K	197.8K	197.2K	196.5K	195.6K	194.1K
30cm	197.0K	197.2K	197.0K	196.7K	196.1K	195.5K	194.6K	193.3K
60cm	194.9K	195.2K	195.3K	195.2K	194.9K	194.4K	193.8K	192.8K
100cm	193.7K	194.1K	194.3K	194.3K	194.1K	193.8K	193.6K	192.8K
140cm	193.2K	193.6K	193.8K	193.8K	193.8K	193.6K	193.4K	192.8K
200cm	192.8K	193.1K	193.3K	193.4K	193.4K	193.2K	193.2K	192.8K
300cm	191.2K	191.4K	191.6K	191.7K	191.7K	191.6K	191.8K	191.5K

the curves for different radio absorption lengths overlay one another fairly closely and differ only in amplitude. As the importance of the diurnal wave in the integral determining the whole-disk brightness temperature increases, so will the difference between the seasonal curves. This is easily seen in Figure 6.1 in which the curve for the smallest radio absorption length is also the hottest curve. If the part of the diurnal wave sampled was 0:00 hours (i.e., midnight) then this curve would have been the coldest and the curves in Figure 6.2 would have changed only marginally.

Another thing that is noticeable in both sets of curves is that the minimum brightness temperature occurs at different seasons for different radio absorption lengths. This delaying of the minimum brightness temperature is easily understood as the propagation of the seasonal thermal wave into the sub-surface. The amount of delay can be estimated by using the linear theory expounded by Piddington and Minat (1949), Muhleman (1972), and others. If the seasonal variation of the surface temperature is approximated by the first component of its Fourier decomposition, then the delay is given by

$$\Psi_n = \Psi_0 + tan^{-1}\left[\frac{l_{\mathrm{R,n}}}{l_T + l_{\mathrm{R,n}}}\right]$$

where l_T is the seasonal thermal skin depth and is assumed to be 120cm for the current calculation. Additionally, $l_{\mathrm{R,n}}$ is the nth radio absorption length. The subscript n is used here to indicate that the same l_R may be obtained by using different wavelengths and different radio absorption length constants. Ψ_0 is the L_S at which the whole-disk surface temperature is a minimum. It can be calculated from the models and is estimated to be 77.15°.

Figure 6.3 compares this theoretical curve with the actual delays. The disagreement between the two is mostly attributable to the fact the diurnally averaged surface temperature needs more than one Fourier component to describe its variation throughout the Martian year. That is, the diurnally averaged surface temperature is not a

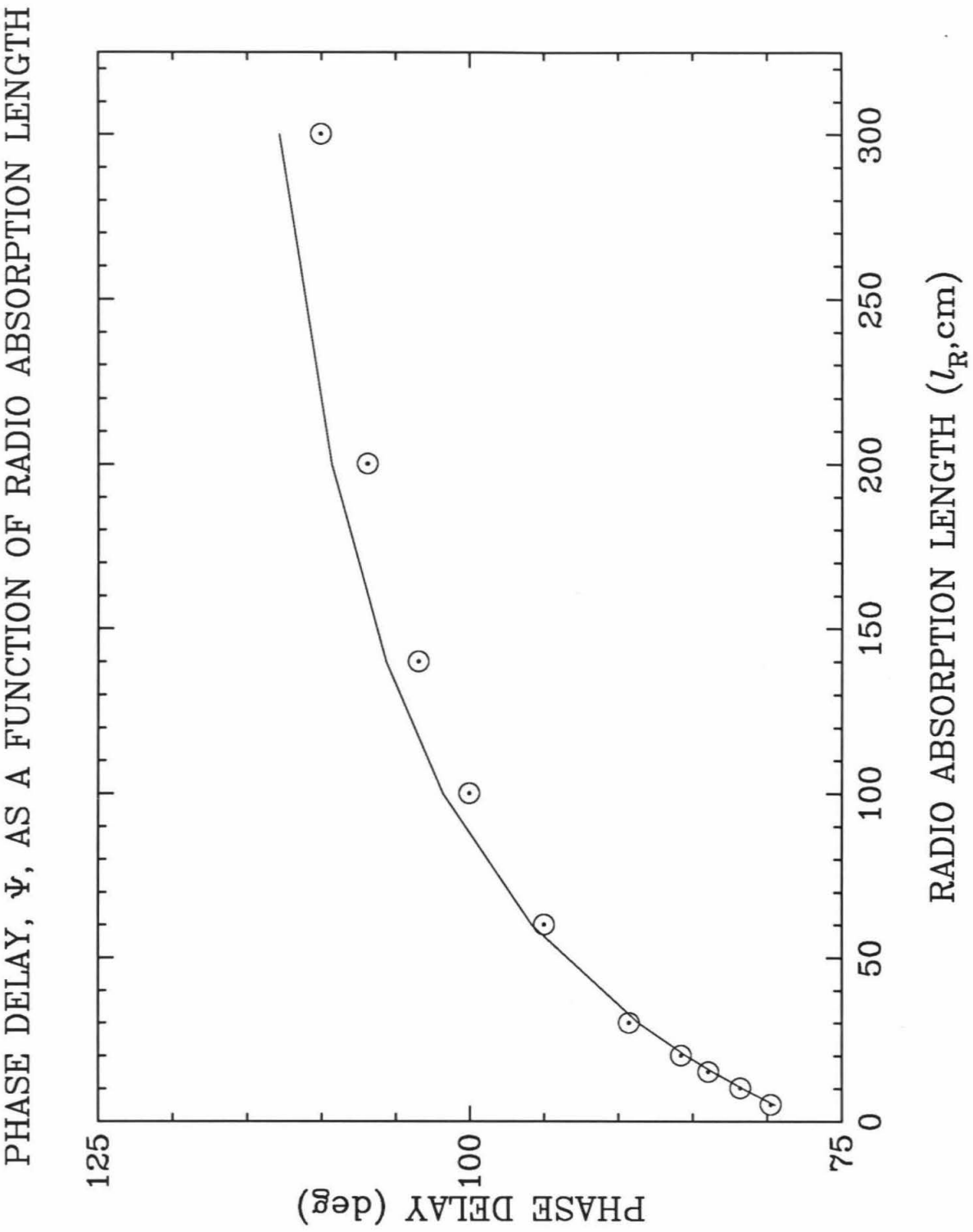

FIGURE 6.3: Delay of the seasonal temperature variation minimum with respect to the radio absorption length. The points are the delays estimated from the models, and the line is the theoretical curve assuming only one Fourier component.

perfect sinusoid. The uncertainty in the seasonal thermal skin depth estimate used for the theoretical calculation is an additional factor that can help explain the difference. Since the thermal parameters vary over the disk, the phase is not zero when the heliocentric distance is at a maximum, but rather occurs slightly later. This can be seen in Table 6.1 which, in addition to the whole-disk brightness temperatures and the season, lists the heliocentric distance, in AU. That is, the disk-averaged surface temperature is not at a minimum when Mars is furthest from the sun, $L_S = 70.9°$ and $R \sim 1.67$AU, but slightly later, at $L_S = 77.15°$.

Since the minima of these curves do not occur at the same season for all wavelengths and since none of the minima occur when Mars is furthest from the sun, it is not a good idea to use any power of the heliocentric distance as a scaling factor. In order to use an $R^{0.25}$ scaling law to compare measurements at different seasons, first the offset between the maximum R and the minimum of the seasonal brightness temperature curve for a given wavelength should be calculated. And even this does not guarantee that the power is the correct one. Rather than attempt to come up with a scaling law, that would have large errors at best, I have tabulated the brightness temperatures at each of the different radio absorption lengths at each of the different seasons in Table 6.1. Deviations from these whole-disk brightness temperatures caused by parameters other than the nominal ones, will be discussed in subsequent sections.

6.2 Variation with Dielectric Constant

In order to illustrate the changes to the nominal model due only to variations in the dielectric constant, the sub-earth latitude will be held at 0°N in this section. In addition, the nominal value of 75°W will be used for the sub-earth longitude, and

noon will remain the sub-earth time of day (i.e., phase angle = 0°). The models were run with four different dielectric constants for each of the ten different radio absorption lengths. The values used for the dielectric constants were 1.4, 2.2, 3.0 and 3.8.

From Figure 6.4 it is relatively easy to see that, for the wavelength chosen, all of the curves are similar. Other curves, not included, show the same similarity for each of the radio absorption lengths investigated. The numbers in Table 6.2 were calculated by dividing the curve for $\epsilon \equiv \epsilon_2 = 2.2$ by each of the remaining curves, $\epsilon_1 = 1.4, \epsilon_3 = 3.0, \epsilon_4 = 3.8$, for each of the ten radio absorption lengths. These ratios are shown for all 4 dielectric constants and for the ten radio absorption lengths for which models were calculated. Since each of the curves in Figure 6.4 is actually twenty-four points, the twenty-four different seasons, a standard deviation may be calculated. The formal errors calculated from the variation of a curve to the scaled ϵ_2 curve are shown next to the ratios in Table 6.1. Note that most are very small, indicating that scaling the ϵ_2 curve is a very good approximation. That is, there appears to be very little seasonal variation in the scaling factor.

In addition, the scaling factors for different radio absorption lengths do not differ by much, indicating that the same empirical relationships exist, to within a small fraction, at all wavelengths. This was to be expected, because in the equation of radiative transfer the dielectric constant and the radio absorption length are essentially in two different terms which are then multiplied to get the whole-disk brightness. This means the variation of one has minimal effect on the term involving the other. The only cross-term is because the dielectric constant, through Snell's law, determines the angle along which the integral with depth is performed (see Equation 3.4). Since the change in the sub-surface incident angle changes very little over the range of dielectric constants used, this is a minor effect.

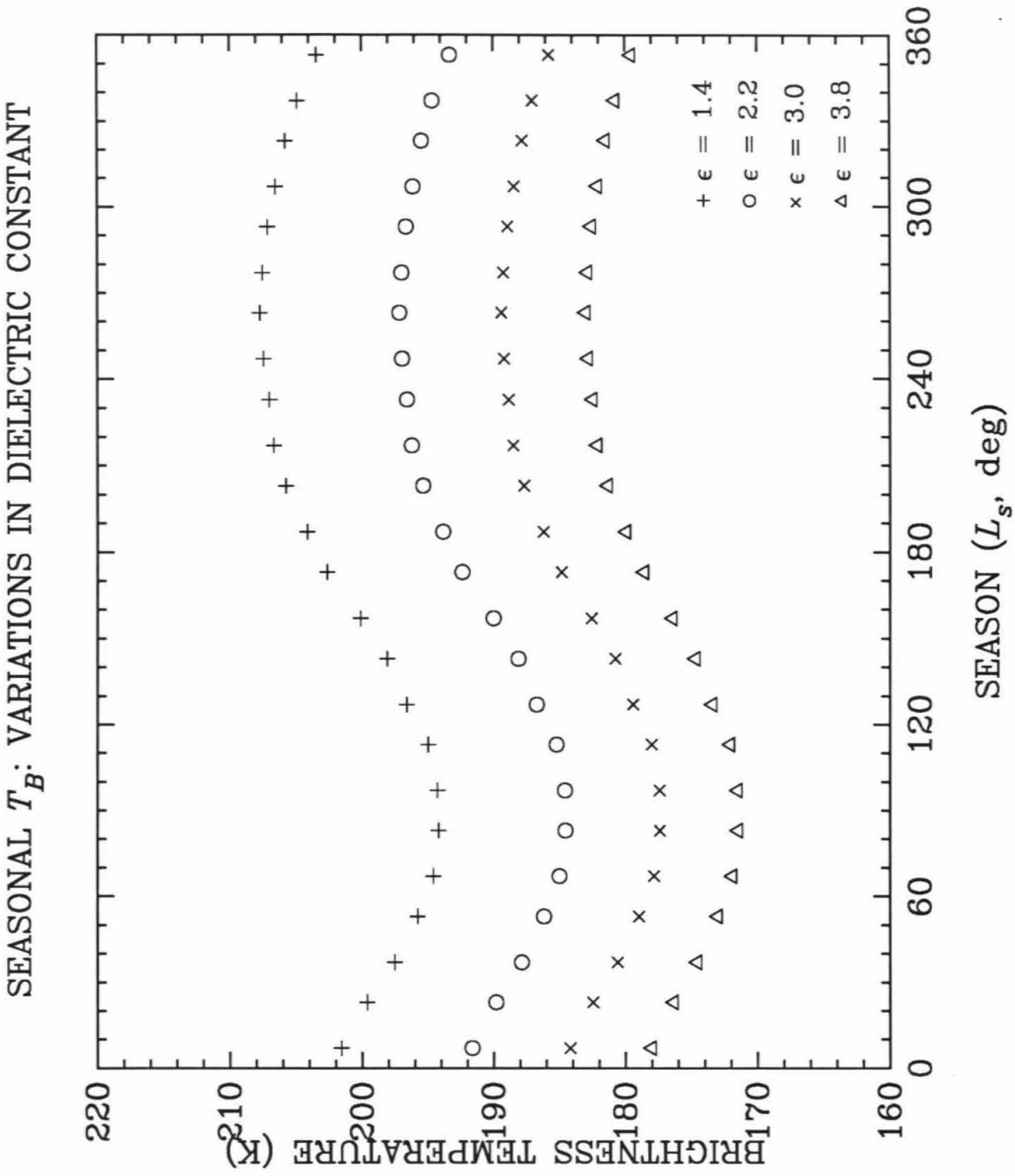

FIGURE 6.4: The variation of brightness temperature as a function of the Martian season for several different dielectric constants is shown. These cases are all for a wavelength of 2cm with a radio absorption length of 15 wavelengths (or equivalently 30cm). The sub-earth latitude is 0°N, the sub-earth longitude is 75°W, and the phase angle is 0°.

TABLE 6.2

Comparison Dielectric Constant Variations								
	$\epsilon_1 = 1.4$		$\epsilon_2 = 2.2$		$\epsilon_3 = 3.0$		$\epsilon_4 = 3.8$	
l_R	R_1 [a]	σ_1 [b]	R_2 [a]	σ_2 [b]	R_3 [a]	σ_3 [b]	R_4 [a]	σ_4 [b]
5cm	0.9487	2.842×10^{-4}	1.0	0.0	1.0414	1.227×10^{-4}	1.0781	1.806×10^{-4}
10cm	0.9490	3.504×10^{-4}	1.0	0.0	1.0411	1.488×10^{-4}	1.0776	2.642×10^{-4}
15cm	0.9493	4.262×10^{-4}	1.0	0.0	1.0410	1.763×10^{-4}	1.0773	3.045×10^{-4}
20cm	0.9495	4.904×10^{-4}	1.0	0.0	1.0408	2.041×10^{-4}	1.0771	3.478×10^{-4}
30cm	0.9499	6.037×10^{-4}	1.0	0.0	1.0407	2.591×10^{-4}	1.0769	4.267×10^{-4}
60cm	0.9505	7.942×10^{-4}	1.0	0.0	1.0404	3.440×10^{-4}	1.0764	5.451×10^{-4}
100cm	0.9509	8.448×10^{-4}	1.0	0.0	1.0402	3.760×10^{-4}	1.0761	5.599×10^{-4}
140cm	0.9512	8.156×10^{-4}	1.0	0.0	1.0401	3.289×10^{-4}	1.0760	5.129×10^{-4}
200cm	0.9512	7.000×10^{-4}	1.0	0.0	1.0402	2.875×10^{-4}	1.0761	4.391×10^{-4}
300cm	0.9491	5.584×10^{-4}	1.0	0.0	1.0415	2.025×10^{-4}	1.0783	3.447×10^{-4}

[a] R_n is the ratio of the seasonal curve for $\epsilon_2 = 2.2$ divided by the seasonal curve for ϵ_n.

[b] σ_n is an unbiased estimator of the standard deviation of the ratio R_n over one Martian season.

Since the scaling factor increases with dielectric constant, it is tempting to see if a simple relationship exists between the scaling factor and the dielectric constant. Even though a linear interpolation between the different values of ϵ produced a relatively good estimate, an even better method to interpolate between the different curves was obtained by first taking the square root of the dielectric constant and then using a linear interpolation. Another way to state this is that the whole-disk emissivity scales as the index of refraction. This is a useful parametrization because it allows a relatively accurate interpolation between the curves. Since, for a given radio absorption length, a change in dielectric constant is well parametrized by just a scaling factor, all of the following sections will assume a dielectric constant of 2.2. The whole-disk brightness temperature for any other dielectric constant may be easily obtained by using the information in Table 6.2

6.3 Variation with Longitude

For the purposes of this chapter the Martian day was divided into 36 equal parts. This means each longitude bin is roughly equivalent to about 40 minutes of time. These bins are centered on every 10 degrees starting at a sub-earth longitude of 5°W and ending at a sub-earth longitude of 355°W. Any integration period can be approximated by averaging the results for all the sub-earth longitudes that occurred during a particular observing run. To reduce the number of cases to be inspected and since changes in the dielectric constant appear as scaling factors, only one dielectric constant will be used in all the following analysis. For simplicity, and in keeping with the previous section, I have chosen $\epsilon = 2.2$ for this role.

Figure 6.5 shows the seasonal brightness temperature variations for several different sub-earth longitudes. I tried to choose several curves which illustrate the entire range of variation. The three sub-earth longitudes that were used to obtain the curves in Figure 6.5 were $\Theta = 35°\text{W}$, $\Theta = 75°\text{W}$, and $\Theta = 135°\text{W}$. As can be seen by looking at the figure, this range of variation is not very large. For the sake of clarity all the cases shown have the same dielectric constant, $\epsilon = 2.2$, and the same radio absorption length, $l_{\text{R}} = 30\text{cm}$. Because the whole-disk brightness temperature is an average over many longitudes, albeit weighted strongly towards the sub-earth point, and since the surface physical parameters (thermal inertia and albedo) do not have an exceptionally strong east-west hemispheric difference, the variations in whole-disk brightness temperature are not very large. Most variations are within two percent of the median curve. This means that the largest variations in the whole-disk brightness temperatures are on the order of 8K. This agrees well with the published estimates of the whole-disk brightness temperature variations (c.f. Jakosky and Muhleman, 1980).

A more significant difference at shorter wavelengths is the variation of the bright-

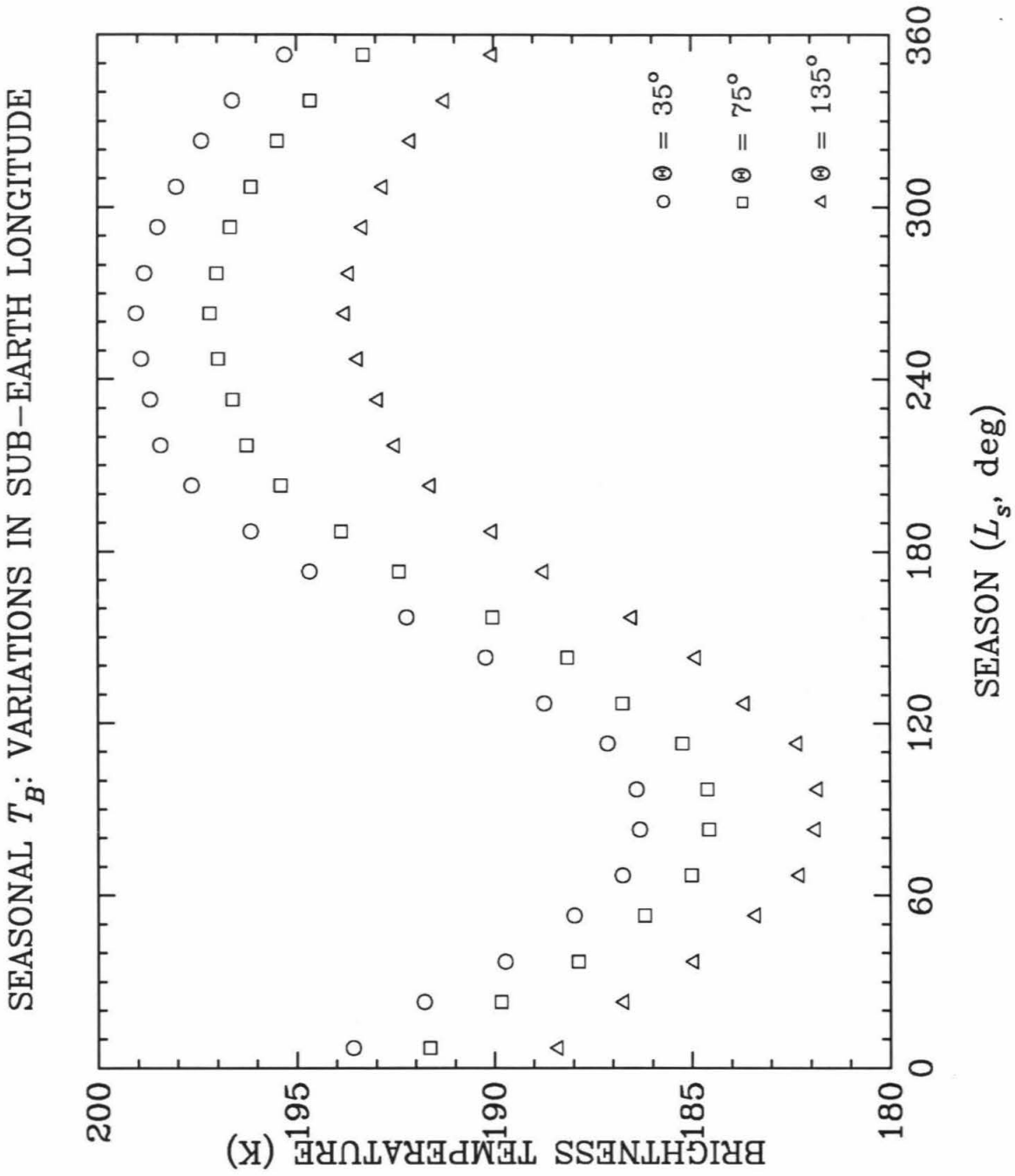

FIGURE 6.5: The variation of brightness temperature as a function of the Martian season is illustrated for several different sub-earth longitudes. The particular cases shown have a wavelength of 2cm with a radio absorption length of 15 wavelengths (or equivalently 30cm) and a dielectric constant of 2.2. The sub-earth latitude is 0°N and the phase angle is 0°.

ness temperature with changes in sub-earth time of day and to a lesser extent the variation with changes in the sub-earth latitude. In addition, once the electrical parameters become more strongly constrained, larger variations may appear as different dielectric constants and radio absorption lengths become associated with different longitudes. Indeed, the correlation of thermal inertia and dielectric constant illustrated in Chapter 4 could be used at present to estimate what effect would be had on the whole-disk brightness temperatures by variations in the electrical parameters.

Table 6.3a,b,c illustrates the variation among all the different sub-earth longitudes and radio absorption lengths. These ratios were calculated in a manner very similar to those in Table 6.2. The seasonal curves were all divided by the curve at 75°W to obtain ratios which can be used to easily get from the nominal model to a whole-disk brightness temperature at a different radio absorption length and different sub-earth longitude. Error estimates were calculated at the same time as the ratios. Again, this can be done because the seasonal variations consist of twenty-four points whose difference from the scaled nominal curve can be used to estimate a standard deviation. I chose, for the purposes of normalization, a curve fairly close to the median. It happened that the sub-earth longitude of this normalization curve was 75°W longitude. This is the reason that the nominal model has a sub-earth longitude of 75°W, this longitude has a seasonal brightness temperature curve which is near the median of the seasonal brightness temperature curves for all longitudes. Both the ratios and the error estimates are shown for the ten different radio absorption lengths used. As with the variations due to changes in dielectric constant, the variations due to changes in sub-earth longitude are subject to the caveat that the thermal parameters above 60°N and below 60°S are estimated from the adjacent latitudes because the data of Palluconi and Keiffer (1981) do not extend into these regions. However, because these regions are at higher latitudes, their projected areas are

TABLE 6.3a

Comparison of Seasonal Temperatures: Sub-earth Longitude Variations								
Long.	$\Phi = 5°W$		$\Phi = 15°W$		$\Phi = 25°W$		$\Phi = 35°W$	
l_R	R_5	σ_5	R_{15}	σ_{15}	R_{25}	σ_{25}	R_{35}	σ_{35}
5 cm	1.0114	4.22×10^{-4}	1.0128	3.81×10^{-4}	1.0139	4.06×10^{-4}	1.0140	4.33×10^{-4}
10 cm	1.0092	5.61×10^{-4}	1.0104	5.36×10^{-4}	1.0114	5.26×10^{-4}	1.0118	5.20×10^{-4}
15 cm	1.0090	6.57×10^{-4}	1.0100	6.56×10^{-4}	1.0108	6.49×10^{-4}	1.0109	6.22×10^{-4}
20 cm	1.0092	7.41×10^{-4}	1.0100	7.42×10^{-4}	1.0106	7.40×10^{-4}	1.0106	7.17×10^{-4}
30 cm	1.0096	8.36×10^{-4}	1.0101	8.41×10^{-4}	1.0105	8.39×10^{-4}	1.0102	8.02×10^{-4}
60 cm	1.0099	8.94×10^{-4}	1.0101	9.01×10^{-4}	1.0102	8.76×10^{-4}	1.0097	8.34×10^{-4}
100cm	1.0095	8.09×10^{-4}	1.0096	8.03×10^{-4}	1.0095	7.87×10^{-4}	1.0090	7.31×10^{-4}
140cm	1.0090	7.21×10^{-4}	1.0091	7.04×10^{-4}	1.0090	6.97×10^{-4}	1.0084	6.43×10^{-4}
200cm	1.0084	6.08×10^{-4}	1.0084	5.95×10^{-4}	1.0082	5.61×10^{-4}	1.0077	5.41×10^{-4}
300cm	1.0076	4.59×10^{-4}	1.0076	4.34×10^{-4}	1.0074	4.06×10^{-4}	1.0069	3.90×10^{-4}
Long.	$\Phi = 45°W$		$\Phi = 55°W$		$\Phi = 65°W$		$\Phi = 75°W$	
l_R	R_{45}	σ_{45}	R_{55}	σ_{55}	R_{65}	σ_{65}	R_{75}	σ_{75}
5 cm	1.0127	4.49×10^{-4}	1.0098	3.79×10^{-4}	1.0054	2.28×10^{-4}	1.0000	0.00
10 cm	1.0108	4.81×10^{-4}	1.0085	3.91×10^{-4}	1.0048	2.26×10^{-4}	1.0000	0.00
15 cm	1.0100	5.61×10^{-4}	1.0078	4.35×10^{-4}	1.0044	2.41×10^{-4}	1.0000	0.00
20 cm	1.0096	6.20×10^{-4}	1.0074	4.85×10^{-4}	1.0041	2.71×10^{-4}	1.0000	0.00
30 cm	1.0091	6.97×10^{-4}	1.0070	5.12×10^{-4}	1.0039	2.88×10^{-4}	1.0000	0.00
60 cm	1.0085	7.11×10^{-4}	1.0064	5.16×10^{-4}	1.0035	3.01×10^{-4}	1.0000	0.00
100cm	1.0078	6.17×10^{-4}	1.0058	4.64×10^{-4}	1.0031	2.33×10^{-4}	1.0000	0.00
140cm	1.0072	5.43×10^{-4}	1.0054	3.99×10^{-4}	1.0029	2.26×10^{-4}	1.0000	0.00
200cm	1.0066	4.51×10^{-4}	1.0049	3.37×10^{-4}	1.0027	1.99×10^{-4}	1.0000	0.00
300cm	1.0059	3.35×10^{-4}	1.0044	2.51×10^{-4}	1.0024	1.58×10^{-4}	1.0000	0.00
Long.	$\Phi = 85°W$		$\Phi = 95°W$		$\Phi = 105°W$		$\Phi = 115°W$	
l_R	R_{85}	σ_{85}	R_{95}	σ_{95}	R_{105}	σ_{105}	R_{115}	σ_{115}
5 cm	0.9942	2.60×10^{-4}	0.9887	5.12×10^{-4}	0.9839	7.59×10^{-4}	0.9802	9.72×10^{-4}
10 cm	0.9948	2.70×10^{-4}	0.9896	5.40×10^{-4}	0.9850	7.87×10^{-4}	0.9814	1.01×10^{-4}
15 cm	0.9952	2.71×10^{-4}	0.9904	5.61×10^{-4}	0.9862	8.31×10^{-4}	0.9829	1.05×10^{-4}
20 cm	0.9955	2.93×10^{-4}	0.9910	5.86×10^{-4}	0.9870	8.68×10^{-4}	0.9839	1.11×10^{-4}
30 cm	0.9958	3.08×10^{-4}	0.9917	6.26×10^{-4}	0.9880	9.27×10^{-4}	0.9852	1.16×10^{-4}
60 cm	0.9963	3.19×10^{-4}	0.9927	6.23×10^{-4}	0.9896	9.15×10^{-4}	0.9872	1.16×10^{-4}
100cm	0.9967	2.70×10^{-4}	0.9934	5.42×10^{-4}	0.9906	8.01×10^{-4}	0.9885	1.03×10^{-4}
140cm	0.9969	2.44×10^{-4}	0.9939	4.67×10^{-4}	0.9913	6.96×10^{-4}	0.9893	8.85×10^{-4}
200cm	0.9972	1.91×10^{-4}	0.9945	3.77×10^{-4}	0.9921	5.69×10^{-4}	0.9903	7.22×10^{-4}
300cm	0.9975	1.29×10^{-4}	0.9950	3.02×10^{-4}	0.9929	4.37×10^{-4}	0.9913	5.53×10^{-4}

TABLE 6.3b

Comparison of Seasonal Temperatures: Sub-earth Longitude Variations								
Long.	$\Phi = 125°W$		$\Phi = 135°W$		$\Phi = 145°W$		$\Phi = 155°W$	
l_R	R_{125}	σ_{125}	R_{135}	σ_{135}	R_{145}	σ_{145}	R_{155}	σ_{155}
5cm	0.9780	1.13×10^{-3}	0.9773	1.23×10^{-3}	0.9780	1.28×10^{-3}	0.9800	1.27×10^{-3}
10cm	0.9791	1.20×10^{-3}	0.9782	1.30×10^{-3}	0.9787	1.36×10^{-3}	0.9803	1.37×10^{-3}
15cm	0.9808	1.24×10^{-3}	0.9799	1.36×10^{-3}	0.9803	1.41×10^{-3}	0.9819	1.43×10^{-3}
20cm	0.9819	1.29×10^{-3}	0.9812	1.41×10^{-3}	0.9817	1.47×10^{-3}	0.9831	1.48×10^{-3}
30cm	0.9835	1.36×10^{-3}	0.9829	1.49×10^{-3}	0.9834	1.55×10^{-3}	0.9848	1.58×10^{-3}
60cm	0.9858	1.37×10^{-3}	0.9853	1.49×10^{-3}	0.9858	1.57×10^{-3}	0.9872	1.62×10^{-3}
100cm	0.9872	1.20×10^{-3}	0.9868	1.32×10^{-3}	0.9873	1.40×10^{-3}	0.9886	1.46×10^{-3}
140cm	0.9882	1.03×10^{-3}	0.9878	1.15×10^{-3}	0.9883	1.21×10^{-3}	0.9894	1.28×10^{-3}
200cm	0.9892	8.50×10^{-4}	0.9889	9.39×10^{-4}	0.9892	1.00×10^{-3}	0.9902	1.06×10^{-3}
300cm	0.9903	6.64×10^{-4}	0.9900	7.27×10^{-4}	0.9903	7.71×10^{-4}	0.9911	8.13×10^{-4}
Long.	$\Phi = 165°W$		$\Phi = 175°W$		$\Phi = 185°W$		$\Phi = 195°W$	
l_R	R_{165}	σ_{165}	R_{175}	σ_{175}	R_{185}	σ_{185}	R_{195}	σ_{195}
5cm	0.9830	1.22×10^{-3}	0.9867	1.13×10^{-3}	0.9909	1.02×10^{-3}	0.9951	9.09×10^{-4}
10cm	0.9828	1.33×10^{-3}	0.9861	1.25×10^{-3}	0.9897	1.16×10^{-3}	0.9935	1.08×10^{-3}
15cm	0.9842	1.39×10^{-3}	0.9872	1.32×10^{-3}	0.9906	1.24×10^{-3}	0.9942	1.16×10^{-3}
20cm	0.9854	1.46×10^{-3}	0.9883	1.40×10^{-3}	0.9915	1.33×10^{-3}	0.9949	1.27×10^{-3}
30cm	0.9870	1.55×10^{-3}	0.9897	1.52×10^{-3}	0.9928	1.46×10^{-3}	0.9960	1.42×10^{-3}
60cm	0.9892	1.64×10^{-3}	0.9916	1.64×10^{-3}	0.9944	1.63×10^{-3}	0.9973	1.60×10^{-3}
100cm	0.9903	1.50×10^{-3}	0.9926	1.54×10^{-3}	0.9950	1.55×10^{-3}	0.9977	1.55×10^{-3}
140cm	0.9910	1.33×10^{-3}	0.9930	1.37×10^{-3}	0.9953	1.39×10^{-3}	0.9978	1.40×10^{-3}
200cm	0.9917	1.11×10^{-3}	0.9935	1.15×10^{-3}	0.9956	1.19×10^{-3}	0.9978	1.21×10^{-3}
300cm	0.9924	8.63×10^{-4}	0.9940	9.07×10^{-4}	0.9958	9.39×10^{-4}	0.9977	9.55×10^{-4}
Long.	$\Phi = 205°W$		$\Phi = 215°W$		$\Phi = 225°W$		$\Phi = 235°W$	
l_R	R_{205}	σ_{205}	R_{215}	σ_{215}	R_{225}	σ_{225}	R_{235}	σ_{235}
5cm	0.9994	8.40×10^{-4}	1.0034	7.83×10^{-4}	1.0071	7.80×10^{-4}	1.0102	7.96×10^{-4}
10cm	0.9974	1.02×10^{-3}	1.0012	9.92×10^{-4}	1.0047	1.00×10^{-3}	1.0077	1.01×10^{-3}
15cm	0.9978	1.13×10^{-3}	1.0014	1.12×10^{-3}	1.0046	1.14×10^{-3}	1.0073	1.16×10^{-3}
20cm	0.9984	1.24×10^{-3}	1.0018	1.24×10^{-3}	1.0049	1.26×10^{-3}	1.0075	1.27×10^{-3}
30cm	0.9993	1.40×10^{-3}	1.0025	1.42×10^{-3}	1.0054	1.43×10^{-3}	1.0078	1.44×10^{-3}
60cm	1.0003	1.59×10^{-3}	1.0032	1.58×10^{-3}	1.0058	1.58×10^{-3}	1.0079	1.55×10^{-3}
100cm	1.0004	1.54×10^{-3}	1.0031	1.52×10^{-3}	1.0055	1.49×10^{-3}	1.0074	1.45×10^{-3}
140cm	1.0003	1.40×10^{-3}	1.0028	1.39×10^{-3}	1.0051	1.35×10^{-3}	1.0068	1.31×10^{-3}
200cm	1.0001	1.21×10^{-3}	1.0024	1.20×10^{-3}	1.0045	1.15×10^{-3}	1.0061	1.11×10^{-3}
300cm	0.9998	9.59×10^{-4}	1.0019	9.46×10^{-4}	1.0038	9.06×10^{-4}	1.0052	8.65×10^{-4}

TABLE 6.3c

Comparison of Seasonal Temperatures: Sub-earth Longitude Variations								
Long.	$\Phi = 245°W$		$\Phi = 255°W$		$\Phi = 265°W$		$\Phi = 275°W$	
l_R	R_{245}	σ_{245}	R_{255}	σ_{255}	R_{265}	σ_{265}	R_{275}	σ_{275}
5cm	1.0125	8.02×10^{-4}	1.0139	7.77×10^{-4}	1.0144	7.62×10^{-4}	1.0141	7.06×10^{-4}
10cm	1.0099	1.01×10^{-3}	1.0115	9.89×10^{-4}	1.0121	9.34×10^{-4}	1.0120	8.66×10^{-4}
15cm	1.0094	1.15×10^{-3}	1.0108	1.12×10^{-3}	1.0114	1.06×10^{-3}	1.0112	9.93×10^{-4}
20cm	1.0094	1.27×10^{-3}	1.0106	1.23×10^{-3}	1.0111	1.17×10^{-3}	1.0109	1.08×10^{-3}
30cm	1.0094	1.43×10^{-3}	1.0105	1.37×10^{-3}	1.0108	1.29×10^{-3}	1.0106	1.18×10^{-3}
60cm	1.0093	1.51×10^{-3}	1.0101	1.44×10^{-3}	1.0102	1.33×10^{-3}	1.0100	1.22×10^{-3}
100cm	1.0086	1.38×10^{-3}	1.0093	1.31×10^{-3}	1.0094	1.21×10^{-3}	1.0091	1.08×10^{-3}
140cm	1.0080	1.24×10^{-3}	1.0086	1.15×10^{-3}	1.0086	1.05×10^{-3}	1.0084	9.47×10^{-4}
200cm	1.0071	1.05×10^{-3}	1.0077	9.73×10^{-4}	1.0077	8.83×10^{-4}	1.0075	7.91×10^{-4}
300cm	1.0061	8.13×10^{-4}	1.0066	7.48×10^{-4}	1.0067	6.88×10^{-4}	1.0066	6.04×10^{-4}
Long.	$\Phi = 285°W$		$\Phi = 295°W$		$\Phi = 305°W$		$\Phi = 315°W$	
l_R	R_{285}	σ_{285}	R_{295}	σ_{295}	R_{305}	σ_{305}	R_{315}	σ_{315}
5cm	1.0131	6.75×10^{-4}	1.0118	6.53×10^{-4}	1.0104	6.21×10^{-4}	1.0093	6.00×10^{-4}
10cm	1.0113	7.99×10^{-4}	1.0103	7.38×10^{-4}	1.0091	6.82×10^{-4}	1.0081	6.53×10^{-4}
15cm	1.0107	8.97×10^{-4}	1.0098	8.05×10^{-4}	1.0089	7.44×10^{-4}	1.0081	6.87×10^{-4}
20cm	1.0104	9.78×10^{-4}	1.0097	8.84×10^{-4}	1.0089	7.91×10^{-4}	1.0082	7.25×10^{-4}
30cm	1.0101	1.08×10^{-3}	1.0095	9.72×10^{-4}	1.0089	8.81×10^{-4}	1.0084	8.14×10^{-4}
60cm	1.0095	1.10×10^{-3}	1.0091	9.96×10^{-4}	1.0087	9.17×10^{-4}	1.0085	8.54×10^{-4}
100cm	1.0087	9.83×10^{-4}	1.0084	8.92×10^{-4}	1.0081	8.22×10^{-4}	1.0081	8.13×10^{-4}
140cm	1.0080	8.63×10^{-4}	1.0077	7.89×10^{-4}	1.0076	7.32×10^{-4}	1.0076	7.22×10^{-4}
200cm	1.0072	7.14×10^{-4}	1.0070	6.46×10^{-4}	1.0069	6.14×10^{-4}	1.0070	6.04×10^{-4}
300cm	1.0063	5.53×10^{-4}	1.0062	4.84×10^{-4}	1.0062	4.67×10^{-4}	1.0063	4.76×10^{-4}
Long.	$\Phi = 325°W$		$\Phi = 335°W$		$\Phi = 345°W$		$\Phi = 355°W$	
l_R	R_{325}	σ_{325}	R_{335}	σ_{335}	R_{345}	σ_{345}	R_{355}	σ_{355}
5cm	1.0087	6.06×10^{-4}	1.0086	5.86×10^{-4}	1.0091	5.63×10^{-4}	1.0100	5.10×10^{-4}
10cm	1.0075	6.17×10^{-4}	1.0072	6.12×10^{-4}	1.0075	6.22×10^{-4}	1.0081	6.01×10^{-4}
15cm	1.0076	6.49×10^{-4}	1.0074	6.37×10^{-4}	1.0076	6.46×10^{-4}	1.0082	6.65×10^{-4}
20cm	1.0078	6.85×10^{-4}	1.0078	6.78×10^{-4}	1.0080	6.93×10^{-4}	1.0085	7.23×10^{-4}
30cm	1.0082	7.68×10^{-4}	1.0083	7.72×10^{-4}	1.0086	7.86×10^{-4}	1.0090	8.07×10^{-4}
60cm	1.0085	8.36×10^{-4}	1.0088	8.43×10^{-4}	1.0091	8.59×10^{-4}	1.0095	8.75×10^{-4}
100cm	1.0082	7.87×10^{-4}	1.0086	8.03×10^{-4}	1.0090	8.05×10^{-4}	1.0093	8.20×10^{-4}
140cm	1.0078	7.26×10^{-4}	1.0082	7.30×10^{-4}	1.0086	7.24×10^{-4}	1.0089	7.37×10^{-4}
200cm	1.0073	6.25×10^{-4}	1.0076	6.27×10^{-4}	1.0080	6.29×10^{-4}	1.0083	6.15×10^{-4}
300cm	1.0066	4.89×10^{-4}	1.0070	5.01×10^{-4}	1.0073	4.81×10^{-4}	1.0076	4.64×10^{-4}

small for a sub-earth latitude of 0°N. Therefore, these areas will have smaller weights when averaged to obtain the whole-disk brightness temperature and should present no problems for small sub-earth latitudes.

6.4 Variation with Time of Day

As stated earlier the sub-earth time of day is also an important factor in determining the whole-disk brightness temperature at the shorter wavelengths. Short, in this instance, means wavelengths of about 4cm or less. For wavelengths longer than this cutoff, the contribution from the part of the sub-surface involved with diurnal variations is minor compared to the rest of the contributing sub-surface. So far I have been keeping this parameter at 12:00 hours. Table 6.4 illustrates the daily brightness temperature variations if this parameter is allowed to vary. Only those time of days that can be observed from Earth are listed. All ten cases of radio absorption lengths are tabulated. These are for the nominal case with a sub-earth longitude of 75°W and a dielectric constant of 2.2. As was done in the previous sections, the variation of the ratios R over the season was used to estimate a standard deviation. As can easily be seen from the table of standard deviations, these ratios do not vary much during the year. Note the very small ratios at the long radio absorption lengths. Even at the shorter radio absorption lengths the changes are not very large.

As with the case of radio absorption length variations over the Martian year, the variations here are not simple enough to allow an easy parametrization of the changes in brightness temperature. In addition, it is impossible to see the nightside of Mars with Earth based observations. The largest phase angle for the Earth-Sun-Mars system is less than 50°, which implies that earth-based observations can cover the range from 9:00 hours to 15:00 hours in sub-earth time of day. For a wavelength

TABLE 6.4

Comparison of Seasonal Temperatures: Sub-earth Time-of-day						
Time	9:20h		10:00h		10:40h	
l_R	R_{-4}	σ_{-4}	R_{-3}	σ_{-3}	R_{-2}	σ_{-2}
5 cm	0.9566	2.74×10^{-3}	0.9691	1.86×10^{-3}	0.9809	1.09×10^{-3}
10 cm	0.9716	1.99×10^{-3}	0.9796	1.37×10^{-3}	0.9872	8.18×10^{-4}
15 cm	0.9790	1.53×10^{-3}	0.9848	1.05×10^{-3}	0.9905	6.38×10^{-4}
20 cm	0.9833	1.25×10^{-3}	0.9879	8.71×10^{-4}	0.9924	5.28×10^{-4}
30 cm	0.9882	9.15×10^{-4}	0.9914	6.42×10^{-4}	0.9946	3.83×10^{-4}
60 cm	0.9937	5.36×10^{-4}	0.9954	3.74×10^{-4}	0.9971	2.23×10^{-4}
100cm	0.9961	3.60×10^{-4}	0.9972	2.57×10^{-4}	0.9982	1.57×10^{-4}
140cm	0.9972	2.54×10^{-4}	0.9980	1.77×10^{-4}	0.9987	1.20×10^{-4}
200cm	0.9980	1.53×10^{-4}	0.9986	1.46×10^{-4}	0.9991	1.29×10^{-4}
300cm	0.9987	1.51×10^{-4}	0.9990	8.33×10^{-5}	0.9994	1.49×10^{-4}
Time	11:20h		12:00h		12:40h	
l_R	R_{-1}	σ_{-1}	R_0	σ_0	R_1	σ_1
5 cm	0.9913	4.56×10^{-4}	1.0000	0.00×10^{-0}	1.0064	2.66×10^{-4}
10 cm	0.9942	3.64×10^{-4}	1.0000	0.00×10^{-0}	1.0045	2.08×10^{-4}
15 cm	0.9956	2.89×10^{-4}	1.0000	0.00×10^{-0}	1.0035	2.35×10^{-4}
20 cm	0.9965	2.19×10^{-4}	1.0000	0.00×10^{-0}	1.0028	1.93×10^{-4}
30 cm	0.9975	1.55×10^{-4}	1.0000	0.00×10^{-0}	1.0020	1.29×10^{-4}
60 cm	0.9986	1.23×10^{-4}	1.0000	0.00×10^{-0}	1.0011	1.24×10^{-4}
100cm	0.9992	9.75×10^{-5}	1.0000	0.00×10^{-0}	1.0007	3.81×10^{-5}
140cm	0.9994	7.52×10^{-5}	1.0000	0.00×10^{-0}	1.0005	7.83×10^{-5}
200cm	0.9996	6.53×10^{-5}	1.0000	0.00×10^{-0}	1.0003	4.93×10^{-5}
300cm	0.9997	1.08×10^{-4}	1.0000	0.00×10^{-0}	1.0002	6.82×10^{-5}
Time	13:20h		14:00h		14:40h	
l_R	R_2	σ_2	R_3	σ_3	R_4	σ_4
5 cm	1.0103	3.63×10^{-4}	1.0117	3.25×10^{-4}	1.0120	1.41×10^{-3}
10 cm	1.0075	3.13×10^{-4}	1.0089	3.09×10^{-4}	1.0093	1.62×10^{-3}
15 cm	1.0058	2.83×10^{-4}	1.0070	2.94×10^{-4}	1.0075	1.57×10^{-3}
20 cm	1.0047	2.59×10^{-4}	1.0058	2.67×10^{-4}	1.0062	1.48×10^{-3}
30 cm	1.0035	1.69×10^{-4}	1.0043	2.48×10^{-4}	1.0046	1.36×10^{-3}
60 cm	1.0019	8.52×10^{-5}	1.0024	1.91×10^{-4}	1.0027	1.14×10^{-3}
100cm	1.0012	1.22×10^{-4}	1.0015	1.32×10^{-4}	1.0017	9.88×10^{-4}
140cm	1.0009	1.38×10^{-4}	1.0011	1.15×10^{-5}	1.0013	8.87×10^{-4}
200cm	1.0006	7.01×10^{-5}	1.0008	7.27×10^{-4}	1.0010	8.01×10^{-4}
300cm	1.0004	1.82×10^{-4}	1.0005	3.15×10^{-4}	1.0007	7.00×10^{-4}

of 2cm (radio absorption length of 30cm) the variation of the whole-disk brightness over this range is about 5 degrees. For a wavelength of 6cm (radio absorption length of 90cm) the variation is slightly more than 1 degree over this range of sub-earth time of day. This means that the assumption that the whole-disk brightness does not change as phase angle changes implies an error of about 2 percent at 2cm. Of course, as the wavelength used becomes shorter, the error inherent in this assumption rises rapidly.

6.5 Variation with Sub-earth Latitude

Another important factor in determining the whole-disk brightness is the sub-earth latitude. Indeed, for certain seasons it is the geometric parameter with the largest effect on the brightness temperature. Figure 6.8 illustrates the difference, for all seasons, in brightness temperatures that are obtained at the two extremes of the sub-earth latitude. As can be seen, for certain seasons the difference between the two extremes is as large as 25K for a radio absorption length of 30cm. Admittedly, this extreme case is never visible from Earth. Because of the geometry, many of the combinations of season and sub-earth latitude are not observable or are observable only rarely. Unfortunately, it is not easy to parametrize which latitudes can be seen at which seasons. In addition, because the whole-disk brightness temperature does not behave in a similar manner as a function of sub-earth latitude at different radio absorption lengths it is very difficult to find a way to present all the variations. The cases shown are for a dielectric constant of 2.2, but as was seen in a previous section, the dielectric constant is only a scaling factor. As with previous illustrative cases, this one also uses the nominal model values for the sub-earth longitude of 75°W. and noon for the sub-earth time of day.

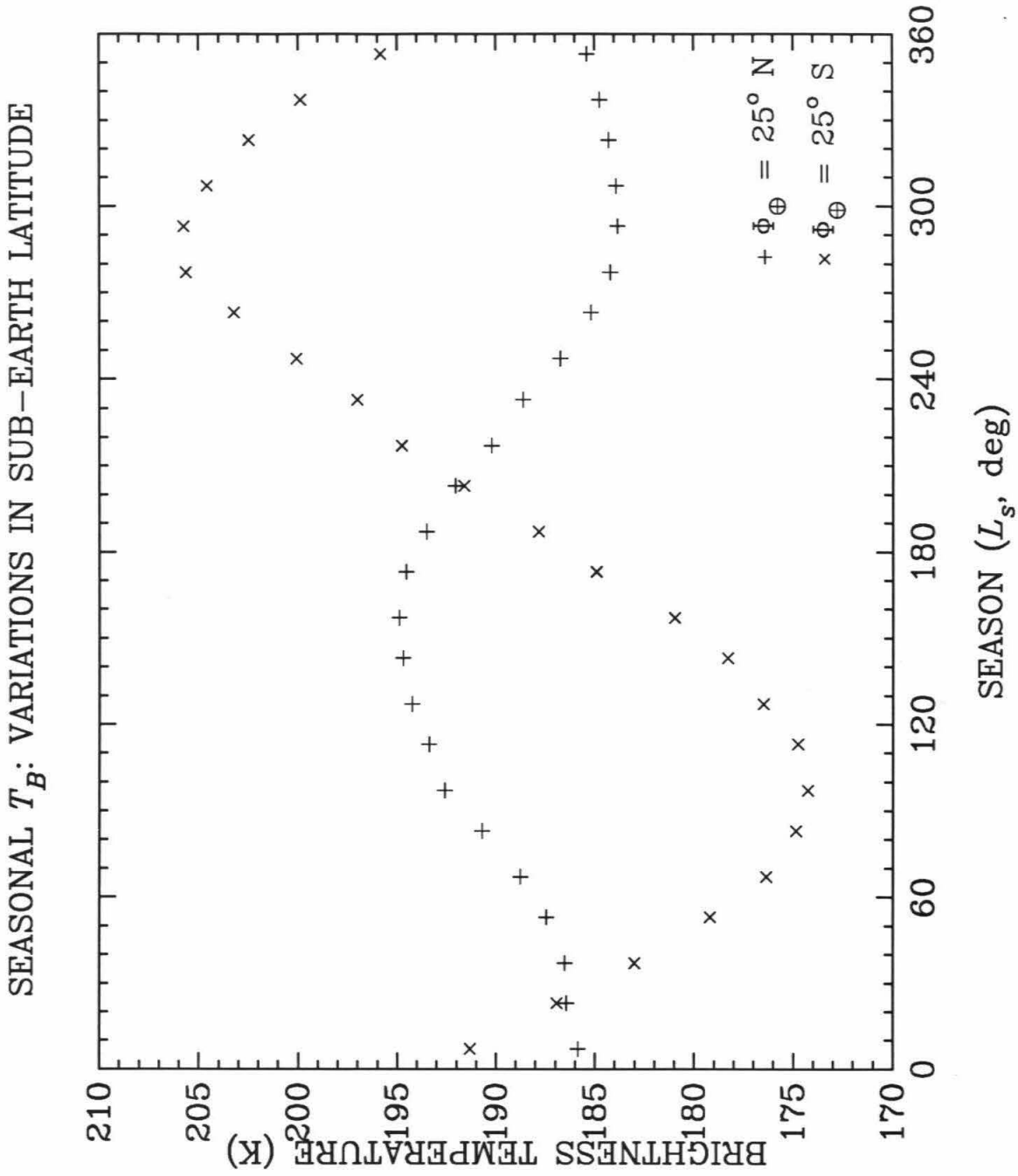

FIGURE 6.6: The variation of brightness temperature as a function of the season for two different sub-earth latitudes. The crosses are the result for a sub-earth latitude of 25°N and the x's are for a sub-earth latitude of 25°S. Both curves are for a sub-earth longitude of 75°W and are calculated from models having a dielectric constant of 2.2 and a radio absorption length of 30cm

Tables 6.5a-f (at the end of this chapter) list the temperature variations as a function of season and radio absorption length for seven different sub-earth latitudes. The variation in brightness temperature across latitudes is a smooth function, as can be seen by looking at the tables. Note that Table 6.5d is the same as the nominal model. As the sub-earth latitude is varied, more and more of one pole or the other is exposed, yielding a warmer or colder brightness temperature, depending upon whether it is the summer or winter pole being brought into sight. An additional factor that adds to the variation is the north-south asymmetry in the thermal parameters.

The reader should once more be reminded that Palluconi and Keiffer (1981) did not determine these thermal parameters above 60°N nor below 60°S. The albedo of the rock surface and the thermal inertia of the surface and, by extension, the sub-surface, were determined by doing an average over all longitudes of the values for these parameters for the latitude adjacent to these cutoffs. Therefore, of all the effects mentioned in this chapter, the sub-earth latitude is not only the most important geometric parameter, it is also the one with the largest amount of error inherent in the model. Included in this error is the unknown variability of the albedo of the CO_2 frost and the exact recession curve of the CO_2. Recall from previous chapters that the edge of the polar caps was not as well-determined as could be hoped for.

6.6 Discussion

It should be abundantly clear that some of the parameters that go into determining the whole-disk brightness temperature of Mars are extremely important if Mars is to be used as a calibrator at, or below, the 5% level. Of the geometric parameters, the most important is the sub-earth latitude. By assuming the sub-earth latitude is 0°N when in actuality it is not, can lead to errors on the order of 5% alone. The least

important geometric parameter is the sub-earth longitude. Unlike the north-south asymmetry, the east-west asymmetry in the thermal inertia and albedo is weaker and this appears as a smaller variation in the whole-disk brightness temperature. The phase angle (equivalently, the sub-earth time of day) is not as important a parameter as sub-earth latitude, but this is mainly because earth-based observers do not sample the entire phase curve.

The electrical parameters also play a very important role in determining the whole-disk brightness temperature. Unlike the purely geometric parameters, however, they are not easily determined. From the measurements presented in Chapters 4 and 5, a good estimate of the radio absorption length is 30cm at a wavelength of 2cm and 90cm at a wavelength of 6cm. Since this estimate was made assuming that the radio absorption length scaled as the wavelength, a good estimate of the radio absorption length at any wavelength is 15λ. Using this scaling factor allows the radio absorption length to be determined for any wavelength. Since this scaling factor is unlikely to be in error by more than 10%, and since changing the radio absorption length by this much does not affect the whole-disk brightness temperature by a large amount, this is a very robust parameter.

Unfortunately, this can not be said about the dielectric constant. A realistic estimate of the error in the dielectric constant does change the whole-disk brightness temperature by a significant amount. In addition, the variations in dielectric constant over the surface of the planet are large enough that they may contribute to variations of the brightness temperature with differing geometries, like the variations in thermal inertia do. Hopefully, future observations will cause the errors in estimating the dielectric constant to go down. Until then, one should carefully consider all the variables when using Mars as a source of calibration. As of the present, although not nearly enough cases have been tested, the use of these charts to estimate the

whole-disk brightness temperature for a given observation appears to be less than five degrees except for possible pathological cases.

TABLE 6.5a

Sub-earth Latitude Variations: 25°N								
l_R	L_S=8°	L_S =23°	L_S=37°	L_S=53°	L_S=69°	L_S=82°	L_S=98°	L_S=112°
5cm	192.9	193.6	193.2	194.3	195.8	198.4	200.4	201.4
10cm	189.0	189.7	189.5	190.6	192.1	194.5	196.4	197.4
15cm	187.4	188.1	188.0	189.1	190.5	192.8	194.7	195.6
20cm	186.6	187.3	187.2	188.3	189.7	191.8	193.7	194.6
30cm	185.9	186.4	186.5	187.5	188.8	190.7	192.6	193.4
60cm	185.6	186.1	186.2	186.9	188.0	189.5	191.2	192.0
100cm	186.2	186.5	186.6	187.1	188.0	189.2	190.6	191.4
140cm	186.9	187.1	187.2	187.6	188.3	189.3	190.5	191.2
200cm	187.6	187.8	187.8	188.1	188.7	189.4	190.4	191.0
300cm	187.2	187.3	187.3	187.5	187.9	188.4	189.2	189.7
l_R	L_S=129°	L_S=141°	L_S=157°	L_S=174°	L_S=188°	L_S=203°	L_S=219°	L_S=232°
5cm	202.8	203.5	203.9	203.4	201.8	199.6	196.9	194.5
10cm	198.5	199.1	199.4	198.9	197.4	195.5	193.0	190.9
15cm	196.6	197.1	197.4	196.9	195.6	193.8	191.6	189.6
20cm	195.5	196.0	196.2	195.8	194.6	192.9	190.9	189.1
30cm	194.3	194.7	194.9	194.6	193.5	192.1	190.2	188.6
60cm	192.8	193.1	193.4	193.1	192.4	191.3	189.9	188.7
100cm	192.1	192.4	192.6	192.5	192.0	191.2	190.1	189.1
140cm	191.8	192.1	192.4	192.3	191.9	191.3	190.4	189.6
200cm	191.6	191.9	192.1	192.0	191.8	191.3	190.6	190.0
300cm	190.1	190.4	190.5	190.6	190.4	190.0	189.5	189.1
l_R	L_S=248°	L_S=264°	L_S=280°	L_S=293°	L_S=308°	L_S=323°	L_S=337°	L_S=353°
5cm	191.8	189.9	189.0	189.0	189.6	190.6	191.3	192.5
10cm	188.6	186.8	185.8	185.7	186.1	186.9	187.5	188.5
15cm	187.4	185.7	184.7	184.5	184.8	185.5	186.0	186.9
20cm	187.0	185.3	184.3	184.1	184.3	184.8	185.3	186.1
30cm	186.8	185.2	184.2	183.9	183.9	184.3	184.8	185.4
60cm	187.2	185.9	185.0	184.6	184.4	184.6	184.9	185.3
100cm	188.0	186.9	186.1	185.7	185.5	185.5	185.8	186.0
140cm	188.6	187.7	187.0	186.6	186.4	186.3	186.6	186.7
200cm	189.2	188.5	187.9	187.5	187.3	187.2	187.5	187.5
300cm	188.5	187.9	187.5	187.2	187.0	186.9	187.2	187.1

TABLE 6.5b

Sub-earth Latitude Variations: 15°N								
l_R	L_S=8°	L_S =23°	L_S=37°	L_S=53°	L_S=69°	L_S=82°	L_S=98°	L_S=112°
5cm	196.1	195.6	194.3	194.1	194.3	195.6	196.9	198.2
10cm	192.0	191.6	190.5	190.4	190.7	191.9	193.1	194.1
15cm	190.4	190.0	189.1	189.0	189.3	190.4	191.5	192.4
20cm	189.6	189.2	188.4	188.3	188.6	189.6	190.6	191.5
30cm	188.8	188.5	187.8	187.7	187.9	188.8	189.8	190.6
60cm	188.5	188.3	187.8	187.6	187.8	188.4	189.2	189.8
100cm	188.9	188.7	188.3	188.1	188.3	188.7	189.4	189.8
140cm	189.4	189.2	188.9	188.7	188.8	189.1	189.7	190.1
200cm	189.9	189.7	189.5	189.3	189.3	189.6	190.0	190.3
300cm	189.1	189.0	188.8	188.6	188.7	188.8	189.1	189.4
l_R	L_S=129°	L_S=141°	L_S=157°	L_S=174°	L_S=188°	L_S=203°	L_S=219°	L_S=232°
5cm	200.2	201.6	203.1	204.3	204.2	203.5	202.1	200.5
10cm	195.8	197.0	198.3	199.3	199.2	198.7	197.5	196.2
15cm	193.9	195.0	196.2	197.1	197.1	196.7	195.6	194.4
20cm	192.8	193.9	194.9	195.9	195.8	195.5	194.6	193.5
30cm	191.7	192.6	193.6	194.4	194.4	194.2	193.4	192.6
60cm	190.6	191.3	192.1	192.7	192.8	192.7	192.3	191.7
100cm	190.5	191.0	191.6	192.1	192.2	192.2	191.8	191.4
140cm	190.6	191.0	191.5	191.9	192.0	192.0	191.8	191.5
200cm	190.8	191.1	191.4	191.8	191.9	191.9	191.7	191.5
300cm	189.7	189.9	190.2	190.5	190.6	190.6	190.4	190.3
l_R	L_S=248°	L_S=264°	L_S=280°	L_S=293°	L_S=308°	L_S=323°	L_S=337°	L_S=353°
5cm	198.6	197.1	196.2	196.0	196.2	196.6	196.6	196.7
10cm	194.6	193.2	192.3	192.0	192.1	192.4	192.4	192.4
15cm	193.0	191.7	190.8	190.5	190.5	190.7	190.7	190.7
20cm	192.2	191.0	190.2	189.8	189.8	189.9	189.9	189.9
30cm	191.5	190.4	189.6	189.3	189.1	189.1	189.1	189.1
60cm	190.9	190.1	189.5	189.1	188.9	188.8	188.9	188.8
100cm	190.9	190.3	189.8	189.5	189.3	189.2	189.3	189.1
140cm	191.0	190.5	190.1	189.9	189.7	189.6	189.7	189.6
200cm	191.1	190.8	190.4	190.2	190.1	189.9	190.1	190.0
300cm	190.0	189.7	189.5	189.3	189.2	189.1	189.3	189.2

TABLE 6.5c

Sub-earth Latitude Variations: 5°N								
l_R	L_S=8°	L_S =23°	L_S=37°	L_S=53°	L_S=69°	L_S=82°	L_S=98°	L_S=112°
5cm	198.2	196.4	194.1	192.6	191.7	191.9	192.6	194.0
10cm	194.0	192.4	190.4	189.1	188.3	188.4	189.0	190.1
15cm	192.4	190.9	189.1	187.8	187.1	187.1	187.6	188.6
20cm	191.6	190.2	188.5	187.3	186.5	186.6	187.0	187.8
30cm	190.9	189.6	188.1	186.9	186.2	186.2	186.5	187.1
60cm	190.7	189.7	188.5	187.4	186.8	186.6	186.7	187.1
100cm	191.0	190.2	189.3	188.4	187.8	187.5	187.5	187.7
140cm	191.4	190.7	189.9	189.1	188.6	188.4	188.3	188.4
200cm	191.6	191.1	190.5	189.9	189.4	189.2	189.1	189.2
300cm	190.5	190.2	189.7	189.3	188.9	188.7	188.6	188.6
l_R	L_S=129°	L_S=141°	L_S=157°	L_S=174°	L_S=188°	L_S=203°	L_S=219°	L_S=232°
5cm	196.6	198.6	201.1	203.8	205.0	205.9	206.0	205.2
10cm	192.3	194.0	196.2	198.6	199.7	200.6	200.8	200.3
15cm	190.4	192.0	194.0	196.3	197.3	198.3	198.5	198.2
20cm	189.5	190.9	192.8	194.9	195.9	196.9	197.2	197.0
30cm	188.5	189.8	191.4	193.3	194.3	195.3	195.6	195.6
60cm	188.0	188.9	190.0	191.5	192.4	193.2	193.6	193.8
100cm	188.3	188.9	189.8	190.9	191.6	192.3	192.7	192.9
140cm	188.9	189.3	190.0	190.9	191.4	192.0	192.4	192.6
200cm	189.4	189.8	190.3	190.9	191.4	191.9	192.1	192.3
300cm	188.8	189.1	189.4	189.9	190.2	190.5	190.7	190.9
l_R	L_S=248°	L_S=264°	L_S=280°	L_S=293°	L_S=308°	L_S=323°	L_S=337°	L_S=353°
5cm	204.6	203.8	203.0	202.6	202.3	201.9	201.1	200.0
10cm	199.8	199.2	198.5	198.0	197.7	197.3	196.6	195.6
15cm	197.8	197.3	196.6	196.2	195.8	195.4	194.8	193.8
20cm	196.7	196.3	195.7	195.3	194.9	194.4	193.9	192.9
30cm	195.4	195.1	194.7	194.3	193.9	193.5	193.0	192.1
60cm	193.8	193.7	193.5	193.3	193.0	192.7	192.4	191.6
100cm	193.0	193.0	192.9	192.8	192.7	192.4	192.3	191.7
140cm	192.7	192.8	192.7	192.6	192.5	192.4	192.3	191.9
200cm	192.4	192.5	192.5	192.5	192.4	192.3	192.3	192.0
300cm	190.9	191.0	191.0	191.0	191.0	190.9	191.1	190.8

TABLE 6.5d

Sub-earth Latitude Variations: 0°N								
l_R	L_S=8°	L_S =23°	L_S=37°	L_S=53°	L_S=69°	L_S=82°	L_S=98°	L_S=112°
5cm	198.7	196.2	193.4	191.3	189.9	189.7	190.2	191.7
10cm	194.6	192.3	189.8	187.9	186.7	186.4	186.8	187.9
15cm	193.0	190.9	188.6	186.8	185.6	185.2	185.5	186.5
20cm	192.2	190.3	188.1	186.4	185.1	184.8	184.9	185.8
30cm	191.6	189.8	187.9	186.2	185.0	184.6	184.6	185.2
60cm	191.5	190.1	188.5	187.0	185.9	185.4	185.2	185.5
100cm	191.8	190.7	189.4	188.2	187.2	186.7	186.4	186.5
140cm	192.1	191.1	190.1	189.1	188.2	187.7	187.4	187.4
200cm	192.2	191.5	190.7	189.9	189.1	188.7	188.4	188.4
300cm	191.0	190.5	189.9	189.3	188.8	188.4	188.2	188.1
l_R	L_S=129°	L_S=141°	L_S=157°	L_S=174°	L_S=188°	L_S=203°	L_S=219°	L_S=232°
5cm	194.4	196.7	199.6	203.0	204.9	206.5	207.3	207.0
10cm	190.2	192.2	194.7	197.8	199.4	201.1	201.9	201.8
15cm	188.5	190.3	192.6	195.4	197.0	198.6	199.4	199.5
20cm	187.6	189.2	191.4	194.0	195.6	197.1	198.0	198.2
30cm	186.8	188.1	190.0	192.4	193.9	195.4	196.2	196.6
60cm	186.4	187.4	188.8	190.6	191.8	193.1	193.9	194.4
100cm	187.1	187.7	188.7	190.1	191.0	192.1	192.8	193.2
140cm	187.8	188.3	189.1	190.1	190.9	191.7	192.4	192.8
200cm	188.6	189.0	189.5	190.3	190.9	191.6	192.1	192.4
300cm	188.2	188.4	188.8	189.3	189.8	190.3	190.6	190.9
l_R	L_S=248°	L_S=264°	L_S=280°	L_S=293°	L_S=308°	L_S=323°	L_S=337°	L_S=353°
5cm	207.0	206.8	206.1	205.6	205.0	204.2	203.0	201.2
10cm	201.9	201.9	201.4	200.9	200.2	199.4	198.4	196.7
15cm	199.7	199.8	199.4	198.9	198.3	197.5	196.5	195.0
20cm	198.5	198.6	198.3	197.8	197.2	196.5	195.6	194.1
30cm	197.0	197.2	197.0	196.7	196.1	195.5	194.6	193.3
60cm	194.9	195.2	195.3	195.2	194.9	194.4	193.8	192.8
100cm	193.7	194.1	194.3	194.3	194.1	193.8	193.6	192.8
140cm	193.2	193.6	193.8	193.8	193.8	193.6	193.4	192.8
200cm	192.8	193.1	193.3	193.4	193.4	193.2	193.2	192.8
300cm	191.2	191.4	191.6	191.7	191.7	191.6	191.8	191.5

TABLE 6.5e

Sub-earth Latitude Variations: 5°S								
l_R	L_S=8°	L_S =23°	L_S=37°	L_S=53°	L_S=69°	L_S=82°	L_S=98°	L_S=112°
5cm	196.1	190.4	185.5	181.1	178.0	176.7	176.9	178.4
10cm	192.7	187.5	183.0	178.8	175.9	174.6	174.5	175.7
15cm	191.6	186.7	182.4	178.4	175.5	174.1	173.9	174.8
20cm	191.3	186.6	182.4	178.5	175.6	174.2	173.8	174.6
30cm	191.3	186.9	183.0	179.2	176.4	174.9	174.3	174.8
60cm	192.0	188.4	185.1	181.8	179.1	177.5	176.6	176.6
100cm	192.6	189.8	187.1	184.2	181.9	180.4	179.3	179.1
140cm	192.8	190.5	188.3	185.9	183.8	182.5	181.4	181.0
200cm	192.8	191.1	189.3	187.3	185.6	184.5	183.5	183.1
300cm	191.4	190.2	188.9	187.4	186.1	185.2	184.4	184.0
l_R	L_S=129°	L_S=141°	L_S=157°	L_S=174°	L_S=188°	L_S=203°	L_S=219°	L_S=232°
5cm	181.7	184.6	188.8	194.6	198.6	203.3	207.6	209.4
10cm	178.5	181.0	184.7	189.9	193.4	197.9	201.7	203.8
15cm	177.3	179.6	182.9	187.7	191.0	195.3	198.9	201.1
20cm	176.8	178.9	181.9	186.4	189.6	193.7	197.1	199.3
30cm	176.5	178.3	181.0	184.9	187.9	191.6	194.8	197.0
60cm	177.5	178.7	180.6	183.5	185.8	188.8	191.4	193.5
100cm	179.5	180.2	181.5	183.6	185.4	187.7	189.8	191.5
140cm	181.2	181.7	182.7	184.3	185.7	187.5	189.3	190.7
200cm	183.1	183.4	184.1	185.2	186.3	187.7	189.0	190.2
300cm	183.9	184.0	184.4	185.2	185.9	186.9	187.9	188.8
l_R	L_S=248°	L_S=264°	L_S=280°	L_S=293°	L_S=308°	L_S=323°	L_S=337°	L_S=353°
5cm	213.2	216.6	218.5	217.4	215.0	211.7	207.8	202.1
10cm	207.3	210.7	212.8	212.0	209.9	206.9	203.4	198.2
15cm	204.4	207.8	210.0	209.5	207.6	204.9	201.7	196.9
20cm	202.6	205.9	208.2	207.9	206.3	203.8	200.8	196.3
30cm	200.1	203.3	205.7	205.8	204.6	202.5	199.9	195.8
60cm	196.1	198.9	201.2	201.9	201.5	200.2	198.5	195.5
100cm	193.7	196.0	198.0	198.9	199.0	198.3	197.3	195.2
140cm	192.5	194.5	196.3	197.1	197.4	197.0	196.4	194.8
200cm	191.6	193.2	194.7	195.4	195.8	195.7	195.5	194.3
300cm	189.9	191.0	192.2	192.8	193.2	193.2	193.2	192.5

TABLE 6.5f

Sub-earth Latitude Variations: 15°S								
l_R	L_S=8°	L_S =23°	L_S=37°	L_S=53°	L_S=69°	L_S=82°	L_S=98°	L_S=112°
5cm	198.1	193.6	189.5	185.8	183.2	182.1	182.4	183.9
10cm	194.3	190.2	186.4	183.0	180.5	179.4	179.5	180.7
15cm	193.0	189.1	185.6	182.3	179.9	178.7	178.6	179.6
20cm	192.4	188.8	185.4	182.2	179.8	178.6	178.4	179.2
30cm	192.2	188.8	185.6	182.5	180.2	178.9	178.5	179.1
60cm	192.4	189.7	187.1	184.4	182.2	180.9	180.2	180.3
100cm	192.8	190.7	188.6	186.3	184.4	183.2	182.4	182.2
140cm	193.0	191.3	189.5	187.6	186.0	184.9	184.1	183.8
200cm	193.1	191.7	190.3	188.8	187.4	186.5	185.7	185.4
300cm	191.7	190.7	189.7	188.6	187.5	186.8	186.1	185.9
l_R	L_S=129°	L_S=141°	L_S=157°	L_S=174°	L_S=188°	L_S=203°	L_S=219°	L_S=232°
5cm	187.1	189.9	193.7	198.7	202.0	205.7	208.7	209.7
10cm	183.4	185.8	189.2	193.6	196.6	200.1	202.8	204.1
15cm	182.0	184.1	187.2	191.4	194.1	197.5	200.1	201.5
20cm	181.3	183.3	186.1	190.0	192.7	195.9	198.4	199.8
30cm	180.8	182.5	185.0	188.4	190.9	193.9	196.2	197.8
60cm	181.3	182.4	184.2	186.7	188.7	191.1	193.2	194.6
100cm	182.7	183.5	184.7	186.6	188.1	189.9	191.6	192.8
140cm	184.1	184.6	185.5	186.9	188.1	189.7	191.0	192.1
200cm	185.5	185.9	186.5	187.5	188.5	189.6	190.7	191.6
300cm	185.8	186.0	186.4	187.1	187.8	188.6	189.4	190.0
l_R	L_S=248°	L_S=264°	L_S=280°	L_S=293°	L_S=308°	L_S=323°	L_S=337°	L_S=353°
5cm	211.9	213.7	214.4	213.5	211.9	209.6	206.9	202.8
10cm	206.2	208.1	208.9	208.2	206.7	204.7	202.2	198.5
15cm	203.5	205.4	206.4	205.9	204.6	202.6	200.4	196.9
20cm	201.9	203.8	204.9	204.5	203.3	201.5	199.4	196.1
30cm	199.7	201.6	202.8	202.7	201.8	200.3	198.4	195.5
60cm	196.4	198.2	199.5	199.8	199.4	198.5	197.2	195.1
100cm	194.4	195.9	197.1	197.6	197.6	197.1	196.3	194.8
140cm	193.4	194.7	195.8	196.3	196.4	196.1	195.7	194.6
200cm	192.6	193.7	194.6	195.1	195.3	195.2	195.0	194.2
300cm	190.8	191.6	192.4	192.8	193.0	192.9	193.0	192.5

TABLE 6.5g

Sub-earth Latitude Variations: 25°S								
l_R	L_S=8°	L_S =23°	L_S=37°	L_S=53°	L_S=69°	L_S=82°	L_S=98°	L_S=112°
5cm	198.9	195.7	192.4	189.7	187.9	187.3	187.7	189.2
10cm	194.8	191.9	189.0	186.5	184.8	184.2	184.4	185.6
15cm	193.3	190.6	187.9	185.5	183.9	183.2	183.3	184.3
20cm	192.6	190.0	187.5	185.2	183.5	182.8	182.8	183.7
30cm	192.1	189.7	187.4	185.2	183.6	182.8	182.6	183.3
60cm	192.1	190.2	188.2	186.3	184.9	184.0	183.6	183.8
100cm	192.4	190.9	189.4	187.8	186.4	185.7	185.1	185.2
140cm	192.6	191.4	190.1	188.8	187.6	186.9	186.4	186.3
200cm	192.7	191.8	190.8	189.7	188.7	188.1	187.6	187.5
300cm	191.4	190.8	190.0	189.2	188.5	188.0	187.6	187.4
l_R	L_S=129°	L_S=141°	L_S=157°	L_S=174°	L_S=188°	L_S=203°	L_S=219°	L_S=232°
5cm	192.1	194.6	197.9	201.9	204.3	206.6	208.2	208.3
10cm	188.1	190.2	193.1	196.6	198.8	201.1	202.6	202.9
15cm	186.4	188.3	191.0	194.3	196.3	198.6	200.0	200.5
20cm	185.6	187.4	189.8	192.9	194.9	197.0	198.4	199.1
30cm	184.9	186.4	188.5	191.3	193.1	195.2	196.6	197.3
60cm	184.8	185.9	187.4	189.5	191.0	192.7	193.9	194.7
100cm	185.7	186.4	187.5	189.0	190.2	191.6	192.6	193.3
140cm	186.7	187.2	188.0	189.2	190.1	191.2	192.1	192.8
200cm	187.7	188.0	188.6	189.5	190.2	191.1	191.8	192.3
300cm	187.5	187.7	188.1	188.7	189.2	189.8	190.4	190.8
l_R	L_S=248°	L_S=264°	L_S=280°	L_S=293°	L_S=308°	L_S=323°	L_S=337°	L_S=353°
5cm	209.1	209.4	209.1	208.5	207.6	206.3	204.6	202.1
10cm	203.7	204.2	204.1	203.5	202.6	201.4	199.9	197.6
15cm	201.4	202.0	201.9	201.4	200.6	199.4	198.0	195.9
20cm	199.9	200.6	200.7	200.2	199.4	198.4	197.1	195.0
30cm	198.2	198.9	199.1	198.9	198.2	197.3	196.1	194.3
60cm	195.7	196.5	196.9	196.9	196.5	195.9	195.2	193.8
100cm	194.2	194.9	195.4	195.6	195.4	195.1	194.7	193.6
140cm	193.5	194.2	194.7	194.8	194.8	194.6	194.4	193.6
200cm	192.9	193.5	193.9	194.1	194.2	194.0	194.0	193.4
300cm	191.2	191.7	192.0	192.2	192.3	192.2	192.3	191.9

CHAPTER 7
IMPLICATIONS FOR FUTURE RESEARCH

In this chapter I would like to discuss the implications of the present research and the directions for the most fruitful future research. The work presented in this thesis may inspire more questions than it answers. I will not debate whether this is a commendation or a condemnation. Rather, I will try to address the points I believe are the most interesting and will hopefully provide the most fertile grounds for further research.

This dissertation has taken radio science one more step along the path towards an understanding of the terrestrial planets. The work presented herein has yielded best estimates of two electrical parameters, dielectric constant and radio absorption length, for all latitudes between 60°N and 60°S. Each of these estimates is only for a limited range of longitudes, however. Hopefully future measurements will allow the complete mapping of these parameters. To do this will require better estimates of the thermal parameters for the sub-surface. It is obvious from the region of anomalously low brightness temperatures found in a band circling the globe between latitudes of roughly 10°S and 35°S that the current thermal parameters are not sufficient, in either time or space, to parametrize the sub-surface to the depth from which the observed radio waves originate.

This is obviously one of most intriguing possibilities for further research. It is difficult, but not impossible, to determine the make-up of the sub-surface from just surface temperature measurements. See Figure 5.8 for an example of the surface manifestation of sub-surface layering. In addition, it would be a useful study to go back to the Viking infrared data and investigate the possibility that the albedo in the anomalous region does vary during the year. Another path of research that also

originates in the anomalous region is the investigation of sub-surface volatiles such as water. Questions of how deep they would have to be in order not to be seen by the infrared data and how fast they would sublimate and what would be their atmospheric signature, immediately spring to mind.

In addition to the estimation of electrical parameters at the given latitudes, the polar regions were also investigated. Since the published maps of thermal inertia and albedo do not extend into these polar regions, an additional investigation reveals itself. That is to lower the standards used by Palluconi and Keiffer (1981) and go back to the Viking infrared data and attempt to get a 'best' estimate of these thermal parameters above 60°N and below 60°S. Or it may be possible, with additional radio measurements at different wavelengths, to estimate both the thermal and radio parameters using just the radio observations. Or inversely, assume the radio parameters are know by extrapolation from lower latitudes and estimate the thermal parameters from the current radio measurements. Either way, with these estimates of the thermal parameters, a few of the currently unanswerable questions may be addressed. For instance, currently it is impossible to know whether the brightness temperatures in these Polar regions are behaving as they should. From Figures 5.1 and 5.2 it seems that if the thermal parameters are near the average of those at lower latitudes, the South Polar Cold Region is colder than would be expected. With surface thermal parameters determined, the question of the effect of sub-surface volatiles could be addressed in much the same manner as suggested above for the anomalous region.

It would also be a worthwhile exercise to attempt to determine the thicknesses of the CO_2 frost caps and their advancement and recession rates. This would require the thermal inertia and albedo of the polar region. This ability would, in turn, allow the determination of the dielectric constant and radio absorption length for the polar regions. With these numbers in hand, and with more observations at different seasons,

it may be possible to determine the radio absorption length of CO_2.

It is also true that with more observations of Mars at different seasons at radio wavelengths, the thermal inertia and albedo could be determined by adding them as additional free parameters in the thermal modeling. This would require a revamping of the thermal model so that several cases with different thermal parameters could be run and the best fit thermal inertia and albedo could be estimated in addition to the electrical parameters. This is a rather ambitious project as it would require not only several more measurements, but good calibration for each of these observations. It is possible, since the whole-disk measurements are well behaved, to use these measurements to self-calibrate the data in a manner similar to the re-calibration used for the South data set. In this way a bootstrap process would be begun whereby any new Mars observations could be used to create better models which are then used to re-calibrate new data sets. Since the whole-disk measurements of polarization are dependent on the degree of polarization of the emitted radiation, rather than the emissivity of the surface, the two sets of measurements are not degenerate and this bootstrap process would, hopefully, settle down to ground truth rather than merely being self-consistent.

CHAPTER 8
BIBLIOGRAPHY

ANDREW, B.H., G.A. HARVEY, F.H. BRIGGS (1977). Rotational Variations in the Radio Brightness of Mars. *Astrophysical Journal* **213**, L131-L134; ERRATUM (1978). *Astrophysical Journal* **220**, L61

BAARS, J.W.M., R. GENTZEL, I.I.K. PAULINY-TOTH, A. WITZEL (1977). The Absolute Spectrum of Cas A; An Accurate Flux Density Scale and a Set of Secondary Calibrators. *Astronomy and Astrophysics* **61**, 99-106

BERGE, G.L., D.O. MUHLEMAN, G.S. ORTON (1972). High Resolution Interferometric Observations of Venus at Three Radio Wavelengths. *Icarus* **17**, 675-681

CAMPBELL, M.J., J. ULRICHS (1969). Electrical Properties of Rocks and Their Significance for Lunar Radar Observations. *Journal of Geophysical Research* **74**(25), 5867-5881

CHRISTENSEN, P.R. (1986) Surface Albedo Variations on Mars: Implications for Yearly Dust Deposition and Removal. (abstract) *MECA workshop on Dust on Mars II* (LPI Technical Report #86-09) 17-19

CUZZI, J.N., D.O. MUHLEMAN (1972). The Microwave Spectrum and Nature of the Sub-surface of Mars. *Icarus* **74**, 548-560

DOHERTY, L.H., B.H. ANDREW, F.H. BRIGGS (1979). Confirmation of the Longitudinal Dependence of the Radio Brightness of Mars. *Astrophysical Journal* **233**, L165-L168

DOWNS, G.S., R.M. GOLDSTEIN, R.R. GREEN, G.A. MORRIS, P.E. REICHLEY (1973). Martian Topography and Surface Properties as Seen by Radar: The 1971 Opposition. *Icarus* **18**, 8-21

DOWNS, G.S., P.E. REICHLEY, R.R. GREEN (1975). Radar Measurements of Martian Topography and Surface Properties: The 1971 and 1973 Oppositions. *Icarus* **26**, 273-312

EPSTEIN, E.E. (1971). Mars: A Possible Discrepancy between the Radio Spectrum and Elementary Theory. *Icarus* **14**, 214-221

EPSTEIN, E.E., B.H. ANDREW, F.H. BRIGGS, B.M. JAKOSKY, F.D. PALLUCONI (1983). Mars: Sub-surface Properties from Observed Longitudinal Variation of the 3.5-mm Brightness Temperature. *Icarus* **56**, 465-475

FOMALONT, E.B., M.C.H. WRIGHT (1974). Interferometry and Aperture Synthesis. In *Galactic and Extra-galactic Radio Astronomy.* (G.L. Verschuur and K.I. Kellerman, Ed.) pp.256-290, Springer-Verlag, N.Y.,N.Y.

FISCHBACHER, G.E., L.J. MARTIN, W.A. BAUM (1969). Martian Polar Cap Boundaries. *Final Report, Part A* (Planetary Research Center, Lowell Observatory, under contract 951547 to JPL)

GOLDEN, L.M. (1979). The Effect of Surface Roughness on the Transmission of Microwave Radiation through a Planetary Surface. *Icarus* **38**, 451-455

HÖGBOM, J.A. (1974). Aperture Synthesis with a Non-regular Distribution of Interferometer Baselines. *Astronomy and Astrophysics Supplement* **15** 417-426

HARMON, J.K., S.J. OSTRO (1985). Mars: Dual-Polarization Radar Observation

with Extended Coverage. *Icarus*, **62** 110-128

HAGFORS, T., J. MORIELLO (1965). The Effect of Roughness on the Polarization of Thermal Emission from a Surface. *Journal of Research of the National Bureau Standards, Radio Science*, **69D** 1614-1615

IWASAKI, K., S. YOSHIKAZU (1982). Martian North Polar Cap 1979-1980. *Journal of Geophysical Research* **87**(B12), 10,265-10,269

IWASAKI, K., S. YOSHIKAZU, T. AKABANE (1979). Behavior of the Martian North Polar Cap 1975-1978. *Journal of Geophysical Research* **84**(B14), 8311-8316

IWASAKI, K., S. YOSHIKAZU, T. AKABANE (1984). Martian North Polar Cap and Haze 1981-1982. *Publ. Astron. Soc. Japan* **36**, 347-356

JAKOSKY, B.M. (1979). The Effects of Non-ideal Surfaces on the Derived Thermal Properties of Mars. *Journal of Geophysical Research* **84**(B14), 8252-8262

JAKOSKY, B.M., P.R. CHRISTENSEN (1986). Global Duricrust on Mars: Analysis of Remote-Sensing Data. *Journal of Geophysical Research*, **91**(B3), 3547-3559

JAKOSKY, B.M., D.O. MUHLEMAN (1980). The Longitudinal Variation of the Thermal Inertia and of the 2.8 Centimeter Brightness Temperature of Mars *Astrophysical Journal* **239**, 403-409

JAKOSKY, B.M., D.O. MUHLEMAN (1981). A Comparison of the Thermal and Radar Characteristics of Mars. *Icarus* **45**, 25-38

JAMES P.B., G. BRIGGS, J. BARNES, A. SPRUCK (1979). Seasonal Recession of

Mars' South Polar Cap As Seen by Viking. *Journal of Geophysical Research* **84** (B6), 2889-2922

JAMES, P.B. (1979). Recession of Martian North Polar Cap: 1977-1978 Viking Observations. *Journal of Geophysical Research* **84** (B14), 8332-8334

JAMES, P.B. (1982). Recession of Martian North Polar Cap: 1979-1980 Viking Observations. *Icarus* **52**, 565-569

JAMES P.B., K. LUMME (1982). Martian South Polar Cap Boundary: 1971 and 1973 Data. *Icarus* **50**, 368-380

KEIFFER, H.H., T.Z. MARTIN, A.P. PETERFREUND, B.M. JAKOSKY, E.D. MINER, F.D. PALLUCONI (1977). Thermal and Albedo Mapping of Mars during the Viking Primary Mission. *Journal of Geophysical Research* **82** (28), 4249-4291

KELLERMAN, K.I. (1965). Radio Observations of Mars. *Nature* **206** 1034

KLEIN, M.J. (1971). Mars: Measurements of Its Brightness Temperature at 1.85 and 3.75cm Wavelength. *Icarus* **14** 210-213

KUZ'MIN, S.O., B.Y. LOSOVSKII (1984). Radiometric Inhomogeneity of Mars at Millimeter Radio Wavelengths. *Solar System Research* **17**, 119-124

LEIGHTON, R.B., MURRAY, B.C. (1966). Behavior of Carbon Dioxide and Other Volatiles on Mars. *Icarus* **153**, 136-144

MAYER, C.H. P.T. MCCULLOUGH (1971). Microwave Radiation of Uranus and Neptune. *Icarus* **14**, 187-191

MUHLEMAN, D.O. (1965). Radar Scattering from Venus and Mercury at 12.5cm. *Journal of Research of the National Bureau Standards, Radio Science*, **69D** 1630-1631

MUHLEMAN, D.O. (1972). Microwave Emission from the Moon. In *Thermal Characteristics of the Moon.* (J.W. Lucas, Ed.) pp. 51-81. MIT Press, Cambridge, Mass.

MUHLEMAN, D.O., G.B. BERGE, D.J. RUDY, A. NIELL (1986). Precise VLA Positions and Flux Density Measurements of the Jupiter System. Submitted to *Astronomical Journal*

PAIGE, D.A., A.P. INGERSOLL (1985). Annual Heat Balance of Martian Polar Caps: Viking Observations. *Science* **228**, 1160-1168

PALLUCONI, F.D., H.H. KEIFFER (1981). Thermal Inertia Mapping of Mars from 60°S to 60°N. *Icarus* **45**, 415-426

PETTENGILL, G.H., I.I. SHAPIRO, A.E.E. ROGERS (1973). Topography and Radar Scattering Properties of Mars. *Icarus* **18**, 22-28

PIDDINGTON, J.H., H.C. MINNETT (1949). Microwave Thermal Radiation from the Moon. *Australian Journal of Scientific Research*, **Series A2**, p.63

POLLACK, J.B., D.S. COLBURN, F.M. FLASER, R. KAHN, C.E. CARLSTON, D. PIDEK (1979). Properties and Effects of Dust Particles Suspended in the Martian Atmosphere. *Journal of Geophysical Research* **84**(B6), 2929-2945

PRESS, W.H., B.P. FLANNERY, S.A. TEUKOLSKY, W.T. VETTERLING (1986). *Numerical Recipes: The Art of Scientific Computing.* University of Cambridge

Press, Cambridge, U.K.

RICHTMYER, R.D., K.W. MORTON (1967). *Difference Methods for Initial-Value Problems.* Interscience Publishers, New York, New York.

SCHLOERB, F. P., D.O. MUHLEMAN, G. L. BERGE (1976). Lunar Heat Flow and Regolith Structure Inferred from Interferometric Observations at a Wavelength of 49.3cm. *Icarus*, **29**, 329-341

SCHWARZ, U.J. (1979). Interferometry and Aperture Synthesis. In *Image Formation from Coherence Functions in Astronomy*, Proceedings of IAU Colloquium No.49 (C. Van Schooneveld Ed.) pp.261-275, D. Reidel

SCOTT, D.H., M.H. CARR (1976). Geologic Map of Mars, Map I-1083, United States Geologic Survey, Washington, D.C.

SIMPSON, R.A., B.C. FAIR, H.T. HOWARD (1980). Microwave Properties of Solid CO_2. *Journal of Geophysical Research* **85**(B10), 5481-5484

SIMPSON, R.A., G.L. TYLER (1981). Viking Bi-static Radar Experiment: Summary of First-Order Results Emphasizing North Polar Data. *Icarus* **46**, 361-389

SIMPSON, R.A., G.L. TYLER (1984). Viking Bi-static Radar Experiment: Summary of Results In Near-Equatorial Regions . *Journal of Geophysical Research* **89**(B12), 10385-10404

THEKAEKARA, M.P., A.J. DRUMMOND (1971). Standard Values for the Solar Constant and its Spectral Components. *Nature- Physical Science* **229**, 6-10

VOHDEN, R.A., F.G. SMITH (1983-1986), ed. *The Astronomical Almanac*, U.S.

Government Printing Office, Washington, D.C.

WEAST, R.C., S.M. SELBY, C.D. HODGMAN (1965), ed. *CRC Handbook of Chemistry and Physics*, p. B165, Chemical Rubber Company, Cleveland, Ohio.

WELLS, E.N., J. VEVERKA, P. THOMAS (1984). Mars: Experimental Study of Albedo Changes Caused by Dust Fallout. *Icarus* **58**, 331-338

APPENDIX A
THERMAL MODEL DETAILS

The thermal model consists of numerically solving the equation of heat conduction for the sub-surface of Mars. This equation can be written as:

$$\frac{\partial T(x,t)}{\partial t} = \frac{1}{\rho c_p(x)} \frac{\partial}{\partial x} \left(k_t(x) \frac{\partial T(x,t)}{\partial x} \right) \qquad A.1$$

where $T(x,t)$ is the physical temperature as a function of the sub-surface depth x and time t, $\rho c_p(x)$ is the volume specific heat as a function of the sub-surface depth and $k_t(x)$ is the thermal conductivity, also as a function of depth. Although, $\rho c_p(x)$ and $k_t(x)$ are both assumed not to vary with depth for the models calculated in this thesis, they will be described as functions of the sub-surface depth in this appendix, because the numerical solution of this differential equation was solved in such a way as to allow them to vary.

The solution of this problem depends on the boundary conditions that are imposed. As was stated in Chapter 3, the lower boundary condition was that no heat flux passed through the bottom boundary and that the bottom layer was deep enough that the temperature did not change by more than half a degree during the entire martian year. Because of the logistical problems with allowing the lower boundary layer to vary in depth during the calculation of the thermal profiles, extensive testing was performed to find the maximum depth that these conditions could be met for any combination of thermal parameters and latitudes. The actual depth steps taken were calculated according to the following formula. The first depth was taken to be 1mm. The first depth step was taken to be 1.2 times the first depth, so the second depth was at 2.2mm. Each of the following depth steps was 1.2 times the previous step. The actual depths were the sum of these constantly changing depth steps. Part of the reason of choosing this particular step size was to insure the daily thermal wave

was being properly sampled. There were twelve depths sampled above 4cm, which is the diurnal skin depth. This is a reasonable number of samples to insure accuracy, especially since they are concentrated near the surface.

Given this algorithm for calculating depths and the conditions imposed on the lower boundary, the maximum depth turned out to be 1270cm. Although these depths were used to calculate the thermal model for comparison with the data, for testing purposes the depth step size and time step used were those of Keiffer *et al.* (1977). This was done to test the algorithm against a well known standard. Unfortunately, the levels used by Keiffer *et al.* were not very good for the purpose of making models for comparison to the radio data.

The surface boundary condition, as already stated in Chapter 3, is:

$$\frac{S_\odot(1-A^*)cos(\psi)}{R^2(t)} + k_t(0)\frac{\partial T}{\partial x}\Big|_{surface} + L\frac{dM_{CO_2}}{dt} + F_a = \varepsilon\sigma T^4(0,t) \qquad A.2$$

The first term on the left hand side is the solar insolation term, $S_\odot$ being the solar constant (whose value was taken to be 1.3533×10^6 erg cm^{-2} sec^{-1}, following Thekaekara and Drummond, 1971). A^* is the Bond albedo, gotten from the work of Palluconi and Keiffer (1981). R is the heliocentric distance of Mars in AU, and was taken directly from the Astronomical Almanac, Vohden and Smith (1983,1984,1985,1986) and ψ is the angle the incident radiation makes with the surface of a planet at a given latitude and longitude. The orbit of Mars was assumed to be co-linear with the plane of the ecliptic. Since this angle is currently about 1.8°, I believe this approximation is justified. The second term on the left hand side of the equation is the heat flux either going into or coming out of the sub-surface. The third term is the heat lost to the formation or gained from the sublimation of CO_2 frost. The fourth term, F_a, is a radiation backscatter term. The only term on the right hand side is the radiative emission term. The thermal models used for comparison purposes had a ε of 1.0.

As stated in the main body of the thesis the radiative backscatter term was given a value of about 0.02 of the noontime solar insolation or 0.02 of the value of the surface frost emission, which ever was greater. This is the value of Keiffer *et al.* (1977). In actuality the value used was 0.018 rather than 0.02. This is because one of the main tests of the thermal model was its ability to reproduce the work of Keiffer *et al.* (1977). However, the model they used differed from the present model in a number of ways. As the model used here does not, it did not agree with the work of Keiffer *et al.* . Using the same time steps and depth steps as Keiffer *et al.*, I found that a value of the radiation backscatter term of 0.018 rather than 0.02 gave the desired reproducibility. By comparing Figures A.1 and A.2 with those published in Keiffer *et al.* it is easy to see that the two are very similar. Therefore, I believe that the current thermal model reproduces the surface temperatures, as observed by the Viking IRTM instrument, very well indeed.

The first thing that has to be done in order to solve this differential equation numerically is to discretize it. The discretization was done so as to allow the vertical depth step to vary and still have the algorithm be stable. The discrete equation that was actually solved is:

$$(\rho c_p)_j \frac{T_j^{n+1} - T_j^n}{\Delta t} = 0.5 \left[\frac{\delta(k\frac{\delta T}{\Delta x})_j^{n+1}}{0.5(\Delta x_{j-\frac{1}{2}} + \Delta x_{j+\frac{1}{2}})} \right] + 0.5 \left[\frac{\delta(k\frac{\delta T}{\Delta x})_j^{n}}{0.5(\Delta x_{j-\frac{1}{2}} + \Delta x_{j+\frac{1}{2}})} \right] \quad A.3$$

where j stands for the depth level and n stands for the nth timestep. The secondary differences are given by

$$\delta\left(k\frac{\delta T}{\Delta x}\right)_j = k_{j+\frac{1}{2}} \frac{(T_{j+1} - T_j)}{\Delta x_{j+\frac{1}{2}}} - k_{j-\frac{1}{2}} \frac{(T_j - T_{j-1})}{\Delta x_{j-\frac{1}{2}}} \quad A.4$$

The half-step notation indicates that the quantity should be evaluated half-way between the two depth levels. For the Δx quantities this means the Δx between the given x and the x on the other side of it. That is, $\Delta x_{j-\frac{1}{2}} = x_j - x_{j-1}$ and

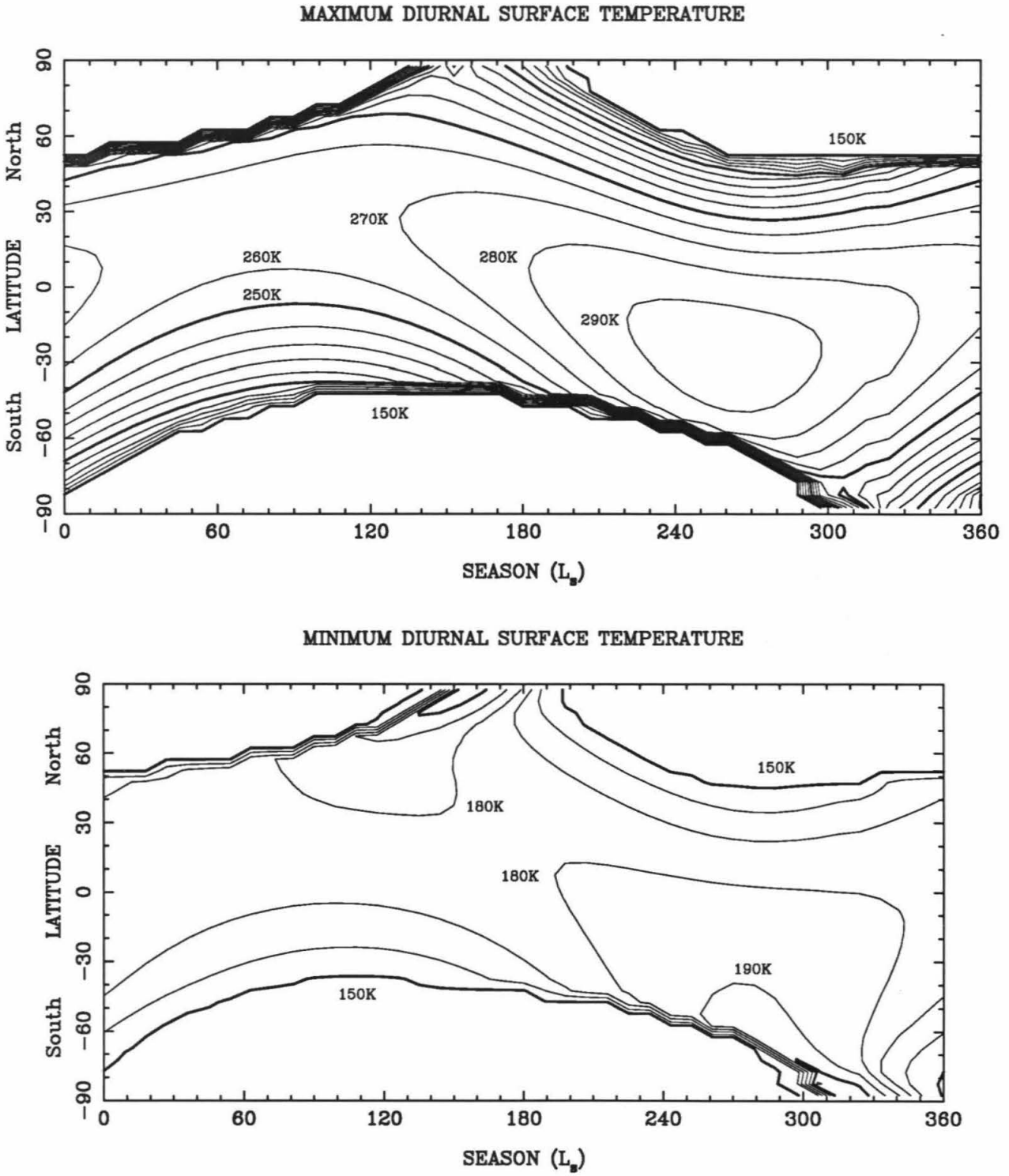

FIGURE A.1: Surface temperatures as a function of Martian season. The model parameters were set up to emulate the work of Keiffer *et al.* (1977). These are the maximum and minimum surface temperatures.

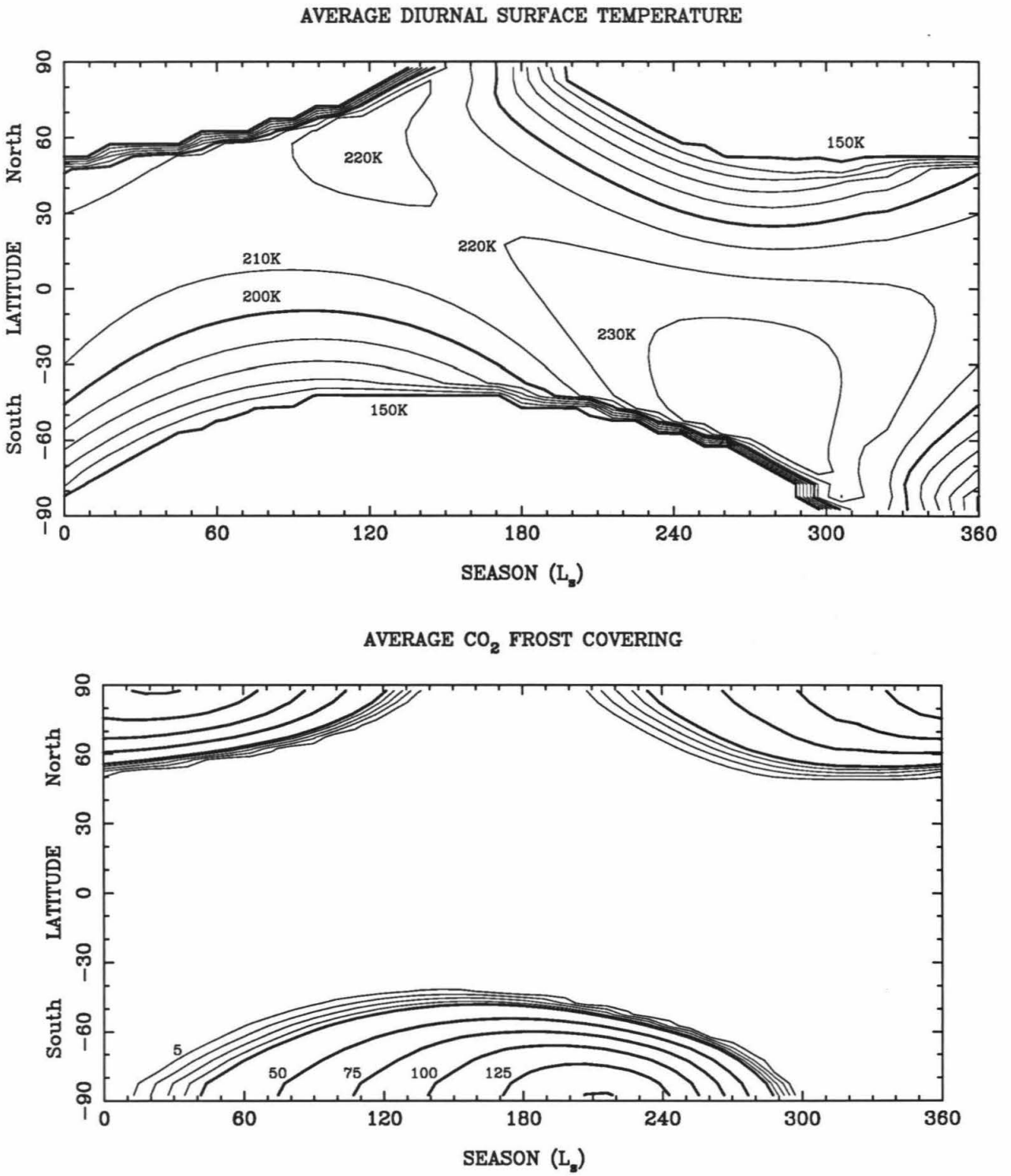

FIGURE A.2: The upper plot is the diurnally averaged surface temperature as a function of Martian season. The lower plot is the diurnally averaged CO_2 frost covering. Units are gm cm^{-2}

$\triangle x_{j+\frac{1}{2}} = x_{j+1} - x_j$. Combining all terms with the same T grid point yields:

$$\begin{aligned}
&T_j^{n+1}\left(\frac{k_{j+\frac{1}{2}}\triangle x_{j-\frac{1}{2}}k_{j-\frac{1}{2}}\triangle x_{j+\frac{1}{2}}}{(\triangle x_{j-\frac{1}{2}}+\triangle x_{j+\frac{1}{2}})\triangle x_{j+\frac{1}{2}}\triangle x_{j-\frac{1}{2}}}+\frac{(\rho c_p)_j}{\triangle t}\right)\\
&-T_{j+1}^{n+1}\left(\frac{k_{j+\frac{1}{2}}}{(\triangle x_{j-\frac{1}{2}}+\triangle x_{j+\frac{1}{2}})\triangle x_{j+\frac{1}{2}}}\right)-T_{j-1}^{n+1}\left(\frac{k_{j-\frac{1}{2}}}{(\triangle x_{j-\frac{1}{2}}+\triangle x_{j+\frac{1}{2}})\triangle x_{j-\frac{1}{2}}}\right)\\
&=T_j^{n}\left(\frac{-k_{j+\frac{1}{2}}\triangle x_{j-\frac{1}{2}}k_{j-\frac{1}{2}}\triangle x_{j+\frac{1}{2}}}{(\triangle x_{j-\frac{1}{2}}+\triangle x_{j+\frac{1}{2}})\triangle x_{j+\frac{1}{2}}\triangle x_{j-\frac{1}{2}}}-\frac{(\rho c_p)_j}{\triangle t}\right)\\
&+T_{j+1}^{n}\left(\frac{k_{j+\frac{1}{2}}}{(\triangle x_{j-\frac{1}{2}}+\triangle x_{j+\frac{1}{2}})\triangle x_{j+\frac{1}{2}}}\right)+T_{j-1}^{n}\left(\frac{k_{j-\frac{1}{2}}}{(\triangle x_{j-\frac{1}{2}}+\triangle x_{j+\frac{1}{2}})\triangle x_{j-\frac{1}{2}}}\right)
\end{aligned} \qquad A.5$$

This is the actual difference equation solved. The $\triangle x$'s are known before any computation of temperature profiles is begun; as are the volume specific heat, and the thermal conductivity. At any given time-step the temperatures at the previous time-step are also known. Therefore, the entire right-hand-side of this equation is known for any particular time-step, and only the three temperatures at the next time-step need be solved for. This implicit method is stable for any time step and is second-order accurate in time. This differencing scheme is sometimes called the 'Crank-Nicholson' implicit solution. In addition, the set of simultaneous linear equation that must be solved is a tridiagonal system. This allows an easy, quick, and robust solution to the system of equations. For a good discussion of the solution of tridiagonal systems see Richtmyer and Morton (1967) or Press *et al.* (1986).

The surface boundary was discretized in a rather straight-forward manner and the result is:

$$\frac{S_\odot^{n+1}(1-A^*)cos(\psi^{n+1})}{(R^2)^{n+1}}+(k_t)_{j=0}\frac{\partial T}{\partial x}\Big|_{x=0}^{n+1}+L\frac{M_{CO_2}^{n+1}-M_{CO_2}^{n}}{\triangle t}+F_a=\varepsilon\sigma(T_{j=0}^4)^{n+1} \qquad A.6$$

where the surface heat conductivity term is estimated by

$$\frac{\partial T}{\partial x}\Big|_{x=0}^{n+1}\simeq\frac{T_0^{n+1}(2x_0-x_1-x_2)}{(x_2-x_0)(x_1-x_0)}+\frac{T_1^{n+1}(x_2-x_0)}{(x_1-x_0)(x_2-x_1)}-\frac{T_2^{n+1}(x_1-x_0)}{(x_2-x_1)(x_2-x_0)} \qquad A.7$$

This surface temperature gradient is a derived from a Taylor expansion of the temperature at the first depth level.

$$T_1 = T_0 + \frac{\partial T}{\partial x}\Big|_{x=0}(x_1 - x_0) + \frac{\partial^2 T}{\partial x^2}\Big|_{x=0}\frac{(x_1 - x_0)^2}{2} + \cdots \qquad A.8$$

Dropping higher order terms and solving for the temperature gradient at the surface yields:

$$\frac{\partial T}{\partial x}\Big|_{x=0}^{n+1} \simeq \frac{T_1^{n+1} - T_0^{n+1}}{x_1 - x_0} - \frac{\partial^2 T}{\partial x^2}\Big|_{x=0}^{n+1}\frac{(x_1 - x_0)}{2} \qquad A.9$$

assuming that the second derivative changes relatively slowly, the second derivative at the surface can be replaced by the second derivative at the level $x = x_1$. The standard centered second-order difference can be used to replace the second derivative in equation A.9, yielding equation A.7.

Since this boundary condition needs the temperature at the time step $n+1$, but is also *needed* to solve for the temperatures at this time step, the solution to this form of the heat equation, with this boundary condition, is acquired iteratively. That is, in place of the temperatures at $n+1$, the temperatures at n are used to estimate the surface thermal gradient, i.e.

$$\begin{aligned}\varepsilon\sigma(T_{j=0}^4)^{n+1} &= \frac{S_\odot^{n+1}(1-A^*)cos(\psi^{n+1})}{(R^2)^{n+1}} + L\frac{M_{CO_2}^{n+1} - M_{CO_2}^n}{\triangle t} + F_a \\ &+ (k_t)_{j=0}\left[\frac{T_0^n(2x_0 - x_1 - x_2)}{(x_2 - x_0)(x_1 - x_0)} + \frac{T_1^n(x_1 - x_0)}{(x_1 - x_0)(x_2 - x_1)} - \frac{T_2^n(x_2 - x_1)}{(x_2 - x_1)(x_2 - x_0)}\right]\end{aligned} \qquad A.10$$

This equation was solved for T^{n+1}, which was then used to calculate a thermal profile. This thermal profile was used to calculate a new surface thermal gradient and this, in turn was used to calculate a new surface temperature, say $\overline{T}^{n+1}$. If this new surface temperature differed from the old one by more than a specified amount, a new temperature profile was calculated. This iterative procedure was continued until convergence was reached, i.e. $\overline{T}^{n+1} \simeq T^{n+1}$. For the final year of the model this convergence criterion was 0.1K. This final temperature profile was then the solution

of the heat equation for the $n+1$ time step and was stored, to be used at the next timestep. This process was continued until an entire day was completed.

Because the amount of CO_2 could also vary it was handled in the following manner. If the temperature dropped below the condensation temperature, here taken to be 149K, the surface temperature was set to be 149K and the albedo was discontinuously changed to 0.65. The extra heat needed to hold the surface temperature at this level was made up for by the heat of condensation of CO_2 frost. The value use for the heat of condensation was 5.9×10^6erg gm-1. The mass, M_{CO_2}, calculated in this way was saved for the next time step. The mass stored had units of gm cm^{-2}. As long as the final surface temperature calculated iteratively was below this temperature of condensation, the amount of CO_2 frost increased.

If the mass of CO_2 frost stored was non-zero and the surface temperature was estimated to be above the temperature of condensation (or, equivalently, sublimation), then the amount of CO_2 frost required to sublimate in order to keep the surface temperature at the sublimation temperature was calculated. If the amount of CO_2 frost deposited was greater than this amount, the amount stored was reduced by this required amount. If the amount stored was less than the amount required to keep the surface temperature at the sublimation temperature, the amount of heat required to sublimate the stored amount was calculated and subtracted from the solar flux term. The albedo was changed back from 0.65 to its previous value and a new surface temperature was calculated. Because the albedo of the CO_2 frost is higher than any of the other albedos used, this part of the algorithm is stable. If some of the surface albedos were larger than the CO_2 frost albedo this part of the calculation might go into an endless loop.

Since the amount of computer time needed to do a daily temperature calculation is large, the heat equation was solved only every fifth day. Therefore, although the

minor time step was about 20 minutes, the major time step was five Martian days. A linear approximation was used to get across one large time step. The final, minor time step of one day plus the final, minor time step of the day five days previous were used to estimate the minor time step just before the beginning of the next major time step. That is, the same time of day temperature profiles were used to make this jump across the major time step. The problem of what to do when the frost disappears across a major time step is another difficulty inherent in this interpolation. Here the last temperature profile from the previous major time step is used as initial temperature profile for the upcoming day. I have confidence in this method, as long as the major time step does not get too large. This same model was run on the San Diego Cray X-MP, but with no missing days. Plots of the surface temperature are identical to those whose major time step was five days.

Several more approximations were made in order to solve for all latitudes and longitudes. Since the thermal inertia maps of Palluconi and Keiffer (1981) only extend as high as 60°N and as low as 60°S the regions above and below these limits needed to have these parameters estimated. The thermal parameters for the latitude adjacent to these regions were averaged over longitude and these values were used in each of the two regions. This means that for latitudes above 60°N the albedo used was 0.1965 and the thermal inertia used was 8.732. For latitudes below 60°S, the albedo and thermal inertia were 0.2324 and 6.629, respectively. In addition, the volume specific heat, $\rho c_p(x)$, was needed. This is because, although the thermal inertia is known, what is really needed to solve the heat equation is the conductivity and the volume specific heat separately, not combined into the thermal inertia. The thermal inertia is given by:

$$I = \sqrt{k_t \rho c_p} \qquad A.10$$

where k_t is the thermal conductivity. Since volume specific heat does not change

much for most geologic materials, the value of 1×10^7erg cm^{-3} K^{-1} was assumed for all latitude and longitude bins. Among geologic materials, the variations in thermal conductivity are much larger than the variations in the volume specific heat, so all of the variation in the thermal inertia was assigned to the thermal conductivity.